AD-A039 175 LEAR SIEGLER INC SANTA MONICA CALIF F/G 20/12
SOLID STATE RESEARCH, 1976:4.(U)
NOV 76 A L MCWHORTER F19628-76-C-0002
UNCLASSIFIED ESD-TR-76-327 NL

1 OF 1
AD A039175

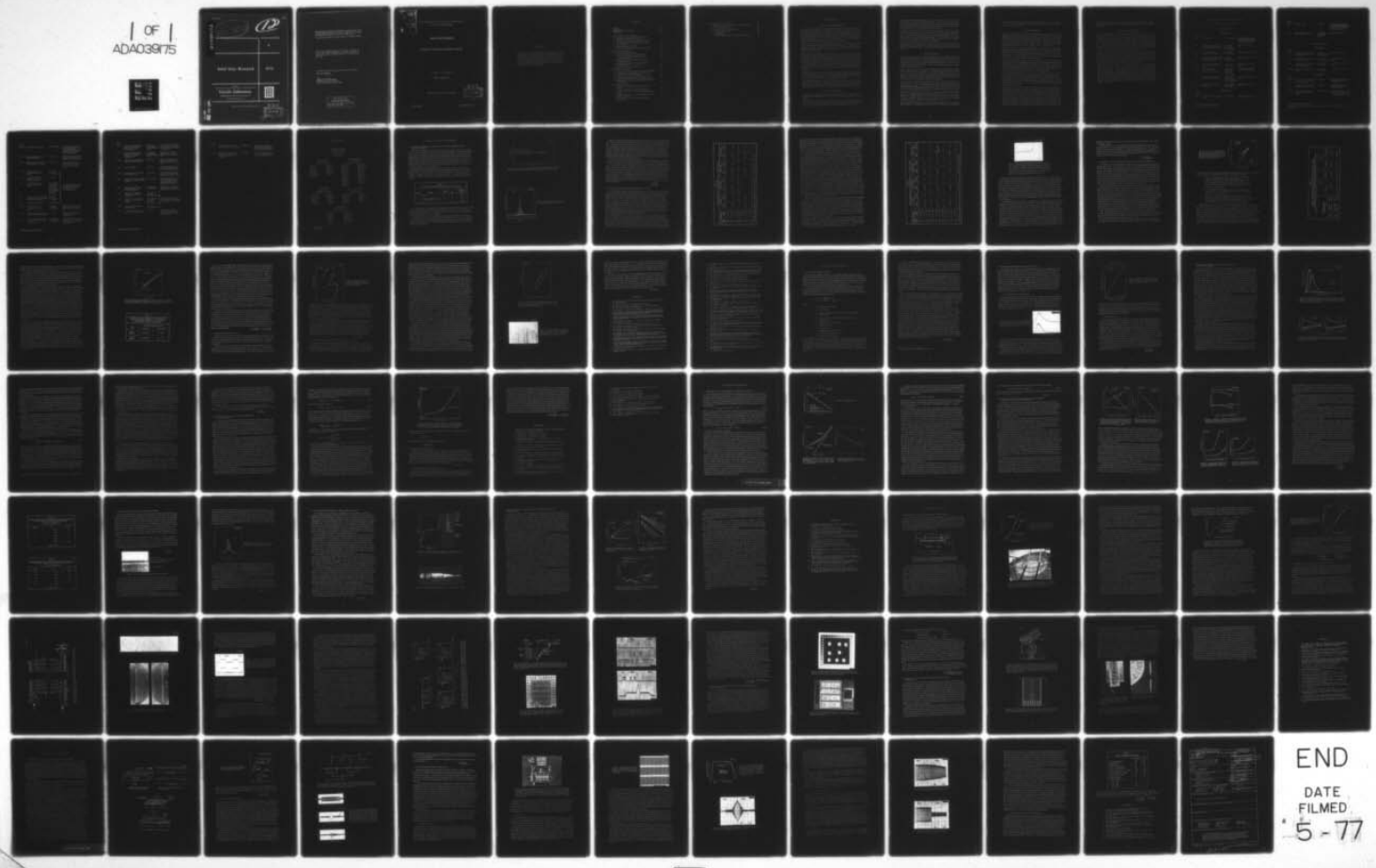

END
DATE FILMED
5-77

ESD-TR-76-327

AD A039175

See 1473

12

FC

4

Solid State Research

1976

Prepared
under Electronic Systems Division Contract F19628-76-C-0002 by

Lincoln Laboratory

MASSACHUSETTS INSTITUTE OF TECHNOLOGY

LEXINGTON, MASSACHUSETTS

Approved for public release; distribution unlimited.

DDC
RECEIVED
MAY 10 1977
D

DDC FILE COPY

The work reported in this document was performed at Lincoln Laboratory, a center for research operated by Massachusetts Institute of Technology, with the support of the Department of the Air Force under Contract F19628-76-C-0002.

This report may be reproduced to satisfy needs of U.S. Government agencies.

The views and conclusions contained in this document are those of the contractor and should not be interpreted as necessarily representing the official policies, either expressed or implied, of the United States Government.

This technical report has been reviewed and is approved for publication.

FOR THE COMMANDER

Raymond L. Loiselle

Raymond L. Loiselle, Lt. Col., USAF
Chief, ESD Lincoln Laboratory Project Office

Non-Lincoln Recipients

PLEASE DO NOT RETURN

Permission is given to destroy this document when it is no longer needed.

ACCESSION for
NTIS White Section
DDC Buff Section
UNANNOUNCED
JUSTIFICATION
BY
DISTRIBUTION/AVAILABILITY CODES
Dist. AVAIL. and/or SPECIAL
A

MASSACHUSETTS INSTITUTE OF TECHNOLOGY

LINCOLN LABORATORY

SOLID STATE RESEARCH

QUARTERLY TECHNICAL SUMMARY REPORT

1 AUGUST – 31 OCTOBER 1976

ISSUED 2 MARCH 1977

Approved for public release; distribution unlimited.

DDC
RECEIVED
MAY 10 1977
D

LEXINGTON MASSACHUSETTS

ABSTRACT

This report covers in detail the solid state research work of the Solid State Division at Lincoln Laboratory for the period 1 August through 31 October 1976. The topics covered are Solid State Device Research, Quantum Electronics, Materials Research, Microelectronics, and Surface-Wave Technology. Funding is primarily provided by the Air Force, with additional support provided by the Army (BMDATC), ARPA (MSO, IPTO), NSF, and ERDA.

CONTENTS

	Abstract	iii
	Introduction	vii
	Reports on Solid State Research	xi
	Organization	xvi
I.	SOLID STATE DEVICE RESEARCH	1
	A. 1000-Hour Continuous CW Operation of Double-Heterostructure GaInAsP/InP Lasers	1
	B. Multiple-Energy Proton Bombardment in n^+-GaAs	3
	C. Low-Dose n-Type Ion Implantation into Cr-Doped GaAs Substrates	8
	D. *Surface Outdiffusion in n-CdTe*	13
	E. Liquid-Phase Epitaxial Growth of $PbS_{1-x}Se_x$ Alloys	14
II.	QUANTUM ELECTRONICS	19
	A. NdLa Pentaphosphate Lasers	19
	B. Passive Q-Switching and Frequency Doubling	21
	1. SF_6 Absorber and Frequency-Doubling	21
	2. Freon 12 Absorber	22
	C. Resonant Infrared Third-Harmonic Generation in Cryogenic Liquids	23
	D. Vibrational Two-Photon Resonance Linewidths in Condensed Media	27
	E. Double-Resonance Spectroscopy of SF_6	29
III.	MATERIALS RESEARCH	33
	A. Thickness of InP Layers Grown by Liquid-Phase Epitaxy	33
	B. Conditions for Lattice Matching in the LPE Growth of GaInAsP Layers on InP Substrates	36
	C. Double-Heterostructure GaInAs/InP Diode Lasers	41
	D. Seeded Bridgman Growth of $AgGaSe_2$ Single Crystals	43
	E. Selective Black Absorbers Using RF-Sputtered Cr_2O_3/Cr Cermet Films	45
IV.	MICROELECTRONICS	
	A. Ion-Implanted Lo-Hi-Lo Annular GaAs IMPATT Diodes	49
	B. Charge-Coupled Devices (CCDs): Imaging Sensor	53
	C. Charge-Coupled Devices: Programmable Transversal Filter	56
	D. Eight-Bit Multiplier Circuit Using Multilayer Thin-Film Hybrid Technology	61
	E. Integral Stripline Filters for Submillimeter-Wave Mixer Diodes	63

V. SURFACE-WAVE TECHNOLOGY 69

A. Suppression of Bulk-Scattering Loss in SAW Resonators 69

B. Variable-Bandwidth Filter 71

C. Acoustoelectric Memory Correlator 73

1. Mechanical Assembly 73
2. Diode Array 74
3. RF Results 77
4. Recent Achievements Compared With Design Goals 79

INTRODUCTION

I. SOLID STATE DEVICE RESEARCH

The first two double-heterostructure GaInAsP/InP diode lasers to be life-tested have so far logged over 1000 and 600 hr, respectively, of continuous CW operation at room temperature without degradation. For both devices, the emission wavelength is 1.15 μm and the output powers are 2 and 4 mW, respectively. It is of particular interest that the lasers tested were fabricated from heterostructures grown on an InP substrate with a dislocation density of about 5×10^5 cm^{-2}, since GaAs/GaAlAs lasers grown on substrates with such a high dislocation density would have very short lifetimes.

For n^+-GaAs, a multiple-energy proton bombardment is shown to be superior to a single-energy bombardment in preparing uniform high-resistivity layers. An appropriate combination of a multiple-bombardment schedule followed by an anneal, which can be at a temperature as high as 500°C for carrier concentrations of 10^{18} cm^{-3}, can yield 10^6 to 10^8 Ω-cm layers in n^+-GaAs.

When low-dose n-type implants are made directly into Cr-doped GaAs, anomalous results are obtained on a large percentage of commercially available ingots. For some Cr-doped ingots, a thin n-type skin of "anomalous excess carriers" is observed after implantation, whereas low activation of the implanted ions is observed in other ingots. On the ingots that show "excess carriers," an improved encapsulation procedure is described which can substantially reduce, and in some cases eliminate completely, the excess sheet concentration. On the ingots that show low activation, an ion-implantation damage-gettering technique is discussed which has been used to increase the activation of implanted ions to ≳80 percent.

Schottky-barrier capacitance measurements have revealed that heating Br- and In-doped n-type CdTe wafers in the 75° to 300°C temperature range produces a large decrease in carrier concentration near the surface. This effect is presumably due to the outdiffusion of Cd and the concomitant formation of compensating defect centers.

Liquid-phase epitaxial films of $PbS_{1-x}Se_x$ on PbS substrates were grown using cooling rates in excess of 20°C/min. and initial growth temperatures of approximately 600°C. Liquidus data for growth solutions of $Pb_{1-y}S_y$ and $Pb_{1-y}(S_{0.7}Se_{0.3})_y$ are given in the temperature range of 580° to 670°C for y values in the 0.005 to 0.010 range, respectively.

II. QUANTUM ELECTRONICS

Calculations and preliminary experiments have been carried out on the feasibility of substituting NdLa pentaphosphate lasers for low-power Nd:YAG lasers using lamp or solar excitation.

With $CdGeAs_2$ and a passively Q-switched CO_2 laser pump, 1.9 W of average doubled power have been obtained. The second harmonic was generated in an antireflection coated crystal using 10.4 W of average input power and a pulse repetition rate of 20 kHz.

Two-photon resonantly enhanced tripling of CO_2 laser radiation in liquid CO mixtures has been observed. Using a tight focusing geometry, a power-conversion efficiency of 0.3 percent for the CO_2 R(6) line at 1069.01 cm^{-1} has been achieved in a CO-O_2 solution. The solvent dependence of the CO two-photon resonance has been studied. Phasematching with an additional molecular constituent has been demonstrated.

A simple analytical model has been developed for the contribution of the vibration-rotation interaction to the linewidth of the isotropic two-photon resonance in simple molecular liquids. The results indicate that this process, which has not been included in recent theoretical calculations, contributes significantly to the observed linewidths. The evolution of the two-photon resonance peak intensity through the Doppler-broadened, pressure-broadened, and motionally narrowed regimes is illustrated.

Double-resonance spectroscopy of the ν_3 band of SF_6 has been carried out using a Q-switched CO_2 laser as the pump and a tunable PbSnTe diode laser as the probe. The effects of an intense optical field on rotational-vibrational transitions in the gas have been observed.

III. MATERIALS RESEARCH

In order to achieve accurate control of the thickness of the liquid-phase-epitaxial InP layers that are incorporated in GaInAsP/InP double-heterostructure diode lasers, this thickness has been determined as a function of the growth parameters. Since the results are consistent with a simplified model for diffusion-limited growth, they have been used to determine the diffusion coefficient of P in In-rich In-P solutions as a function of temperature between 550° and 680°C.

In developing a procedure for fabrication of GaInAsP/InP double-heterostructure diode lasers, a detailed study has been made of the liquid-phase epitaxial growth of GaInAsP layers on InP substrates. No evidence has been found that lattice-matched epilayer compositions are favored in this system; the composition is a sensitive function of the growth parameters, which must therefore be closely controlled in order to obtain the lattice-matched GaInAsP layers required for efficient laser operation.

Laser emission at 1.58 μm has been obtained at about 80 K for double-heterostructure diodes with an active region of $Ga_{0.465}In_{0.535}As$ sandwiched between barrier layers of InP and $Ga_{0.20}In_{0.80}As_{0.48}P_{0.52}$. This emission wavelength is the longest that can be obtained for lattice-matched GaInAsP/InP diode lasers, since the active region composition is the P-free limit of the series of GaInAsP alloys with the same lattice constant as InP.

Seeded vertical Bridgman growth of $AgGaSe_2$, a material for nonlinear infrared applications, has reproducibly yielded crack-free single crystals with volumes of several cubic centimeters. Orienting the growth axis approximately parallel to the crystallographic c-axis has eliminated cracking that previously occurred because the thermal expansion coefficient of $AgGaSe_2$ is negative for directions within 25° of the c-axis.

Excellent selective black absorbers, with the high solar absorption and low infrared emittance needed for use in flat-plate solar collectors, have been prepared by employing RF

sputtering to coat metal substrates with successive thin films of Cr_2O_3/Cr cermet and Cr_2O_3. Such thin-film composites deposited on Ni-coated stainless steel are stable in air at temperatures up to 300°C.

IV. MICROELECTRONICS

Large-area annular IMPATT diodes have been fabricated from GaAs having a lo-hi-lo impurity profile created by silicon ion implantation. Proton bombardment was used to define the annuli. Measurements of the thermal resistance of annular diodes and disk diodes of equivalent active area have indicated that the thermal resistance has been reduced by as much as 30 percent by virtue of the annular geometry. An efficiency of 35 percent with an output power of 7.4 W has been achieved at 3.0 GHz, and another device has generated an output power of 12.1 W with an efficiency of 21.6 percent at 3.15 GHz.

Fabrication of the 100- × 400-cell CCD imaging sensors for the GEODSS (Ground Electro-Optical Deep Space Surveillance) Program has begun. Processing of the first "set" of silicon wafers has been completed, and approximately 13 percent of the devices on the wafers were free of gate-gate and gate-substrate shorts and were thus suitable for dynamic testing. Successful operation of one of these devices with electrical input signals has been achieved at the design goal data rate of 400 kHz.

A new transversal filter structure is described which uses charge-coupled device (CCD) technology, and is capable of handling signals at data rates much higher than existing CCD implementations. This structure allows tap weights to be programmed as digital words, which can be stored on the device in static shift registers. A 32-stage prototype device has been designed and tested at data rates up to 20 MHz, which is the limit of our present clocking circuitry. Operation at even higher rates appears feasible.

A two's-complement multiplier which can multiply two 8-bit signed numbers in less than 75 nsec has been fabricated in hybrid integrated circuit form using commercially available Schottky TTL dice. This project was undertaken in order to demonstrate the possible reduction in size of complex digital systems. The multiplier circuit was selected because it was felt to have greater applicability than a more specialized circuit. By putting eight dice into one package, a 6-to-1 reduction in system size over standard DIP packaging has been achieved.

The bias filter in a mixer diode circuit supplies DC bias to the mixer diode and provides the intermediate frequency output, while presenting an almost perfect reflection at the signal and local-oscillator frequencies. At centimeter wavelengths, the bias filters are usually made by using quarter-wavelength low- and high-impedance coaxial line sections to form a low-pass filter structure. However, at millimeter and submillimeter wavelengths, the low-pass bias filter cannot be constructed in coaxial form since the coaxial line dimensions become too small to fabricate by conventional machining operation. Bias filters for submillimeter wave mixers have been provided by an integral stripline filter which is incorporated into the diode package. The characteristics of these filters at submillimeter wavelengths were inferred from measurements made on dimensionally scaled

filter models in the frequency range from 1.0 to 9.0 GHz. This use of scaled models is essential in evaluating mixer components for potential operation in the submillimeter wave region.

V. SURFACE-WAVE TECHNOLOGY

In order to maximize the Q in surface-acoustic-wave (SAW) resonators, it is necessary to minimize small residual losses. One such loss is due to scattering from surface waves into bulk waves at the edges of a reflection grating. This loss process has been suppressed by tapering the groove depth of successive grooves in a grating from zero up to the maximum depth. A taper which extends over a relatively short distance (typically 20 to 30 grooves) at the grating edge is adequate to significantly decrease the scattering loss. A simple ion-beam-etching technique has been developed for obtaining the tapers. With tapering, a Q of 80,000 has been obtained at 170 MHz on $LiNbO_3$, and a Q of 61,000 at 150 MHz on ST-quartz. These Qs are close to the material-loss limit.

A filter circuit which employs a pair of reflective-array compressors (RACs) has been developed. This unique circuit exploits the exceptional filter characteristics of RAC devices to obtain a bandpass filter with a bandwidth which is continuously variable over more than a 20:1 range. The bandwidth is varied by changing the frequency of a pair of oscillators in the filter circuit. A prototype circuit provides a bandwidth variable from 0.8 to 22 MHz, together with more than 50-dB out-of-band rejection.

Significant advances have been made in acoustoelectric memory-correlator technology. The memory correlator is a gap-coupled SAW device in which a matrix of freestanding diodes on a silicon strip is held in close proximity (~300-nm gap) to the surface of an $LiNbO_3$ SAW delay line. Interactions between the surface waves and the diodes provide a wide-band programmable analog matched filter. Improvements in the Schottky-diode arrays, the substrate geometry, and the mechanical assembly have yielded the desirable features of a stable, uniform response with wide bandwidth and long storage time (up to 100 msec). The use of LEDs for erasure of stored reference waveforms has been demonstrated. The major residual problem to be solved is the suppression of spurious signals in memory correlators.

15 August through 15 November 1976

PUBLISHED REPORTS

Journal Articles

JA No.			
4036	Ferromagnetism	J. B. Goodenough	Estratto dal Vol. V della Enciclopedia della Chimica (Uses Edizioni Scientifiche, Firenze, 1976), p. 357
4615	Impurity Gettering in Semi-insulating Gallium Arsenide Using Ion Implantation Damage	C. O. Bozler J. P. Donnelly W. T. Lindley R. A. Reynolds*	Appl. Phys. Lett. 29, 698 (1976)
4618	Transient InSb Spin-Flip Laser – A Measurement of T_1	S. R. J. Brueck A. Mooradian	Opt. Commun. 18, 539 (1976)
4623	High-Efficiency High-Average-Power Second-Harmonic Generation with $CdGeAs_2$	N. Menyuk G. W. Iseler A. Mooradian	Appl. Phys. Lett. 29, 422 (1976)
4636	Selective Black Absorbers Using MgO/Au Cermet Films	J. C. C. Fan P. M. Zavracky	Appl. Phys. Lett. 29, 478 (1976)
4641	Distributed Feedback $Pb_{1-x}Sn_xTe$ Double-Heterostructure Lasers	J. N. Walpole A. R. Calawa S. R. Chinn S. H. Groves T. C. Harman	Appl. Phys. Lett. 29, 307 (1976), DDC AD-A031649
4643	Direct Optically Pumped Multiwavelength CO_2 Laser	M. I. Buchwald* C. R. Jones* H. R. Fetterman H. R. Schlossberg*	Appl. Phys. Lett. 29, 300 (1976)
4678	GaAs $p^+n^-n^+$ Directional-Coupler Switch	F. J. Leonberger J. P. Donnelly C. O. Bozler	Appl. Phys. Lett. 29, 652 (1976)

Meeting Speeches

MS No.			
4067	Recent Advances in Tunable Lasers	A. Mooradian	Sov. J. Quant. Electron. 6, 420 (1976)

*Author not at Lincoln Laboratory.

MS No.			
4169	Ion Beam Etching	H. I. Smith	Proceedings of Symposium on Etching and Pattern Definition (The Electrochemical Society, Princeton, New Jersey, 1976), pp. 133-143
4205	Design of Reflective-Array Surface Wave Devices	J. Melngailis R. C. Williamson J. Holtham R. C. M. Li	Wave Electronics 2, 177 (1976)

* * * * *

UNPUBLISHED REPORTS

Journal Articles

JA No.			
4621	Minority Carriers in Graphite and the H-Point Magnetoreflection Spectra	W. W. Toy* M. S. Dresselhaus* G. Dresselhaus	Accepted by Phys. Rev. B
4647	Multiple-Energy Proton Bombardment in n^+-GaAs	J. P. Donnelly F. J. Leonberger	Accepted by Solid-State Electron.
4681	Preparation and Properties of PbS Crystals with Low Carrier Concentrations	T. C. Harman A. J. Strauss	Accepted by J. Electron. Mater.
MS-4280	CdTe Optical Waveguide Modulators	D. L. Spears A. J. Strauss	Accepted by J. Physique

Meeting Speeches†

MS No.			
4062A	GaAs/GaAlAs and GaInAsP/InP DH Diode Lasers Grown from Supercooled Solutions	J. J. Hsieh	Seminar, RCA Laboratories, Princeton, New Jersey, 12 August 1976
4124	Analog Memory Correlators for Radar Signal Processing	E. Stern	AGARD Symposium, The Hague, Netherlands, 14-17 June 1976
4124A	Wideband Signal Processing with Acoustoelectric SAW Devices	R. C. Williamson	Symposium on Impact of New Technologies in Signal Processing, Aviemore, Scotland, 21-24 September 1976

---

*Author not at Lincoln Laboratory.

† Titles of Meeting Speeches are listed for information only. No copies are available for distribution.

MS No.			
4140C, D	Photoelectrolysis of Water	J. G. Mavroides	Colloquium on Photoelectrolysis, Johns Hopkins University, 8 October 1976; Greater Washington Physics Colloquium, Washington, D.C., 7 October 1976
4177D	Sputtered Films for Solar Energy Applications	J. C. C. Fan	New England ISHM Technical Symposium, Woburn, Massachusetts, 21 September 1976
4177E	Wavelength-Selective Surfaces for Solar Energy Utilization	J. C. C. Fan	Symposium on Optical, Electro-Optical, Laser and Photographic Technology, San Diego, 23-27 August 1976
4230A	$In_xGa_{1-x}As_yP_{1-y}/InP$ Double-Heterostructure Lasers	J. A. Rossi J. J. Hsieh J. P. Donnelly	
4295	Thickness of InP Layers Grown by LPE from Supercooled Solutions	J. J. Hsieh	
4296	Ion Implanted Lo-Hi-Lo Annular GaAs IMPATT Diodes	R. A. Murphy C. O. Bozler J. P. Donnelly R. W. Laton G. A. Lincoln R. W. Sudbury W. T. Lindley L. Lowe* M. Deane*	1976 North American Symposium on Gallium Arsenide and Related Compounds, St. Louis, Missouri, 26-29 September 1976
4298	Conditions for Lattice-Matching in the LPE Growth of GaInAsP Layers on InP Substrates	J. J. Hsieh M. C. Finn J. A. Rossi	
4302	Ion Implantation in GaAs	J. P. Donnelly	
4230B	$In_xGa_{1-x}As_yP_{1-y}/InP$ Double-Heterostructure Lasers	J. J. Hsieh J. A. Rossi J. P. Donnelly	IEEE Semiconductor Laser Conference, Nemu-no-sato, Mie, Japan, 6-8 September 1976
4230C	1.2 μm cw, Room-Temperature GaInAsP/InP DH Diode Lasers	J. J. Hsieh	Seminar, Bell Laboratories, Holmdel, New Jersey, 4 August 1976
4261	Studies of Surface Defect States on TiO_2: Two-Dimensional Surface Phases	V. E. Henrich G. Dresselhaus H. J. Zeiger	XIII International Conference on the Physics of Semiconductors, Rome, Italy, 30 August – 3 September 1976

*Author not at Lincoln Laboratory.

MS No.			
4263A	Theory of Resonant Raman Scattering from Magnetic Excitons in Europium Chalcogenides	S. A. Safran* G. Dresselhaus M. S. Dresselhaus* B. Lax*	XIII International Conference on the Physics of Semiconductors, Rome, Italy, 30 August – 3 September 1976
4263	Theory of Resonant Raman Scattering from Magnetic Excitons in Europium Chalcogenides	S. A. Safran* G. Dresselhaus M. S. Dresselhaus* B. Lax*	International Conference on Magneto-Optics, Zurich, Switzerland, 1-3 September 1976
4265B	High-Nd-Concentration Mini-Lasers and Laser Materials	S. R. Chinn	Seminar, Philips Research Laboratories, Briarcliff Manor, New York, 31 August 1976
4271	X-Ray Lithography	H. I. Smith	1976 International Conference on Solid State Devices, Tokyo, 1-3 September 1976
4274A	Tunable Infrared Lasers and Their Applications	P. L. Kelley	1976 Fall Meeting, Optical Society of America, Tucson, Arizona, 18-22 October 1976
4285	The Influence of Semiconductor Properties on Photoelectrolysis of Water	D. I. Tchernev	International Conference on the Photochemical Conversion and Storage of Solar Energy, London, Ontario, Canada, 24-28 August 1976
4290	Double Reticle Method of Eliminating Repeated Defects in LSI Masks	T. O. Herndon D. L. Smythe, Jr.	INTERFACE '76 Microelectronics Seminar, Monterey, California, 3-6 October 1976
4318	Suppression of Bulk-Wave Scattering Loss in SAW Resonators	J. A. Alusow R. C. M. Li R. C. Williamson	1976 IEEE Ultrasonics Symposium, Annapolis, Maryland, 29 September – 1 October 1976
4319	Convolvers for DPSK Demodulation of Spread Spectrum Signals	J. H. Cafarella S. A. Reible E. Stern R. W. Ralston	
4320	A Continuously Variable Delay Line System	V. S. Dolat R. C. Williamson	
4332	Lincoln Laboratory Program on Thin-Film Photovoltaics	H. J. Zeiger	ERDA Solar Photovoltaic Program Review Meeting, University of Maine, Orono, 3-5 August 1976

*Author not at Lincoln Laboratory.

MS No.			
4345	Application of Laser Technology to Atmospheric Monitoring	A. Mooradian	8th Materials Research Symposium, National Bureau of Standards, Washington, D.C., 20-24 September 1976
4360	Study of Perfect and Imperfect Surfaces Using Ultrahigh Vacuum Spectroscopy Techniques	H. J. Zeiger	Physics Colloquium, Syracuse University, Syracuse, New York, 16 September 1976

ORGANIZATION

SOLID STATE DIVISION

A. L. McWhorter, *Head*
I. Melngailis, *Associate Head*
C. R. Grant, *Assistant*

P. E. Tannenwald

QUANTUM ELECTRONICS

A. Mooradian, *Leader*
P. L. Kelley, *Associate Leader*

Barch, W. E.
Brueck, S. R. J.
Burke, J. W.
Chinn, S. R.
DeFeo, W. E.
Deutsch, T. F.
Fetterman, H. R.
Flemming, M. W.*
Hancock, R. C.
Heckscher, H.
Kildal, H.
Larsen, D. M.
Menyuk, N.
Moulton, P. F.
Osgood, R. M.
Parker, C. D.
Pine, A. S.

ELECTRONIC MATERIALS

A. J. Strauss, *Leader*
H. J. Zeiger, *Associate Leader*

Anderson, C. H., Jr.
Animalu, A. O. E.
Button, M. J.
Delaney, E. J.
Dresselhaus, G.
Dwight, K., Jr.
Fahey, R. E.
Fan, J. C. C.
Feldman, B.
Finn, M. C.
Gay, R. R.*
Henrich, V. E.
Hong, H. Y-P.
Hsieh, J. J.
Iseler, G. W.
Kafalas, J. A.
Kolesar, D. F.
Krohn, L., Jr.
LaFleur, W. J.
Mastromattei, E. L.
Mavroides, J. G.
Mroczkowski, I. H.
Oli, B. A.*
Owens, E. B.
Palm, B. J.
Pantano, J. V.
Pierce, J. W.
Plonko, M. C.
Reed, T. G.
Spura, S.†
Tchernev, D. I.
Tracy, D. M.
Vohl, P.

APPLIED PHYSICS

A. G. Foyt, *Leader*
T. C. Harman, *Assistant Leader*
C. E. Hurwitz, *Assistant Leader*

Belanger, L. J.
Calawa, A. R.
Carter, F. B.
DeMeo, N. L., Jr.
Donnelly, J. P.
Ferrante, G. A.
Groves, S. H.
Leonberger, F. J.
Lind, T. A.
McBride, W. F.
Orphanos, W. G.
Paladino, A. E.
Shen, C. C.
Spears, D. L.
Tsang, D. Z.*
Walpole, J. N.

SURFACE WAVE TECHNOLOGY

E. Stern, *Leader*
R. C. Williamson, *Assistant Leader*

Brogan, W. T.
Cafarella, J. H.
DeGraff, P. D.
Dolat, V. S.
Efremow, N., Jr.
Flanders, D. C.*
Kernan, W. C.
Li, R. C. M.
Melngailis, J.
Ralston, R. W.
Reible, S. A.
Smith, H. I.
Vlannes, N.*

MICROELECTRONICS

W. T. Lindley, *Leader*
F. J. Bachner, *Assistant Leader*

Beatrice, P. A.
Bozler, C. O.
Burke, B. E.
Clifton, B. J.
Clough, T. F.
Cohen, R. A.
Daniels, P. J.
Durant, G. L.
Foley, G. H.
Grant, L. L.
Gray, R. V.
Lincoln, G. A., Jr.
McGonagle, W. H.
Mountain, R. W.
Murphy, R. A.
Pichler, H. H.
Smythe, D. L., Jr.
Wilde, R. E.

---

* Research assistant

† Co-op. student

I. SOLID STATE DEVICE RESEARCH

A. 1000-HOUR CONTINUOUS CW OPERATION OF DOUBLE-HETEROSTRUCTURE GaInAsP/InP LASERS

State-of-the-art fused silica fibers have both minimum attenuation and minimum dispersion in the 1.1- to 1.3-μm region. Diode lasers with emission wavelengths in this region would therefore be optimum light sources for fiber optics communication systems, if they had long enough operating lifetimes. Room-temperature CW operation of GaInAsP/InP double-heterostructure (DH) diode lasers emitting at about 1.1 μm has been reported by Hsieh, Rossi, and Donnelly.[1] In this section, we report the results obtained to date in the first life tests of such devices. The first laser tested has been in continuous CW operation at room temperature in air for over 1000 hr, the second laser for over 600 hr, without degradation in performance. Both lasers, which emit at 1.15 μm, are still in operation.

The GaInAsP/InP lasers are stripe-geometry devices made by proton bombardment of heterostructures prepared by growing successive liquid-phase-epitaxial (LPE) layers of InP, GaInAsP, and InP on (111)B-oriented, melt-grown InP substrates. The thickness, dopant, and carrier concentration of each LPE layer are listed in Table I-1. The stripe width is 13 μm, and the cavity length is 380 to 400 μm. Details of the fabrication procedure have been described earlier.[1]

TABLE I-1
LPE LAYERS OF DOUBLE-HETEROSTRUCTURE GaInAsP/InP LASERS

Layer	Material	Thickness (μm)	Dopant	Carrier Concentration (cm^{-3})
1	n-InP	.2	Sn	4×10^{18}
2	n-$Ga_{0.12}In_{0.88}As_{0.27}P_{0.77}$	0.5	Sn	3×10^{17}
3	p-InP	2	Zn	3×10^{18}

For room-temperature CW operation, each diode is indium-soldered to a copper block. The block is then attached to a copper heat sink through which methanol is cycled to maintain the heat-sink temperature at 24° ± 2°C. The temperature of the active region of the laser during operation is estimated to be 5° to 10°C higher.

During the life tests, the laser output power is monitored continuously with a calibrated silicon solar cell, and the DC operating current is adjusted periodically to keep the output power constant to ±20 percent. The threshold current is checked periodically, and the laser spectrum is measured from time to time by focusing the light into a grating spectrometer provided with a cooled S-1 photomultiplier.

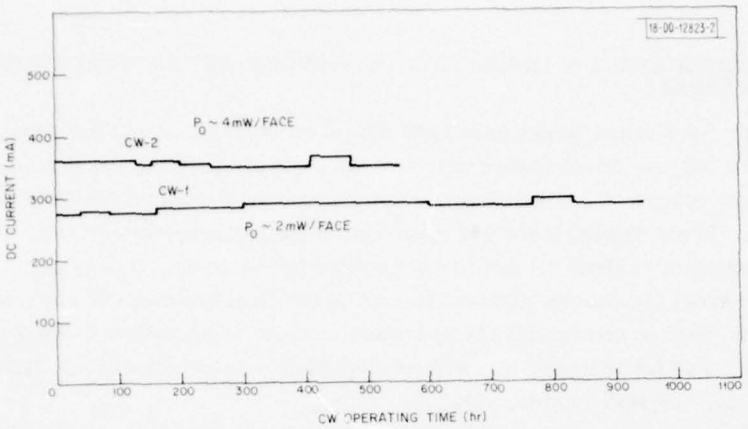

Fig. I-1. Diode current vs operating time for two CW GaInAsP/InP DH lasers with single-facet output powers of 2 and 4 mW (±20 percent), respectively.

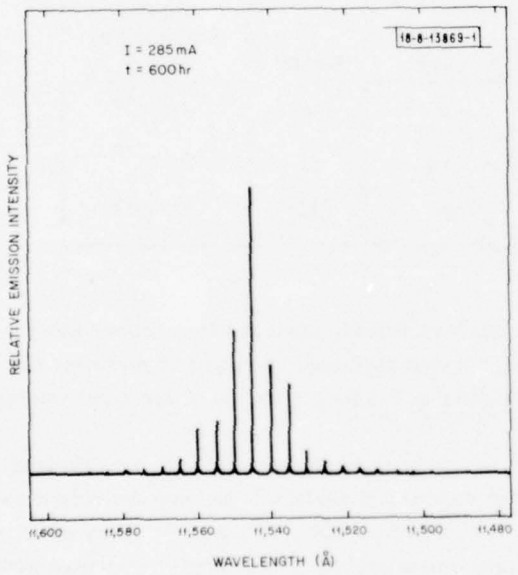

Fig. I-2. Spectrum of laser CW-1 after 600 hr of room-temperature operation.

Figure I-1 shows the diode operating current as a function of time for GaInAsP/InP lasers CW-1 and CW-2 over their first 950 hr and first 550 hr, respectively, of continuous CW operation. No significant variation in the current required to maintain constant output power (2 and 4 mW, respectively) occurred for either device; the small changes in current shown in Fig. I-1 were due to changes in heat-sink temperature, not to laser degradation. The threshold currents (275 and 330 mA, respectively) also varied somewhat with temperature, but otherwise remained constant with time. (After several hundred hours of operation, the laser output at constant current gradually dropped because a thin film formed on the cleaved facets, which had not been protectively coated. After the film was removed by dipping the diode in buffered HF, the output power was restored to its original value.)

Figure I-2 shows the output spectrum of laser CW-1 at 285 mA after 600 hr of continuous operation. The spectrum is identical to that obtained at the same current prior to the life test.

Lasers CW-1 and CW-2 are both still in operation, having now logged over 1000 and over 600 hr, respectively, without any degradation in performance. The fact that such excellent results have been obtained for the first GaInAsP/InP lasers to be life-tested is a very encouraging indication that devices of this type will prove to be sufficiently reliable for use as light sources in fiber optics communication systems. These results also suggest that GaInAsP/InP lasers may not be subject to the same degradation mechanisms that are responsible for the failure of GaAs/GaAlAs lasers. It is of particular interest that the lasers tested were fabricated from heterostructures grown on an InP substrate with a dislocation density of about 5×10^5 cm^{-2}, since GaAs/GaAlAs lasers grown on substrates with such a high dislocation density would have very short lifetimes.

C. C. Shen
J. J. Hsieh
T. A. Lind

B. MULTIPLE-ENERGY PROTON BOMBARDMENT IN n^+-GaAs

It has previously been shown that proton bombardment can be used to create high-resistivity layers in GaAs (Refs. 2 through 7) and $Ga_{1-x}Al_xAs$ (Refs. 7 and 8), and that this technique is a useful device-processing step.[3] It has been used in the fabrication of avalanche photodiodes,[9,10] IMPATT diodes,[11-14] "stripe-geometry" lasers,[7] field-effect transistors,[15] and optical waveguides.[16-18] In this section, we will discuss several areas which have not been previously treated. These include a comparison of the effects of single- and multiple-energy bombardments on the electrical characteristics of n^+-GaAs ($n \geq 10^{18}$ cm^{-3}), and the use of the combination of a multiple-energy bombardment and a post-bombardment anneal to create thermally stable high-resistivity layers in n^+-GaAs. The anneal characteristics of proton-bombarded layers are important since many of the devices in which proton bombardment is used are subject to elevated temperatures through post-bombardment processing and/or operating conditions. More detailed information can be found in Ref. 19.

For n-GaAs with a carrier concentration less than 10^{17} cm^{-3}, a single dose of about 10^{13} cm^{-2} protons is usually sufficient to compensate the entire bombarded layer (for thicknesses $\lesssim 10$ μm).[3] For n^+-GaAs ($n \geq 10^{18}$ cm^{-3}), however, we have found that a single-energy 400-keV proton bombardment cannot effectively compensate the entire 4-μm-thick bombarded layer. These results can be explained by a nonuniform compensation with depth.[5,6] A multiple-energy proton-bombardment schedule which would create a "uniform-damage" region was therefore developed. Using this multiple-energy proton-bombardment schedule, the bombarded layer

TABLE I-2

MULTIPLE-ENERGY PROTON BOMBARDMENTS IN $n = 3 \times 10^{18}$ cm^{-3} GaAs

Proton Bombardment		No Anneal		300°C Anneal		350°C Anneal		400°C Anneal	
Energy (keV)	Dose (cm^{-2})	RA (Ω-cm^2)	C/A† (nF/cm^2)	RA (Ω-cm^2)	C/A† (nF/cm^2)	RA (Ω-cm^2)	C/A† (nF/cm^2)	RA (Ω-cm^2)	C/A† (nF/cm^2)
400	1×10^{15}	1.0×10^{2}	5.2	4.0×10^{3}	3.2	2.0×10^{3}	3.4	1.2×10^{3}	4.2
300	7×10^{14}								
200	5×10^{14}								
100	3×10^{14}								
400	3×10^{15}	8.1×10^{1}	20.0	–	–	6.5×10^{2}	4.1	5.1×10^{3}	3.2
300	2×10^{15}								
200	1×10^{15}								
100	6×10^{14}								

† Capacitance measured at 500 kHz. For ideal 4-μm-thick 10^{8} Ω-cm layer, RA = 4×10^{4} Ω-cm^2 and C/A = 2.8 nF/cm^2.

in n^+-GaAs could be effectively compensated throughout its depth. In fact, the results were found to be very similar to those reported for fast-neutron bombardment in n^+-GaAs (Ref. 20). Without any post-bombardment annealing, there is an optimum dose which results in a maximum resistivity of 10^7 to 10^8 Ω-cm. This dose increases with carrier concentration. For samples bombarded for maximum resistivity without anneal, the resistivity decreases monotonically with increasing anneal temperature. For higher doses, the resistivity is initially lower but increases at first with anneal temperature until it reaches a maximum in the 10^7 to 10^8 Ω-cm range. The optimum anneal temperature increases with dose, and can be as high as 500°C.

Table I-2 lists the resistance-area product RA (measured around zero bias on a curve tracer) and capacitance per unit area C/A (measured on a bridge at 500 kHz) results obtained on two bombarded samples which had initial electron concentrations of 3×10^{18} cm^{-3}. They were bombarded with different total doses and annealed at temperatures up to 400°C. Sample 1 was bombarded with 1×10^{15} cm^{-2} at 400 keV, 7×10^{14} cm^{-2} at 300 keV, 5×10^{14} cm^{-2} at 200 keV, and 3×10^{14} cm^{-2} at 100 keV. Sample 2 was bombarded with 3×10^{15} cm^{-2} at 400 keV, 2×10^{15} cm^{-2} at 300 keV, 1×10^{15} cm^{-2} at 200 keV, and 6×10^{14} cm^{-2} at 100 keV. For an ideal 4-μm-thick 10^8 Ω-cm layer, RA would be 4×10^4 Ω-cm^2 and C/A would be 2.8 nF/cm^2. With no anneal, the RA product of both bombarded samples is quite low and C/A is higher than expected. The capacitance of sample 1 is appreciably lower than that of sample 2. After a 30-min., 300°C anneal, the RA product of sample 1 increases to 4×10^3 Ω-cm^2 (which corresponds to a $\overline{\rho}$ of 10^7 Ω-cm) and the capacitance per unit area decreases to 3.2 nF/cm^2. On all of the annealed samples measured thus far, the minimum capacitance is always 10- to 20-percent higher than expected for an ideal 4-μm layer. This is believed to be due to the annealing of the compensation created by the most deeply penetrating portion of the 400-keV proton bombardment (see Fig. 1 of Ref. 3). No matter how high a compensation uniformity is achieved in the rest of the bombarded layer, this region will always have some decrease in compensation over several standard deviations. For higher anneal temperatures, the RA product of sample 1 decreases with increasing anneal temperature, and C/A increases. For sample 2, RA increases and C/A decreases with anneal temperature up to at least 400°C (the highest anneal temperature used). After the 400°C anneal, the RA product was 5.1×10^3 Ω-cm^2 ($\overline{\rho} = 1.3 \times 10^7$ Ω-cm) and the C/A was 3.2 nF/cm^2.

Table I-3 lists similar data for three samples with an initial electron carrier concentration of 1×10^{18} cm^{-3}. Sample 1 was bombarded with 5.0×10^{14} cm^{-2} at 400 keV, 3.0×10^{14} cm^{-2} at 300 keV, 1.5×10^{14} cm^{-2} at 200 keV, and 1.0×10^{14} cm^{-2} at 100 keV. The dose at each energy for sample 2 was twice that of sample 1, and for sample 3 was twice that of sample 2. For no anneal, RA decreases and C/A increases with increasing total dose. Sample 2 showed a maximum in RA of 2.0×10^{14} Ω-cm^2 and a minimum in C/A of 3.0 nF/cm^2 for anneal temperatures of 350° and 400°C. At 500°C, there was appreciable annealing of the compensation in the bombarded layer. Sample 3 showed an increase in RA and a decrease in C/A up to the highest anneal temperature used, 500°C. After the 500°C anneal, RA was about 1×10^5 Ω-cm^2 ($\overline{\rho} = 2.5 \times 10^8$ Ω-cm) and C/A was 3.2 nF/cm^2.

Figure I-3 shows the I-V characteristics for a 20-mil-diameter gold contact on sample 3 after a 500°C anneal. The leakage current is very small ($\lesssim 1$ μA) out to about 40 V in either bias direction. The forward direction, corresponding to a positive voltage on the gold contact, has a "breakdown voltage" a few volts less than in the reverse direction. In either direction, the average electric field in the bombarded layer at breakdown is $\geqslant 1 \times 10^5$ V/cm.

TABLE I-3

MULTIPLE-ENERGY PROTON BOMBARDMENTS IN $n = 1 \times 10^{18}$ cm^{-3} GaAs

Proton Bombardment		No Anneal		350°C Anneal		400°C Anneal		500°C Anneal	
Energy (keV)	Dose (cm^{-2})	RA (Ω-cm^2)	C/A† (nF/cm^2)	RA (Ω-cm^2)	C/A† (nF/cm^2)	RA (Ω-cm^2)	C/A† (nF/cm^2)	RA (Ω-cm^2)	C/A† (nF/cm^2)
400	5.0×10^{14}	1.4×10^3	3.8	4.0×10^3	3.5	4.0×10^3	4.2	–	–
300	3.0×10^{14}								
200	1.5×10^{14}								
100	1.0×10^{14}								
400	1.0×10^{15}	3.4×10^2	4.8	2.0×10^4	3.0	2.0×10^4	3.0	6.1×10^3 (Diode)	140
300	6.0×10^{14}								
200	3.0×10^{14}								
100	2.0×10^{14}								
400	2.0×10^{15}	2.1×10^2	12	5.0×10^3	3.7	1.0×10^4	3.3	1.0×10^5	3.2
300	1.2×10^{15}								
200	6.0×10^{14}								
100	4.0×10^{14}								

† Capacitance measured at 500 kHz. For ideal 4-μm-thick 10^8 Ω-cm layer, RA = 4×10^4 Ω-cm^2 and C/A = 2.8 nF/cm^2.

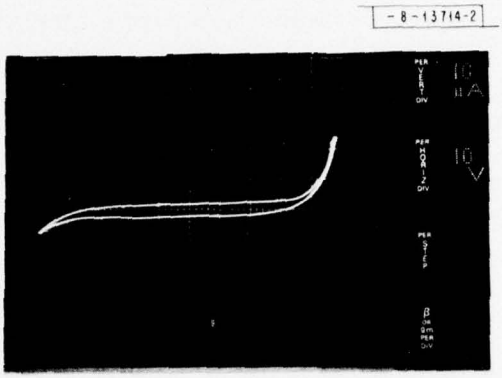

Fig. I-3. Current-voltage characteristics of 20-mil-diameter gold contact on multiple-energy proton-bombarded n^+-GaAs ($n = 1 \times 10^{18}$ cm^{-3}) sample. GaAs was bombarded with proton doses of 2.0×10^{15} cm^{-2} at 400 keV, 1.2×10^{15} cm^{-2} at 300 keV, 6.0×10^{14} cm^{-2} at 200 keV, and 4.0×10^{14} cm^{-2} at 100 keV, and was post-annealed at 500°C for 30 min.

These results indicate that proton-bombarded high-resistivity layers are useful to higher operating temperatures than previously indicated.[5,6] Although the situation is probably extremely complex, it appears that several different compensating levels which anneal at different temperatures are created during the proton bombardment. The density of each compensating level varies with depth for any single-energy bombardment, and for any annealing temperature there is an optimum compensating density which does not anneal out. By using a multiple-energy bombardment, the optimum density can be approximated throughout the entire bombarded region. The concept of "over-bombarding" the sample, i.e., using a higher dose than required for an optimum resistance without anneal and then annealing, has been previously suggested to simultaneously optimize the average resistivity and optical loss of single-energy proton-bombarded p^+-GaAs (Ref. 4). However, in Ref. 4 the average resistivity itself decreased with increasing anneal temperature.

The equivalent parallel AC resistance r and capacitance C of bombarded layers in n^+-GaAs were generally found to vary with measuring frequency. Since rA appears to be inversely proportional to $f^{1/2}$ at higher frequencies, a hopping conductivity[21,22] is very likely occurring in the heavily compensated bombarded region. A tunnel-assisted hopping mechanism has been reported for neutron-bombarded[20] and ion-implanted[23] GaAs. Hopping theory predicts that the real part of the AC conductivity should vary as ω^n, where $\omega = 2\pi f$ and n is between 0.5 and 1.0 (Ref. 22). Therefore, above some frequency f_o, rA (which is inversely proportional to σ) should vary as f^{-n}. The observed dependence corresponds to $n \approx 0.5$. The imaginary part of the AC conductivity which is equal to $\omega P(\omega)$, where $P(\omega)$ is the polarization due to the hopping process, is related to the real part of the AC conductivity through the Kramers-Kronig relation. For the hopping process, $P(\omega)$ decreases with increasing frequency, and therefore the capacitance will decrease with increasing frequency, asymptotically approaching the capacitance expected from the usual dielectric constant of the material. This is the capacitance variation observed. The

capacitance generally decreases with frequencies up to a few hundred kilohertz, above which it is essentially constant.

Although this study is by no means exhaustive and in fact raises several issues that are possible candidates for future investigations, it does show that for at least n^+-GaAs, a multiple-energy proton bombardment is superior to a single-energy bombardment in creating high-resistivity layers, and that an appropriate combination of a multiple-energy bombardment schedule and an anneal, which can be at a temperature as high as 500°C for 10^{18} cm^{-3} material, can result in 10^6 to 10^8 Ω-cm layers in n^+-GaAs.

J. P. Donnelly
F. J. Leonberger

C. LOW-DOSE n-TYPE ION IMPLANTATION INTO Cr-DOPED GaAs SUBSTRATES

Ion implantation in GaAs is finding many applications in the fabrication of microwave and optoelectronic devices. For some of these devices, such as MESFETs[24-28] and planar Gunn devices,[29] epitaxial growth can be eliminated and the fabrication simplified by implanting donors directly into Cr-doped semi-insulating substrates. For these applications, however, low-dose implants (10^{12} to 10^{13} cm^{-2}) must be utilized, and results in this low-dose regime have generally not been reproducible from one Cr-doped ingot to another due to the considerable variation in commercially available material. Screening can be used to select Cr-doped ingots, but this generally results in less than 20 percent of the ingots being acceptable. In this section, we will first present some results of low-dose Se^+ implants into several different Cr-doped ingots. These results will illustrate the substrate-related variations that are generally observed. We will then discuss methods of reducing or eliminating these substrate effects.

Slices with (100) surfaces were cut from the different Cr-doped ingots investigated. These wafers were chemical-mechanically polished on one side. Each wafer was cleaved into several samples which were free-etched in a freshly prepared solution of $5H_2SO_4$:$1H_2O_2$:$1H_2O$. Samples from each wafer were then implanted at 200°C with 400-keV Se^+ ions (or for ingot 3258, 400-keV S^+ ions). Other samples of each wafer, which were processed as controls, were either not implanted or implanted with 400-keV Kr^+ ions. The implanted or polished surface of all the samples (even the unimplanted ones) were then coated with 500 to 700 Å of pyrolytic Si_3N_4. The Si_3N_4 deposition procedure and parameters have been found to be extremely important and will be discussed below. To mechanically protect the thin Si_3N_4 during subsequent handling, ≈2000 Å of SiO_2 was pyrolytically deposited at 400°C over the Si_3N_4. The samples were then annealed at 900°C for 15 min. in flowing N_2. Since 900°C is most likely the highest temperature that will be used in annealing ion-implanted GaAs (Refs. 29 through 34), the above anneal procedure seems appropriate for investigating the variations between Cr-doped ingots.

After annealing, the SiO_2 and Si_3N_4 layers were removed in HF. To minimize contact effects in making Hall measurements of the van der Pauw type,[35] electrically isolated cloverleaf-shaped mesas were defined in the implanted layer using 6000 Å of pyrolytic SiO_2 as an etch mask. Good linear contacts were obtained by alloyed Au-Sn.

Figure I-4 shows the sheet carrier concentration vs implant dose for a series of 400-keV Se^+ implants into six different Cr-doped GaAs ingots. At high doses (>10^{13} cm^{-2}), the results in

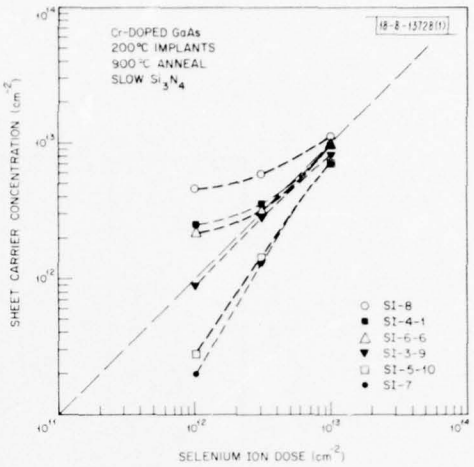

Fig. I-4. Sheet carrier concentration vs dose for six different Cr-doped GaAs ingots implanted with 400-keV Se^+ ions. Samples were implanted bare, encapsulated with "slow" pyrolytic Si_3N_4, and annealed at 900°C for 15 min.

Cr-doped GaAs have been found to be comparable from ingot to ingot. For the low doses shown in Fig. I-4, however, the ingots tend to fall into three general classifications:

(1) Several of the implanted ingots (SI-8, SI-6, and SI-4) exhibit a sheet carrier concentration higher than the implanted dose, i.e., excess carriers. The unimplanted control samples of these ingots (which were encapsulated and annealed) were found to have a thin n-type layer on the surface which had a sheet concentration approximately equal to the number of excess carriers.

(2) Two of the ingots (SI-7 and SI-5) exhibit very low activation (≈20 percent) with a 10^{12}-cm^{-2} implant and no measurable carriers without an implant, i.e., excess compensation.

(3) Only one (SI-3-9) showed the optimum result with both high activation down to low doses and no measurable carriers without an implant. For SI-3-9, the sheet carrier concentration and mobility were 8.5×10^{11} cm^{-2} and 4500 cm^2/V-sec, respectively, for the 10^{12}-cm^{-2} implant.

Although it may be possible to vary the implantation parameters to some extent in each ingot to compensate for the excess carriers or excess compensation, it would be more advantageous to eliminate or reduce the variation in results attributed to the difference between substrates. The ingots that exhibit "excess carriers" will be discussed first, and it will be shown that an improved Si_3N_4 deposition procedure can reduce or eliminate the excess carriers. The ingots that exhibit "excess compensation" will then be discussed, and it will be shown that an ion-implantation gettering technique can reduce or eliminate the excess compensation.

Surface layers of excess carriers similar to those observed on SI-4, SI-6-6, and SI-8 have been observed by others on Cr-doped GaAs annealed using both chemical vapor-deposited Si_3N_4 (Ref. 36) and sputtered Si_3N_4 (Ref. 26). In Ref. 36, the excess carriers were correlated to the

TABLE I-4

EFFECTS OF HEATUP TIME AND TIME AT TEMPERATURE DURING THE Si_3N_4 DEPOSITION ON UNIMPLANTED AND 400-keV Se^+ ION-IMPLANTED Cr-DOPED GaAs INGOTS SI-6-6 AND SI-8. ALL SAMPLES WERE ANNEALED AT 900°C FOR 15 MINUTES.

Deposition Parameters for ≈500-Å Si_3N_4			SI-6-6 N_s (cm^{-2})		SI-8 N_s (cm^{-2})	
			No Implant	1×10^{12} Se^+/cm^2	No Implant	1×10^{12} Se^+/cm^2
Slow Si_3N_4	25° to 720°C	16 sec	1.4×10^{12}	2.3×10^{12}	4.2×10^{12}	4.7×10^{12}
	At 720°C	60 sec				
Fast Si_3N_4	200° to 690°C	6 sec	$(0.6 \text{ to } 2.0) \times 10^{11}$	$(6 \text{ to } 9) \times 10^{11}$	1.8×10^{12}	Not done
	At 690°C	9 sec				

concentrations of Cr and Si in the GaAs substrates. Although we have made mass spectrographic analyses of all the ingots used in these experiments, we have not been able to obtain any simple correlation between results and impurity concentrations.

To determine at what point in the process the "excess" n-type skins were formed, several additional samples of SI-6-6 and SI-8 were encapsulated with Si_3N_4 but not annealed at 900°C. The n-type skins were not formed, indicating that the high-temperature anneal was necessary to form the n-type skins. Various nitride deposition parameters were therefore varied in an attempt to improve the encapsulating quality of the pyrolytic Si_3N_4. It was found that appropriate modification of the encapsulation procedure could in fact substantially reduce the number of excess carriers on those ingots that fall into category (1).

All the data shown in Fig. I-4 were obtained using what will be referred to as a slow pyrolytic Si_3N_4. What is meant by a slow nitride is outlined in Table I-4. The procedure for depositing the slow pyrolytic Si_3N_4 is essentially that originally described in Ref. 30, except that the heating time to reach the deposition temperature is longer. For the slow nitride, the SiH_4, ammonia and nitrogen dilution flow rates are established. The GaAs substrate is then heated from room temperature to 720°C in 16 sec. It takes an additional 60 sec to deposit a 500-Å Si_3N_4 layer. By decreasing the heatup time and increasing the growth rate of the Si_3N_4, the excess carriers observed can generally be reduced substantially. The best results have been obtained using essentially the same deposition procedure used in the fabrication of ion-implanted lo-hi-lo IMPATT diodes.[31] Films deposited by this process will be referred to as fast pyrolytic Si_3N_4. The growth rate of the Si_3N_4 was increased by increasing the flow rates of the reactant gases to 500 scc/min. of 5-percent SiH_4 in N_2 further diluted in 500 scc/min. of N_2, and 1000 scc/min. of NH_3 diluted in 250 scc/min. of N_2. Since it was observed that the silane could react at room temperature with trace amounts of oxygen in the reactor chamber causing a predeposition on the sample, for the fast nitride the samples were heated to 200°C before the introduction of the silane, eliminating the predeposition. With all the gases present, the sample is heated from 200° to 690°C in 6 sec. It takes nine additional seconds at 690°C to deposit a 500-Å film of silicon nitride.

Table I-4 summarizes the results obtained on ingots SI-6-6 and SI-8 with the slow and fast nitrides. Every sample of these two ingots, which were annealed with a fast nitride encapsulation, had an excess sheet carrier concentration which was substantially less than that observed with a slow nitride. Ingot SI-8 has shown the largest number of excess carriers that we have observed on any ingot, but even here the fast nitride reduced the excess surface electrons without an implant from 4.2×10^{12} cm^{-2} to 1.8×10^{12} cm^{-2}. For unimplanted samples of SI-6-6 annealed with a fast nitride, the excess carriers were reduced to a small fraction of a typical FET or Gunn channel implant dose. The lowest value observed with a fast nitride was 6×10^{10} cm^{-2}, while the highest was 2×10^{11} cm^{-2}. The average excess sheet concentration without an implant was 1×10^{11} cm^{-2}. On control samples of SI-6-6 that were implanted at 200°C with 400-keV Kr^+ ions, the excess surface conduction was, if anything, smaller than that observed on unimplanted control samples. With a 1×10^{12} cm^{-2} Se implant, samples of SI-6-6 which were encapsulated with a fast nitride exhibited sheet concentrations of (6 to 9) $\times 10^{11}$ cm^{-2}. The percent scatter in these data should be much less at the more typical channel implant doses of $(\gtrsim 2) \times 10^{12}$ cm^{-2}.

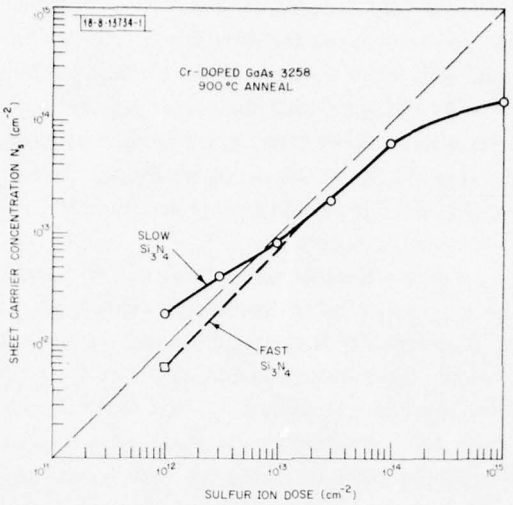

Fig. I-5. Sheet carrier concentration vs dose for 400-keV S^+-implanted Cr-doped GaAs ingot 3258. Samples were implanted bare, encapsulated with a slow or fast Si_3N_4, and annealed at 900°C for 15 min.

TABLE I-5

THE EFFECTS OF Ne^+ ION-IMPLANTATION DAMAGE-GETTERING ON THE ACTIVATION OF 400-keV Se^+ IONS IMPLANTED INTO Cr-DOPED GaAs INGOT SI-7. ALL THE SAMPLES WERE ANNEALED AT 900°C FOR 15 MINUTES.

GaAs SI-7	Sheet Carrier Concentration (cm^{-2})	
	No Implant	1×10^{12} Se^+/cm^2
Without gettering	Not measurable	1.9×10^{11}
With Ne^+ gettering	Not measurable	8.0×10^{11}

On a more recently acquired ingot, number 3258, excess carriers were reduced to an unmeasurable value using the fast nitride. Figure I-5 shows the results of some sulfur implants into this crystal of Cr-doped GaAs. With the slow Si_3N_4 procedure, excess carriers were observed. With the fast Si_3N_4, there were no measurable excess carriers without an implant and a reasonable activation ($N_s = 6.3 \times 10^{11}$ cm^{-2}) was achieved for a 10^{12}-cm^{-2} S^+ implant.

For ingots in which there is a low activation of implanted ions at low doses, another procedure – ion-implantation damage-gettering – has resulted in a reduction in excess compensation. Ion-implantation damage-gettering in GaAs has been used previously to reduce the outdiffusion of compensating impurities or defects from the Cr-doped substrate into epitaxial layers.[37] A sample of ingot SI-7 was bombarded at room temperature with 1×10^{16}-cm^{-2} 400-keV Ne^+ ions and then annealed for 16 hr with an Si_3N_4 cap. After anneal, the Si_3N_4 was removed by reactive ion etching using a mixture of 5-percent O_2 and CF_4. The plasma etch was necessary for nitride removal because the usual HF chemical technique left a film of relatively inert material on the surface, which interfered with subsequent chemical-etch steps. A 3-μm layer was then removed from the Ne^+-damaged surface using a room-temperature $5H_2SO_4:1H_2O_2:1H_2O$ etching solution. Implants were made into the same surface that was previously damaged. Further details of the gettering procedure can be found in Ref. 37.

Table I-5 summarizes the implantation results obtained on gettered and nongettered samples of Cr-doped ingot SI-7. For the sample which was not gettered, a 10^{12}-cm^{-2} Se^+ implant resulted in a sheet carrier concentration of only 1.9×10^{11} cm^{-2}. This can be compared with an Ne^+-gettered substrate in which no excess carriers could be measured without an implant, while for a 10^{12}-cm^{-2} implant, a sheet carrier concentration of 8×10^{11} cm^{-2} with a mobility of 4300 cm^2/V-sec was measured.

In conclusion, it has been shown that when low-dose n-type implants are made directly into Cr-doped GaAs, anomalous results are obtained on a large percentage of commercially available ingots. The variation between different materials may result in a thin n-type skin of "anomalous excess carriers" in some ingots, and a low activation of the implanted ions in others. On the ingots that show excess carriers, an improved encapsulation procedure can substantially reduce, and in some cases eliminate entirely, the excess sheet concentration. On the ingots that show low activation, an ion-implantation damage-gettering technique can be used to increase the activation of implanted ions to $\gtrsim$80 percent. These procedures, when used prudently, should encourage a wider use of fabricating ion-implanted devices directly in Cr-doped semi-insulating GaAs.

J. P. Donnelly W. T. Lindley
C. O. Bozler G. A. Ferrante

D. SURFACE OUTDIFFUSION IN n-CdTe

Schottky-barrier capacitance measurements have revealed that moderate heating of n-type CdTe wafers produces a large drop in carrier concentration near the surface. These compensated layers (about 1000 Å thick for a 60-min., 150°C heat treatment) can be very detrimental to many devices, particularly photoemitters.[38] This effect is presumably due to outdiffusion of cadmium.[39]

The measurements were carried out on bromine-doped CdTe wafers with 4.5×10^{17} carriers/cm^3, and on indium-doped wafers with about 2×10^{16} carriers/cm^3. The wafers were polished and etched in 10-percent bromine-methanol, and then heated either in air or in a nitrogen ambient; 9-mil-diameter gold Schottky barriers were then electroplated onto one surface

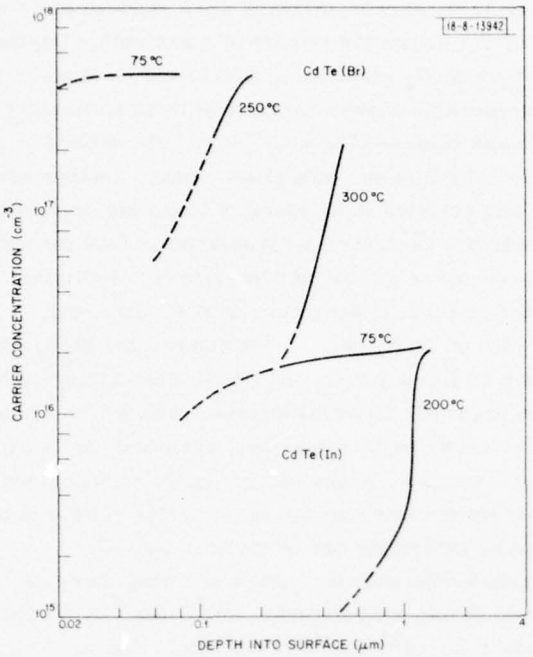

Fig. I-6. Carrier concentration as a function of depth into surface of CdTe wafers heated for 60 min. at different temperatures.

through a photoresist mask. Heating during the photomasking procedure was roughly equivalent to heating for 1 hr at 75°C. Capacitance-voltage measurements at 1 MHz were made on several devices on each wafer. Figure I-6 shows the carrier concentration as a function of depth into the surface for five typical 60-min. anneals. Concentration profiles given by the solid lines were obtained from differential capacitance data. The dashed lines are extrapolations based upon the zero-bias capacitance data and assuming a 0.71-V barrier height[40] between the gold and CdTe. This barrier gives rise to a depletion layer at zero bias of about 400 and 2000 Å in the In- and Br-doped samples, respectively.

The exact value of carrier concentration at the surface of the annealed wafers is not known; however, it is clearly orders of magnitude below the bulk value. Considerable variation from anneal to anneal was found which did not seem to be a function of ambient conditions. For example, the outdiffusion depth (defined as the depth where the carrier concentration was one-half the bulk value) for the 250°C anneals varied from 0.12 to over 1 μm. Coating the wafers with either 4000 Å of sputtered ZnS or 3000 Å of pyrolytic SiO_2 before annealing did not retard the outdiffusion effect. Indeed, the 5 min. at 350°C required to deposit the SiO_2 produced more outdiffusion than the 60-min., 250°C anneal. Other coatings are currently being explored.

D. L. Spears

E. LIQUID-PHASE EPITAXIAL GROWTH OF $PbS_{1-x}Se_x$ ALLOYS

The double-heterostructure (DH) configuration has made it possible for $Pb_{1-x}Sn_xTe$ diode lasers to routinely operate CW at liquid-nitrogen temperature and above. The short wavelength limit of these diodes is ~6 μm, which corresponds to the energy bandgap of PbTe. $PbS_{1-x}Se_x$ DH diodes could extend the wavelength range to 4 μm, which corresponds to the bandgap of PbS. Recently, Preier et al.[41] have demonstrated CW operation up to 96 K with $PbS_{1-x}Se_x$ DH diodes

grown by the hot-wall epitaxial technique. We report here on a preliminary investigation of the liquid-phase epitaxial (LPE) growth of $PbS_{1-x}Se_x$ from Pb-rich growth solutions. Several growth problems have been identified, and some progress has been made toward solving them. Growth of the preferred structure, consisting of two n-type epitaxial layers on a p-type substrate, probably can be made only if a high sulfur pressure is maintained in the growth tube, preventing the rapid loss of sulfur from the substrate and the resulting carrier-type conversion that has occurred in our experiments.

Growth of high-quality epitaxial PbS and $PbS_{1-x}Se_x$ alloys is considerably more difficult than that of $Pb_{1-x}Sn_xTe$. An atmosphere other than H_2 must be used because of the partial conversion of the sulfur component of the PbS substrate to H_2S at growth temperatures. We have generally used helium gas passed over a titanium getter to remove O_2, and on occasions we have successfully used nitrogen. A more difficult problem is the lack of a suitable etch that gives a highly polished surface on the PbS substrate. Hot aqua regia yields a better surface than other etches, but it leaves a surface roughness of ~0.1 μm (see Ref. 42). This surface is similar in appearance to the vapor-etched surfaces, caused by the action of H_2 at temperatures above 500°C, that must be prevented for successful LPE growth. Surfaces that have been mechanically etch-polished are reasonably smooth and have been used for most of our studies, with the recognized disadvantages of some surface damage and probably some surface oxidation.

Liquidus data for solutions of $Pb_{1-y}S_y$ and $Pb_{1-y}(S_{0.69}Se_{0.31})_y$ are shown in Fig. I-7. For the comparison of LPE growth of these materials with the $Pb_{1-x}Sn_xTe$ alloys, we note that the solubility of S in Pb over the growth temperature range of 450° to 700°C is roughly ten times less than that of Te in Pb. Furthermore, only a degree or two of undercooling of the $Pb_{1-y}S_y$ solution is possible. This undesirable characteristic can be overcome in the case of PbTe growth by cooling at rates in excess of 1°C/min., which apparently drives the solution downward in temperature fast enough to give an adequate nucleation density for smooth growth. Cooling rates in excess of 20°C/min. have been necessary to produce continuous growth of PbS, presumably because of the lower solubility. Figure I-8 shows a photomicrograph of a layer grown at >20°C/min. There is some evidence that the waviness could be reduced by more accurate orientation of the substrate to the ⟨100⟩ direction (see p. 12 in Ref. 38). Growth on a (111) surface did not yield good films, nor did attempts at using meltback to etch the surface.

The preferred geometry for a Pb-salt DH diode laser consists of a p-type substrate, an n- or p-type active layer, and an n-type final layer. Either by masking before growth or by mesa-etching after growth, a stripe geometry is formed with the broad-area contact on the p-type substrate; this configuration is preferred because of the greater difficulty in making low-resistance contacts to the p-type material. An important factor to the success of the $Pb_{1-x}Sn_xTe$ heterostructure lasers was discovering that Tl-doped PbTe remains p-type when Pb-saturated and, in particular, when the substrate is contacted with the metal-rich growth solution. Unfortunately, there is no known impurity that will keep PbS p-type when Pb-saturated. It was our hope that a rapid LPE growth (several minutes) and cool-down would cause only a small shift of the p-n junction, and the advantages of the DH diode would be retained.

This optimism was ill-founded for several reasons. Although the epilayers can be grown in several minutes, heating the furnace and establishing starting conditions takes half an hour or more. The sulfur pressure over sulfur-rich (p-type) PbS can amount to several atmospheres at LPE growth temperatures; consequently, just covering the substrate to protect it from direct exposure to the atmosphere during this time will not prevent loss of sulfur and type conversion.

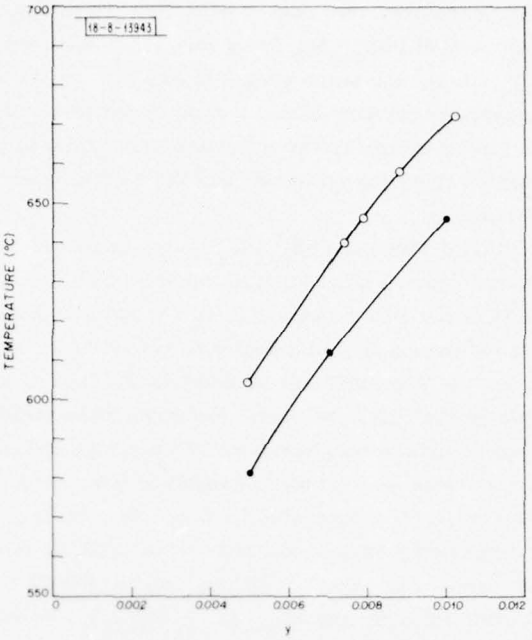

Fig. I-7. Liquidus data for growth solutions of $Pb_{1-y}S_y$ (○) and $Pb_{1-y}(S_{0.69}Se_{0.31})_y$ (●), which were taken by visual determination in a transparent furnace.

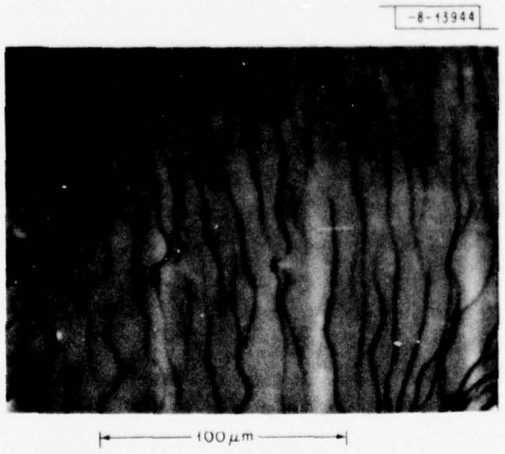

Fig. I-8. Photomicrograph of PbS LPE layer, several micrometers thick, grown on PbS substrate of (100) orientation. Cooling rate was in excess of 20°C/min., and growth was initiated at ~600°C.

The lower the growth temperature the less the loss of sulfur, but the low solubility makes it difficult to grow continuous layers below ~550°C. The loss of sulfur also causes a surface roughening, which aggravates the nucleation and growth problems. We have tried several growths on substrates with $p \simeq 3 \times 10^{18}$ cm^{-3} and on substrates which, in addition, were Tl-doped. In all cases, most or all of the substrate converted to n-type, and surface roughness prevented good growth.

From this preliminary study, it is clear that other approaches are necessary to make DH diodes by the LPE technique. Workers at Rockwell[43] have found that it is possible to grow p-type epilayers of PbS from solutions containing Ag. This is unexpected, because Ag-doped PbS has not remained p-type when Pb-saturated,[44] nor does Ag doping give p-type, vapor-grown PbS (Ref. 43). Another approach would be to grow an entirely n-type heterostructure and then diffuse in a p-n junction. With either of these approaches, one would have to settle for the less desirable p-on-n structure. An alternative would be to provide a sulfur-rich atmosphere, possibly using H_2S, to keep the substrate p-type prior to growth.

S. H. Groves

REFERENCES

1. J. J. Hsieh, J. A. Rossi, and J. P. Donnelly, Appl. Phys. Lett. 28, 709 (1976), DDC AD-A028550/2.
2. K. Wohlleben and W. Beck, Z. Naturf. 21A, 1057 (1966).
3. A. G. Foyt, W. T. Lindley, C. M. Wolfe, and J. P. Donnelly, Solid-State Electron. 12, 209 (1969), DDC AD-694145.
4. J. C. Dyment, J. C. North, and L. A. D'Asaro, J. Appl. Phys. 44, 207 (1973).
5. B. R. Pruniaux, J. C. North, and G. L. Miller, in Proceedings of Second International Conference on Ion Implantation in Semiconductors, 1971 (Springer-Verlag, Berlin, Heidelberg, New York, 1971), p. 212.
6. H. Haradu and M. Fumimoto, in Proceedings of Fourth International Conference on Ion Implantation in Semiconductors, 1974 (Plenum Press, New York, London, 1975), p. 73.
7. J. C. Dyment, L. A. D'Asaro, J. C. North, B. I. Miller, and J. E. Ripper, Proc. IEEE 60, 726 (1972).
8. P. N. Favennec and D. Diguet, Appl. Phys. Lett. 23, 546 (1973).
9. W. T. Lindley, R. J. Phelan, Jr., C. M. Wolfe, and A. G. Foyt, Appl. Phys. Lett. 14, 197 (1969), DDC AD-694323.
10. G. E. Stillman, C. M. Wolfe, J. A. Rossi, and J. P. Donnelly, Appl. Phys. Lett. 25, 671 (1974), DDC AD-A006705/8.
11. R. A. Murphy, W. T. Lindley, D. F. Peterson, A. G. Foyt, C. M. Wolfe, C. E. Hurwitz, and J. P. Donnelly, in Gallium Arsenide and Related Compounds (The Institute of Physics, London, 1973), p. 224, DDC AD-771891/9.
12. R. A. Murphy, W. T. Lindley, D. F. Peterson, and P. W. Staecker, in 1974 IEEE S-MTT International Microwave Symposium Digest of Technical Papers (IEEE, New York, 1974), p. 315.
13. I. S. Groves, J. D. Speight, P. Leight, N. McIntyre, S. O'Hara, and P. Hemment, in Proc. 4th European Microwave Conference (Microwave Exhibitions and Publishers, Ltd., Kent, England, 1974), p. 163.
14. J. D. Speight, P. Leight, N. McIntyre, I. S. Groves, S. O'Hara, and P. Hemment, Electron. Lett. 10, 98 (1974).
15. B. R. Pruniaux, J. C. North, and A. V. Payer, IEEE Trans. Electron Devices ED-19, 672 (1972).

16. E. Garmire, H. Stoll, A. Yariv, and R. G. Hunsperger, Appl. Phys. Lett. 21, 87 (1972).

17. S. Somekh, E. Garmire, A. Yariv, H. L. Garvin, and R. G. Hunsperger, Appl. Phys. Lett. 22, 46 (1973).

18. P. N. Favennec and E. V. K. Rao, in Proc. Fourth Intl. Conf. on Ion Implantation in Semiconductors, 1974 (Plenum Press, New York, London, 1975), p. 65.

19. J. P. Donnelly and F. J. Leonberger, Solid-State Electron. (to be published).

20. R. Coates and E. W. J. Mitchell, Adv. Phys. 24, 593 (1975).

21. M. Pollak and T. H. Geballe, Phys. Rev. 122, 1742 (1961).

22. A. K. Jonscher, J. Non-Crystalline Solids 8-10, 293 (1972).

23. Y. Kato, T. Shimada, Y. Shiraki, and K. F. Komatsubara, J. Appl. Phys. 45, 1044 (1974).

24. R. G. Hunsperger and N. Hirsh, Solid-State Electron. 18, 349 (1975).

25. J. A. Higgins, B. M. Welch, F. H. Eisen, and G. D. Robinson, Electron. Lett. 12, 18 (1976).

26. W. Keller, H. Kniepkamp, R. Restow, and H. Boroffka, in 1975 Technical Digest of the International Electron Devices Meeting (IEEE, New York, 1975), p. 187.

27. G. O. Ladd, R. E. Lundgren, E. C. Cleary, and N. Hirsh, in 1976 Proc. Intl. Solid State Circuits Conference, Philadelphia (IEEE, New York, 1976), p. 169.

28. J. A. Higgins, B. M. Welch, F. H. Eisen, and G. D. Robinson, Electron. Lett. (to be published).

29. T. Mizutani and K. Kurusadu, Electron. Lett. 11, 639 (1975).

30. J. P. Donnelly, W. T. Lindley, and C. E. Hurwitz, Appl. Phys. Lett. 27, 41 (1975), DDC AD-A016690/0.

31. C. O. Bozler, J. P. Donnelly, R. A. Murphy, R. W. Laton, R. W. Sudbury, and W. T. Lindley, Appl. Phys. Lett. 29, 123 (1976), DDC AD-A030622.

32. F. H. Eisen, B. M. Welch, K. Gamo, T. Inada, H. Mueller, M-A. Nicolet, and J. W. Mayer, in Applications of Ion Beams to Materials, G. Carter, J. S. Colligan, and W. A. Grant, Eds. (The Institute of Physics, London, 1976), p. 44.

33. K. Gamo, T. Inada, S. Krekeler, J. W. Mayer, F. H. Eisen, and B. M. Welch, Solid-State Electron. (to be published).

34. F. H. Eisen, B. M. Welch, K. Gamo, T. Inada, and J. W. Mayer, Solid-State Electron. (to be published).

35. L. J. van der Pauw, Philips Res. Rep. 13, 1 (1958).

36. C. A. Stolte, in Tech. Digest of the Intl. Electron Devices Meeting, Washington, D.C., 1975 (IEEE, New York, 1975), p. 585.

37. C. O. Bozler, J. P. Donnelly, W. T. Lindley, and R. A. Reynolds, Appl. Phys. Lett. 29, 698 (1976).

38. Solid State Research Report, Lincoln Laboratory, M.I.T. (1976:3), p. 35, DDC AD-A034647.

39. A. J. Strauss, in Proceedings of the International Symposium on Cadmium Telluride, Strasbourg, France, 29-30 June 1971, P. Siffert and C. Cornet, Eds. (Centre de Recherches Nucléaires, Strasbourg, 1971), p. I-1.

40. C. A. Mead and W. G. Spitzer, Phys. Rev. 114, A713 (1964).

41. H. Preier, M. Bleicher, W. Riedel, and H. Maier, Appl. Phys. Lett. 28, 669 (1976).

42. G. A. Ferrante, M. C. Lavine, T. C. Harman, and J. P. Donnelly, J. Electrochem. Soc. 120, 310 (1973), DDC AD-759092.

43. A. M. Andrews, D. T. Cheung, and E. R. Gertner, Technical Report, Rockwell International Science Center, Thousand Oaks, California (July 1975), DDC AD-B005917.

44. A. J. Strauss, private communication.

II. QUANTUM ELECTRONICS

A. NdLa PENTAPHOSPHATE LASERS

Because of the availability of large (~1 cm^3) crystals of $Nd_xLa_{1-x}P_5O_{14}$ (NdLaPP), we carried out calculations and preliminary experiments to examine the feasibility of making low-threshold, high-efficiency lasers as a replacement for low-power Nd:YAG lasers in some applications. With larger-radius cavity reflectors and longer crystals, such lasers would have mode volumes three orders of magnitude larger than the NPP lasers which we have previously reported,[1] but could still be several times smaller than Nd:YAG lasers.

In order to make comparisons among several configurations, we used the standard laser rate equations and generalized them to allow for the spatial nonuniformity of both the laser mode and excitation density. To avoid undue complexity, the calculations were carried out only for low-excitation, single-mode lasers, and thermal effects were neglected. The general steady-state equation describing such a laser is:

$$\int dV \frac{\left(\beta N - \frac{N}{\tau}\frac{\sigma^A}{\sigma^B}\right) F(r)}{1 + \mathcal{P} F(r)} = \frac{\pi w^2}{4\sigma^B \tau} (L + T)$$

where

βN = excitation rate/unit volume

N = Nd-ion density

σ^A = effective stimulated absorption cross section from terminal laser manifold

σ^B = effective stimulated emission cross section from upper laser manifold

$F(r)$ = spatial distribution of laser mode

$\mathcal{P}$ = saturation parameter

w = laser mode waist

τ = spontaneous fluorescence lifetime

L = internal laser loss/round trip

T = output mirror transmission.

The saturation parameter is given by $\mathcal{P} = 4P_L/\pi w^2 I_s$, where P_L is the one-way internal laser power, and $I_s = h\nu/\sigma^B\tau$ is the saturation power density. The mode distribution has a standing-wave sinusoidal z variation, and a Gaussian transverse variation. For low excitation levels, the integral can be evaluated by first expanding the denominator to order $\mathcal{P}^2$, and carrying out the spatial integrals and the implicit integration over the pump wavelength dependence of βN. The condition $\mathcal{P} = 0$ determines threshold, and the laser power can be found by solving the equation for $\mathcal{P} > 0$.

In order to obtain the excitation rate/unit volume βN, one must know: (1) the geometry of the excitation source, laser rod, and imaging optics; (2) the spectral density of the excitation; and (3) the absorption coefficients of the laser material. We have carried out measurements of the absorption spectrum in NdLaPP and 1-percent Nd:YAG, and have performed calculations for items (1) and (2) in which the pump is either longitudinal solar excitation or transverse, tungsten lamp (black-body) excitation.

Because of the large number of variable parameters involved in the comparisons, the results are too lengthy to present here in detail; thus, only general qualitative results will be given. First, NdLaPP is superior to Nd:YAG for broadband transverse excitation because of its larger pump absorption. The effect of varying the Nd concentration is quite complex, since it simultaneously changes the amount and distribution of pump absorption, the fluorescence lifetime, and the terminal-state absorption (resonant loss). The numerical calculations show that the optimum concentration of Nd varies with pump, laser, and cavity parameters, but is typically about 20 percent. Comparing Nd:YAG and NdLaPP lasers capable of similar output power, the NdLaPP laser could have three times lower threshold, and ten times smaller rod volume.

Second, for longitudinal broadband (i.e., solar) excitation, Nd:YAG is a slightly better laser material. This slight superiority depends on having an Nd:YAG rod long enough (typically, about 3 cm) so that the weaker Nd:YAG absorption is compensated for by the longer rod. It should be noted that we have used a conservative value of $\sigma^B = 1.3 \times 10^{-19}$ cm^2 for NdLaPP, derived from the data of Ref. 2. If the value of $\sigma^B = 2.0 \times 10^{-19}$ cm^2 from Ref. 3 were used, the performance of solar, longitudinally pumped NdLaPP and Nd:YAG lasers would be comparable. Typical NdLaPP parameters would be 10-percent Nd concentration and 1-cm rod length.

We have begun laser experiments in evaluating the performance of larger mode volume NdLaPP lasers, using a confocal cavity with 10-cm mirror separation. This gives a mode waist of 130 μm, and a mode area approximately 100 times larger than in previous experiments with a concentric cavity.[1] Using chopped dye laser excitation, the most significant result so far is the success in lasing a 3.3-mm-long crystal of $Nd_{0.5}La_{0.5}P_5O_{14}$, having polished 'c' faces as the laser facets. This appears to be the most practical orientation, since it allows use of the highest gain 'b' polarization for the laser mode, and uses laser facets normal to the c-axis, which is the easiest plane to polish well. Crystallographic twins (corresponding to different orientations of the monoclinic space group axes) which appeared because of cutting and polishing stresses were deliberately not removed to verify that they had no effect on the laser performance in this orientation. This is the first direct observation of lasing perpendicular to the twin walls in NdLaPP, with about 20 domains being present along the 3.3-mm crystal. (In Ref. 4, a similar geometry was reported, but because of their mounting method for the much thinner crystals, any domains present could not be observed.) We are continuing similar experiments with improved thermal mounting of the laser crystals to offset the larger heat dissipation in the increased mode volume.

S. R. Chinn
W. K. Zwicker†

---

† Philips Laboratories, Briarcliff Manor, New York.

B. PASSIVE Q-SWITCHING AND FREQUENCY DOUBLING

The average second-harmonic power generated in $CdGeAs_2$ using a Q-switched CO_2 laser has been limited by the available laser power.[5] To obtain increased pump power while operating at a high pulse rate, we are now using a double-tube system with an intracavity gas cell which can be filled with a saturable absorber to passively Q-switch the laser. The laser is designed to operate with a flowing gas system and is water-cooled. The optical cavity is 355 cm long × 15 mm diameter and is presently operating with a 100 ℓ/mm grating and an 85-percent reflecting, 10-m-radius GaAs mirror. In addition, there are two gold-coated mirrors in the cavity to "fold" the laser. The cell containing the saturable absorber has a median length of 2.8 in. and uses ZnSe Brewster windows. With the evacuated cell in the cavity, the CW laser output power on the P(20) line of the 10.6-μm band is 20 W for a tube current of 12.5 mA, increasing to 30 W at 22.5 mA. The output is all in a single CO_2 laser transition line and is largely, but not exclusively, in the TEM_{00} mode.

1. SF_6 Absorber and Frequency-Doubling

The laser was passively Q-switched by the addition of a mixture of SF_6 and He to the intracavity cell. The pulse repetition rate (PRR), shape, width, and stability of the resulting pulses are complicated functions of the tube current, mode quality, and transition line of the laser as well as of the gas mixture. It was found that stable Q-switched pulses of the P(20), 10.6-μm transition, with pulse widths between 200 and 250 nsec and PRRs between 15 and 35 kHz were obtainable over a fairly broad range of gas mixtures. Most frequency-doubling experiments were conducted within this set of values.

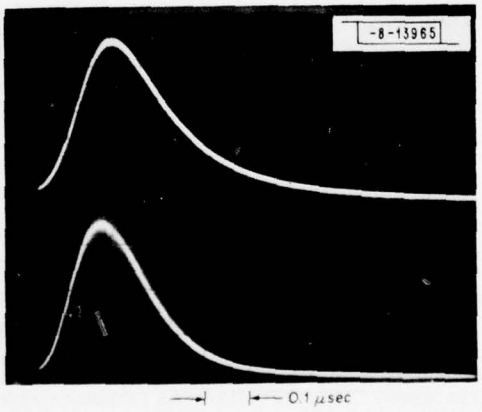

Fig. II-1. Oscilloscope traces of passively Q-switched CO_2 laser pump pulse and corresponding second-harmonic pulse for 16-kHz pulse rate. Upper trace: 10.6 μm, E = 475 μJ; lower trace: 5.3 μm, E = 70 μJ.

The second-harmonic generation was obtained by focusing the laser output onto an antireflection coated $CdGeAs_2$ crystal, as previously described.[6] An oscilloscope trace showing typical shapes of both the passively Q-switched CO_2 laser pulse and the corresponding frequency-doubled pulse are given in Fig. II-1. The CO_2 laser pulse shown has a 225-nsec width (FWHM) with a 16-kHz PRR, and was obtained with a gas cell mixture of 0.25-Torr SF_6 and 2.5-Torr He.

The higher power levels available with the new laser enabled us to extend our previous study of second-harmonic generation.[5] The results are given in Fig. II-2 where it is seen that an average second-harmonic power level of 1.9 W at 5.3 μm has been generated by a $CdGeAs_2$ crystal

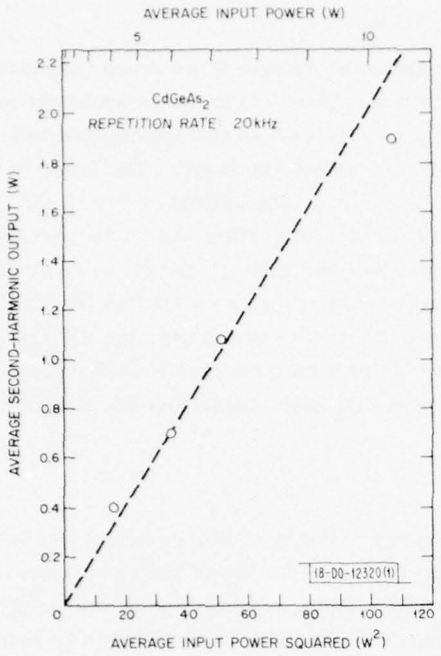

Fig. II-2. Average second-harmonic power output of $CdGeAs_2$ at 5.3 μm as a function of square of average passively Q-switched CO_2 pump power at PRR = 20 kHz.

irradiated from a focused 10.6-μm pump source with 10.4 W average power at a 20-kHz PRR. This is almost 2.5 times the highest value (0.79 W) previously reported.[6] The 1.9-W point in Fig. II-2 falls below the value expected for a square-law relationship, which is given by the straight line. This indicates the onset of saturation effects. However, complete saturation has not occurred, nor has the damage threshold of the crystal been reached, so we can reasonably anticipate further increases in average power.

2. Freon 12 Absorber

The use of SF_6 as the saturable absorber limits passive Q-switching to portions of the P branch of the 10.6-μm band. It is desirable to obtain stable Q-switched pulses on CO_2 laser lines which, when doubled, are coincident with CO absorption lines. The appropriate CO_2 laser lines are P(24), R(8), R(18), and R(30) of the 9.4-μm band. Freon 12 (CF_2Cl_2) has been reported to act as a saturable absorber for passive Q-switching of the three R-branch lines.[7] We investigated using Freon 12 with our laser, and obtained Q-switched pulses of the R(18) and R(30) lines. However, the gas pressure range over which Q-switching could occur was very limited. In addition, the power output had to be low (~5 W), the pulses were generally unstable, with the PRR limited to values between 110 and 150 kHz and pulse widths near 1.5 μsec. These results indicate that Freon 12 is unsuitable in a passively Q-switched CO_2 laser for obtaining a stable output which when doubled would be in coincidence with CO absorption lines.

Freon 12 can also be used as a saturable absorber in the P branch of the 10.6-μm band.[8] In this spectral range, we were able to obtain high-energy and stable Q-switched pulses. However, the PRR was limited to high values (~100 kHz), with pulse widths between 700 nsec and 1 μsec. This makes Freon 12 less effective than SF_6 for obtaining efficient second-harmonic generation in the 10.6-μm band.

N. Menyuk
P. F. Moulton
G. W. Iseler

C. RESONANT INFRARED THIRD-HARMONIC GENERATION IN CRYOGENIC LIQUIDS

Resonance enhancement of the nonlinear susceptibilities of gaseous media can lead to efficient frequency conversion.[9] In simple molecular liquids, e.g., N_2 and O_2, two-photon resonant processes (such as vibrational Raman scattering) can have extremely narrow linewidths[10] – one to two orders of magnitude narrower than typical linewidths of infrared (single-photon) absorption bands. These narrow linewidths also describe the resonance properties of third-harmonic generation (THG) for the case of a two-photon resonance between the pump-laser frequency and the molecular vibrational frequency. We report the first investigation of this two-photon resonant THG in liquid media, specifically the tripling of CO_2 laser radiation in liquid CO diluted with N_2, O_2, and Ar. The results indicate that a very narrow two-photon linewidth also occurs for the heteronuclear diatomic CO. Using a tight focusing geometry to compensate for the negative dispersion of the liquid CO medium between 9.3 and 3.1 μm, we obtained a power-conversion efficiency of 0.3 percent for the CO_2 R(6) line at 1069.01 cm^{-1}. The effects of various solvents on the CO two-photon resonance were observed. Phasematching was demonstrated by adding a positively dispersive molecule (SF_6) to the liquid mixture.

Previously, Bey et al.[11] reported phasematched THG in a room-temperature organic liquid using a 1.06-μm pump laser. However, the efficiency was low because the third-order susceptibility $\chi^{(3)}$ was nonresonant. The highest reported efficiency for THG of CO_2 laser radiation is 10^{-6} for the chalcopyrite $CdGeAs_2$ (Ref. 12). Recently, THG in CO gas at pressures up to a few atmospheres has been investigated.[13,14] In this case, $\chi^{(3)}$ is resonantly enhanced for the CO_2 pump lines R(8) and R(10) at 9.3 μm, which are in two-photon resonance with the vibrational-rotational lines of the CO Q-branch transition. Above a pressure of a few atmospheres, $\chi^{(3)}$ begins to saturate due to pressure broadening of the resonant transitions. At still higher pressures and at liquid densities, however, the discrete vibrational-rotational lines overlap, and the envelope of the Q-branch collapses into a narrow line due to motional narrowing effects,[15] which substantially enhances the peak value of $\chi^{(3)}$. Coupled with this, the laser-induced breakdown threshold reaches a minimum near 20 atm and then increases again at higher pressures.[16] Consequently, liquid CO, at a density corresponding to a pressure of 700 atm at 23°C, is expected to be an efficient system for THG.

A grating-controlled, TEM_{00} mode, spontaneously mode-locked, CO_2 TEA laser with a pulse width of 170 nsec (FWHM) for the R(6) line at 9.35 μm was used. The laser output was kept constant, and the energy incident on the Dewar containing the cryogenic liquid was controlled using CaF_2 attenuators and measured with a Gen-Tec ED-200 Joule meter. The external windows were BaF_2; both BaF_2 and ZnSe cold windows were used. The liquid path length ℓ was 5.8 cm. The laser beam was focused into the center of the Dewar with a 9.5-cm, f.l. ZnSe lens that gave a spot size of about 99 μm (confocal parameter $b \sim 0.81$ cm). The CO_2 radiation was blocked from the detector (InSb or Ge:Au) with 5-mm-LiF and 6-mm-quartz filters. For accurate measurements of conversion efficiencies, a Laser Precision RkP-335 energy meter, calibrated against the Gen-Tec Joule meter, was used.

Figure II-3 shows the third-harmonic signal generated in the tight focusing limit in CO diluted with different solvents using the CO_2 R(6) line at 9.35 μm as the pump. The CO concentration was monitored by measuring the peak absorbance of the second vibrational overtone transition near 6339 cm^{-1}. The relative CO peak absorbance is not exactly proportional to the

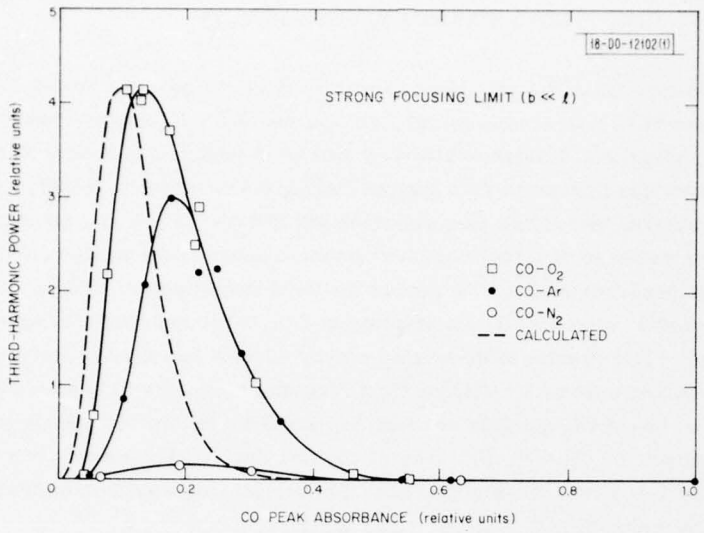

Fig. II-3. Concentration dependence of THG in CO diluted in different solvents at constant laser power (T = 77 K, ℓ = 5.8 cm, b = 0.81 cm). Maximum of calculated curve has been arbitrarily set equal to maximum of CO-O_2 experimental curve.

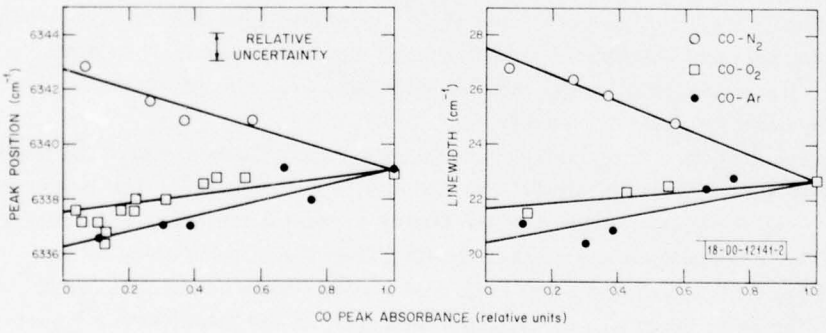

Fig. II-4. Linewidth (FWHM) and peak position of CO second vibrational overtone vs relative CO peak absorbance at second overtone transition measured for three solvents.

CO concentration since the linewidth of the second overtone transition is weakly solvent-dependent, as shown in Fig. II-4. (The linewidths in the figure are corrected for the 5.5-cm^{-1} spectrophotometer resolution by squaring the measured linewidth and the resolution, and taking the square root of the difference.)

The most efficient system for THG is the CO-O_2 solution. Furthermore, its observed laser-induced breakdown threshold is also at least a factor of two higher than that of the CO-Ar mixture. For the CO-O_2 system, at a relative CO peak absorbance of 0.125 (0.1 molar CO concentration), we measured a maximum third-harmonic power-conversion efficiency of 0.3 percent with 60 mJ focused into the liquid. The third-harmonic signal increased as the input power cubed up to the laser-induced breakdown threshold of the liquid at 390 J/cm^2 (area = $\pi w_o^2/2$). There was no evidence of saturation. At present, we do not know if this breakdown threshold represents an intrinsic value for the CO-O_2 mixture or if it can be increased by further purification.

We also examined briefly THG using the CO_2 R(4) and R(8) lines at 1067.54 and 1070.46 cm^{-1}, respectively. We find that for pure CO liquid the R(4) and R(8) lines produce a third-harmonic signal less than 1 percent of the signal generated by the R(6) line. This result implies bounds of 0.6 cm^{-1} for the linewidth, $\Delta\omega/2\pi c$, and 2138.0 ± 0.3 cm^{-1} for the center frequency, $\omega_o/2\pi c$, of the two-photon resonance of $\chi^{(3)}$. For the CO-N_2 mixture, the resonance is broader and the ratios between the third-harmonic signals produced by the R(6) compared with the R(4) and R(8) lines are about 10:1 at a CO relative absorbance of 0.19. In contrast, the ratios for the CO-O_2 and CO-Ar mixtures are larger than 100:1 at similar CO concentrations.

The THG power-conversion efficiency, given by Eq. (4) of Ref. 13, is proportional to $|\chi^{(3)}|^2$ and to $|\mathcal{F}|^2$, where $\mathcal{F}$ is the phase-mismatch integral; $\mathcal{F}$ reduces to $|\mathcal{F}|^2 = (\pi\Delta kb)^2 \exp[\Delta kb]$ for $\Delta k < 0$, and $|\mathcal{F}|^2 = 0$ for $\Delta k \geq 0$ in the tight focusing limit ($b \ll \ell$), where $\Delta k = k_3 - 3k_1$ is the wavevector mismatch. The dominant term in $\chi^{(3)}$ for CO in the case of a vibrational two-photon resonance is given by[13,14]

$$\chi^{(3)} = \frac{8\pi^2}{\mu_o^2 \hbar}\left(\frac{n^2+2}{3}\right)^4 \frac{d\sigma^r/d\Omega}{\omega_r \omega_s^3} \frac{N}{\omega_o - 2\omega_1 - i\Delta\omega/2} \qquad \text{(II-1)}$$

where $[(n^2+2)/3]^4$ is the local field correction,[17] and N is the CO density. The Raman pump and Stokes frequencies ω_r and ω_s are those used in measuring $d\sigma^r/d\Omega$, which is the narrow linewidth component of the Raman scattering cross section associated with the spherically symmetric part α' of the Raman polarizability tensor.[15,18] In addition, there is a weaker, broad-linewidth, scattering component associated with the traceless anisotropic component γ' of the polarizability tensor. We determine $d\sigma^r/d\Omega \approx 4.3 \times 10^{-31}$ $cm^2 sr^{-1}$ (λ_r = 514.5 nm) from the measured total Q-branch Raman scattering cross section,[19] which includes a negligibly small contribution from this broader scattering component.

The dashed curve in Fig. II-3 gives the calculated CO concentration dependence of the third-harmonic power neglecting any effects of the solvent on the $\chi^{(3)}$ resonance and any solvent dispersion. With these assumptions, both $\chi^{(3)}$ and Δk† vary linearly with N, and the optimum third-harmonic efficiency is obtained by maximizing $|\chi^{(3)}|^2|\mathcal{F}|^2$, which occurs for $\Delta k = -4/b$.

† $\Delta k = 6\pi(n_3 - n_1)/\lambda_1$ where $n_3 - n_1 = -16[(n^2+2)/3]^2 N|\mu_{01}|^2/(45n^3\epsilon_o\hbar\omega_1)$, cf. Refs. 5 and 9.

In pure CO liquid, the coherence length $|\pi/\Delta k| = 0.058$ cm is too short to allow optimizing $|\mathcal{F}|^2$ by varying b with practical infrared optics.

The differences between the experimental curves arise because of the solvent dependences of the two-photon resonance frequency and linewidth. Figure II-4 shows the dependence, measured by linear absorption, of the peak position of the second vibrational overtone in CO on the concentration of the three solvents used. Note that as the shift between the liquid-solution peak position and the gas-phase band center (6350 cm^{-1}) increases, the observed linewidth decreases. By taking advantage of the solvent shift, it is possible to fine-tune the vibrational transition for optimum THG. In pure CO liquid, the position of the two-photon resonance can be estimated by extrapolating the measured Raman shifts in high-pressure CO gas.[15] This gives $\omega_o/2\pi c = (2138.1 \pm 0.2)$ cm^{-1}, close to the doubled CO_2 R(6) frequency of 2138.03 cm^{-1}. We estimate ω_o for diluted CO mixtures by taking one-third of the second overtone absorption solvent shifts. For the optimum CO-O_2 mixture (0.1 molar CO concentration), we estimate a resonance mismatch of 0.4 cm^{-1}.

The fundamental vibrational-rotational single-photon absorption linewidths of liquid CO mixtures[20] (approximately equal to the second overtone absorption linewidths of Fig. II-4) are primarily determined by molecular reorientational motions. In contrast, the two-photon resonance linewidth $\Delta\omega$ associated with α' is much narrower, since it does not depend upon reorientational effects except through the vibrational-rotational interaction which determines the splittings of the Q-branch components.[15] There are two contributions to $\Delta\omega$ determined by (1) the dephasing of the vibrational transition, and (2) the motionally narrowed width of the Q-branch. This latter contribution should be about the same in CO as in N_2, since the molecular constants are similar; it is of the order of 0.07 cm^{-1} (Ref. 10), independent of solvent effects. The vibrational dephasing time, however, is probably shorter in CO than in N_2, since CO has a dipole moment. An upper limit for the dephasing time can be roughly estimated from the vibrational exchange time scaled from gas-phase data;[21] this gives 10 psec ($\Delta\omega/2\pi c \sim 1$ cm^{-1}) for pure CO liquid. By diluting CO in a solvent, we expect this linewidth contribution to decrease linearly with CO concentration. For the optimum CO-O_2 mixture, we estimate a total linewidth of 0.2 cm^{-1}.

When we insert the above values for $d\sigma^r/d\Omega$, $\Delta\omega$, and $\omega_o - 2\omega_1$ into Eq. (II-1) and use $n = 1.23$ estimated from low-pressure CO and O_2 gas data including local field corrections, we obtain $|\chi^{(3)}| = 8.4 \times 10^{-33}$ Asm/V^3. Then, for an incident energy of 60 mJ in a 170-nsec pulse we calculate a power-conversion efficiency of 5×10^{-5}, substantially lower than the measured value. This discrepancy is probably due to both overly large estimates for $\omega_o - 2\omega_1$ and $\Delta\omega$, and to the effects of the spontaneous modelocking of the CO_2 laser which enhances the measured conversion efficiency. Clearly, direct measurements of ω_o and $\Delta\omega$ are necessary for a better understanding of the THG process.

The dispersive characteristics of the liquid medium can be varied by adding additional constituents, as was done in the gas-phase experiments.[14] Phasematching ($\Delta k = 0$) has been achieved by adding the positively dispersive molecule SF_6 to a CO-O_2 solution. The measured CO-SF_6 ratio at phasematching was 216:1, in good agreement with our earlier results[14] in low-pressure CO gas (208:1). Details of this experiment will be reported elsewhere.[22] This phasematching technique is important for scaling up the THG system to higher output energies and efficiencies.

In conclusion, we have demonstrated a third-harmonic power-conversion efficiency of 0.3 percent for 9.35-μm radiation in a CO-O_2 solution using tight focusing to compensate for the negative dispersion of the solution, and we have shown that phasematching is possible by adding SF_6. The laser-induced breakdown threshold of the liquid of at least 400 J/cm^2 is much higher than the breakdown thresholds in solids, which are typically less than 10 J/cm^2 at 10 μm. For a somewhat longer cell than used in the present experiment and employing phasematching techniques, we estimate that a THG efficiency of 10 percent is obtainable. This tripling technique should also be applicable to other cryogenic liquids such as the various isotopic forms of CH_4, N_2, NO, and CO.

The liquid CO system is also useful for more general four-wave mixing processes ($2\omega_1 \pm \omega_2$). For example, with two CO_2 lasers it should be possible to produce outputs in the 8- to 9-μm region at efficiencies similar to the THG efficiency.

H. Kildal
S. R. J. Brueck

D. VIBRATIONAL TWO-PHOTON RESONANCE LINEWIDTHS IN CONDENSED MEDIA

As discussed in the preceding section, it is the very narrow two-photon resonance of the third-order susceptibility tensor $\chi^{(3)}$ for liquid CO and CO-O_2 mixtures, coupled with the high laser breakdown threshold, which leads to the efficient tripling of CO_2 laser radiation. The widths of these two-photon resonances (0.1 cm^{-1}, Ref. 10), which arise from the isotropic component of the Raman polarizability tensor, in simple cryogenic liquids such as N_2, CO, O_2, etc. are, on the one hand, very much narrower than the widths of the single-photon (infrared absorption) and anisotropic two-photon resonances (~30 cm^{-1}, Refs. 20 and 23) and are, on the other hand, very much broader than the widths determined by vibrational energy relaxation processes (<10^{-12} cm^{-1}, Ref. 24).

In this section we discuss one physical mechanism, the vibration-rotation interaction, which contributes significantly to the isotropic two-photon resonance linewidth, and obtain a simple analytic result for estimating its magnitude. A number of recent papers devoted to an evaluation of this two-photon resonance linewidth have not included this linewidth contribution.[25-27] The isotropic two-photon resonance is narrower than the single-photon and anisotropic two-photon resonances because it is, to a first approximation, independent of the molecular rotational degrees of freedom and is thus affected primarily by vibrational dephasing processes. However, due to the vibration-rotation interaction, the rotational degrees of freedom are weakly coupled into the isotropic two-photon resonance. At low pressures, this results in a splitting of the two-photon resonance, which describes the polarized Raman scattering Q-branch, into a series of discrete lines whose frequencies are given by $\omega(J) = \omega_o - 2\pi c \alpha_e J(J+1)$, where ω_o is the vibrational frequency, α_e is the vibration-rotation coupling constant, c is the speed of light, and J is the angular momentum.[28] As the pressure is increased, these lines broaden and begin to overlap, and the total resonance width decreases due to motional narrowing effects.[15] It is this motional narrowing of the two-photon resonance which leads to the large enhancement of $\chi^{(3)}$ at high pressures and in the liquid state.

We describe this motionally narrowed regime by an extension of the J-diffusion description of rotational dephasing first discussed by Gordon.[29] Rotation is treated classically and molecules are assumed to rotate freely between collisions that randomize the rotational angular

momentum. A density matrix formulation of this model is given here because of its compactness. A similar model has recently been used to describe motional narrowing of the spin-flip Raman resonance in semiconductors, and a derivation of the lineshape function more closely paralleling Gordon's correlation function calculation is given in Ref. 30. The time evolution of the density matrix is given by the expression

$$i\hbar \frac{\partial \rho}{\partial t} = [\mathcal{H}_o - \mu \cdot \mathcal{E}, \rho] + i\hbar \frac{\partial \rho}{\partial t}\Big|_{coll} \tag{II-2}$$

where the collision term is given by

$$\frac{\partial \rho}{\partial t}\Big|_{coll} = -\frac{1}{T_2}\rho - \frac{1}{\tau_J}[\rho - f(\omega_r)\langle\rho\rangle] \tag{II-3}$$

and the angular brackets denote an integral over the rotational states of the molecule. Further, $f(\omega_r) = 1/(\omega^*)^2 \exp[-\omega_r^2/2\omega^{*2}]$ is the Boltzmann-weighted density of states for a linear molecule, where $\omega^* = (4\pi cKT B_e/\hbar)^{1/2}$, with B_e the rotational constant. In Eq. (II-3), T_2 is the vibrational dephasing time and τ_J is the duration of the free rotational motion between angular momentum randomizing collisions. Note that the second term on the right side in Eq. (II-3) has the property that it conserves the total number of vibrational excitations, e.g.,

$$\int \left(\frac{\partial \rho}{\partial t}\Big|_{coll}\right) d\omega_r = -\frac{1}{T_2}\int \rho d\omega_r$$

independent of τ_J. These equations can be readily solved for the lineshape dependence of $\chi^{(3)}$ near a two-photon vibrational resonance, viz:

$$I(2\omega_1) \propto N \frac{\frac{e^{+\xi}}{2\gamma\omega^{*2}} E_1(\xi)}{1 + \frac{i}{\tau_p}\frac{e^{+\xi}}{2\gamma\omega^{*2}} E_1(\xi)} \tag{II-4}$$

where $E_1(x)$ is the exponential integral, $\gamma = \alpha_e/8\pi cB_e^2$, $\xi = (2\omega_1 - \omega_o - i/\tau)/2\omega^{*2}\gamma$, $1/\tau = 1/T_2 + 1/\tau_J$, and N is the molecular density.

Figure II-5 shows the maximum value of $\chi^{(3)}$ as a function of molecular density calculated for the molecular parameters of N_2. At low pressures, a simple pressure-broadening model (pressure-broadening coefficient 0.05 cm^{-1}/amagat) was used. At pressures below 0.1 amagat, the individual rotational components of the Q-branch are Doppler-broadened, and the magnitude of $\chi^{(3)}$ increases linearly with density. Between 0.1 and 1 amagat is the pressure-broadened regime in which the rotational components are still isolated, but the linewidth is increasing linearly with density and $\chi^{(3)}$ remains approximately constant. Between 1 and 10 amagats, the individual rotational lines begin to overlap and merge into a single line. The effects of motional narrowing become important above this density, and Eq. (II-4) has been used to evaluate $\chi^{(3)}$. The dotted curve gives the $\chi^{(3)}$ expected if motional narrowing is neglected and the simple pressure-broadening theory is extended beyond its proper range of applicability. The motional-narrowing effects clearly lead to a large enhancement of the peak value of $\chi^{(3)}$. The data point at 600 amagats is the experimental result of Clements and Stoicheff.[10] The value of τ_J at this density, using the same pressure-broadening coefficient as was used at low pressures, is 0.35 psec, in good agreement with the τ_J evaluated by van Konynenburg and Steele[23] in fitting

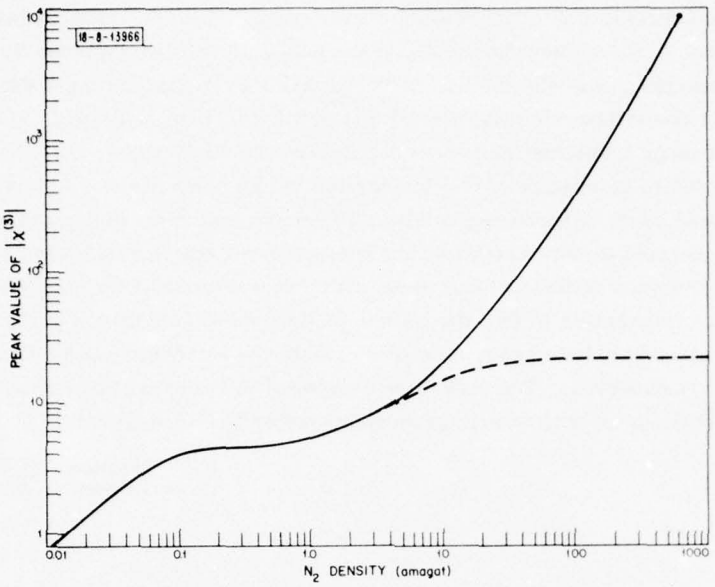

Fig. II-5. Calculated peak value of two-photon resonant third-order susceptibility for N_2 as a function of density, illustrating Doppler-broadened, pressure-broadened, and motionally narrowed regimes. (T = 77 K, pressure-broadening coefficient 0.05 cm^{-1}/amagat.)

their results for the anisotropic Raman linewidth to the J-diffusion model. In the strongly motional-narrowed limit,

$$\tau_J \frac{\alpha_e}{B_e} \frac{kT}{\hbar} \ll 1$$

the calculated lineshape is Lorentzian of width (FWHM)

$$\Gamma = 2\tau_J \left(\frac{\alpha_e}{B_e} \frac{kT}{\hbar}\right)^2$$

and the peak value of $\chi^{(3)}$ scales as N^2.

In summary, we have developed a simple expression for evaluating the contribution to the linewidth of the isotropic two-photon resonance in diatomic molecules due to the motionally narrowed vibration-rotation interaction, and have demonstrated that this mechanism contributes significantly to the total linewidth. Vibrational dephasing contributions,[25-27] which we have not included, should also be significant, and a full theory of the linewidth must incorporate both effects. Further experimental work is also necessary for a full understanding of the linewidths, and hence of the optimum system for nonlinear optical processes.

S. R. J. Brueck

E. DOUBLE-RESONANCE SPECTROSCOPY OF SF_6

Tunable PbSnTe double-heterostructure diode lasers operating CW at temperatures of 77 K and above have been used with a single-frequency, electro-optically Q-switched CO_2 laser to perform double-resonance spectroscopy of SF_6 gas in the 10.6-μm region. The diode-laser

output is passed transversely through a region of gas excited by the focused, pulsed output of the CO_2 (pump) laser. The perturbation of the transmitted diode signal caused by pump-laser-induced transient changes in the distribution of rotational-vibrational states is detected. Wavelength regions in the immediate vicinity of the P(12) and P(16) through P(24) CO_2 lines have been examined, and large transient increases in the detected diode signal have been observed. Such increases are due to saturation of SF_6 absorption by the pump laser. In addition, diode lasers have been tuned to other wavelengths around 10.6 μm, and transient signals have been observed which are related to optical transitions from excited vibrational states and to transitions which share a common initial or final state with states connected by the pump laser. The latter transitions are interesting in that the effects of Rabi nutation between pump levels are evident. Theoretical work is being carried out to explain the lineshapes and spectroscopic features of the signals observed. The technique developed in the experiments may be useful in understanding observations of multiphoton photodissociation in this molecule.

P. F. Moulton J. N. Walpole
D. M. Larsen A. Mooradian

REFERENCES

1. S. R. Chinn, J. W. Pierce, and H. Heckscher, IEEE J. Quantum Electron. QE-11, 747 (1975), DDC AD-A017355/9.
2. S. Singh et al., J. Appl. Phys. 46, 1191 (1975).
3. G. Huber et al., J. Appl. Phys. 46, 3580 (1975).
4. G. Winzer et al., Appl. Phys. 11, 121 (1976).
5. Solid State Research Report, Lincoln Laboratory, M.I.T. (1975:4), p. 18, DDC AD-A025489/6.
6. N. Menyuk, G. W. Iseler, and A. Mooradian, Appl. Phys. Lett. 29, 422 (1976).
7. J. J. Wynne and F. Shimizu, IEEE J. Quantum Electron. QE-9, 676 (1972).
8. S. Marcus, Appl. Phys. Lett. 15, 217 (1969).
9. D. M. Bloom, J. T. Yardley, J. F. Young, and S. E. Harris, Appl. Phys. Lett. 24, 427 (1974).
10. W. R. L. Clements and B. P. Stoicheff, Appl. Phys. Lett. 12, 246 (1968).
11. P. P. Bey, J. F. Giuliani, and H. Rabin, Phys. Rev. Lett. 19, 819 (1967).
12. H. Kildal, R. F. Begley, M. M. Choy, and R. L. Byer, J. Opt. Soc. Am. 62, 1398 (1972).
13. H. Kildal and T. F. Deutsch, IEEE J. Quantum Electron. QE-12, 429 (1976), DDC AD-A030985.
14. H. Kildal (to be published).
15. A. D. May, J. C. Stryland, and G. Varghese, Can. J. Phys. 48, 2331 (1970).
16. N. G. Basov, E. M. Belenov, V. A. Danilycnev, O. M. Kerimov, and I. B. Kovsh, Zh. Eksp. Teor. Fiz. 63, 2010 (1972) [Sov. Phys. JETP 36, 1061 (1973)].
17. N. Bloembergen, Nonlinear Optics (Benjamin, New York, 1965), p. 68.
18. R. G. Gordon, Adv. Magn. Reson. 3, 1 (1968).

19. C. M. Penney, L. M. Goldman, and M. Lapp, Nature Phys. Sci. 235, 110 (1972).

20. G. E. Ewing, J. Chem. Phys. 37, 2250 (1962).

21. H. T. Powell, J. Chem. Phys. 63, 2635 (1975).

22. S. R. J. Brueck and H. Kildal (to be published).

23. P. van Konynenburg and W. A. Steele, J. Chem. Phys. 62, 2301 (1975).

24. S. R. J. Brueck and R. M. Osgood, Jr., Chem. Phys. Lett. 39, 568 (1976), DDC AD-A028459/6.

25. S. F. Fischer and A. Laubereau, Chem. Phys. Lett. 35, 6 (1975).

26. D. W. Oxtoby and S. A. Rice, Chem. Phys. Lett. 42, 1 (1976).

27. W. G. Rothschild, J. Chem. Phys. 65, 2958 (1976).

28. G. Herzberg, Molecular Spectra and Molecular Structure, I. Spectra of Diatomic Molecules, 2nd edition (Van Nostrand-Reinhold, New York, 1950).

29. R. G. Gordon, J. Chem. Phys. 44, 1830 (1966).

30. S. R. J. Brueck, A. Mooradian, and F. A. Blum, Phys. Rev. B 7, 5253 (1973), DDC AD-772151/7.

III. MATERIALS RESEARCH

A. THICKNESS OF InP LAYERS GROWN BY LIQUID-PHASE EPITAXY

In the fabrication of GaInAsP/InP double-heterostructure diode lasers,[1] InP barrier layers are grown by liquid-phase epitaxy (LPE). Accurate control of layer thickness is necessary for satisfactory device performance. In this study, the thickness of LPE InP layers was measured as a function of the growth conditions, and the experimental results were used to test the applicability of a simplified model for diffusion-limited growth from a dilute, semi-infinite, supercooled solution. By using this model, the following expression[2] was derived for the thickness d of an LPE layer:

$$d = (1/C_s m)\,(D/\pi)^{1/2}\,(2\Delta t^{1/2} + \tfrac{4}{3}Rt^{3/2}) \qquad \text{(III-1)}$$

where C_s is the concentration in the solid compound of the element present in lower concentration in the solution (e.g., P in InP), m is the slope of the liquidus curve, D is the diffusion coefficient of the lower-concentration element in the solution, Δ is the amount of supercooling (i.e., the difference between the equilibrium liquidus temperature T_ℓ and the initial growth temperature), t is the growth time, and R is the rate of cooling. In this expression, C_s and m are expressed in atoms per unit volume. It is more convenient to express them in terms of atom fractions, with $C_s = 1/2$ and m given in the usual phase diagram unit, deg (atom fraction)$^{-1}$. Equation (III-1) can then be rewritten as

$$d = (2F/m)\,(D/\pi)^{1/2}\,(2\Delta t^{1/2} + \tfrac{4}{3}Rt^{3/2}) \qquad \text{(III-2)}$$

where F is 1.94 for dilute In-P solutions.

In order to make a reliable experimental test of Eq. (III-2), the values of Δ must be accurately known. This, in turn, requires accurate values for T_ℓ as a function of solution composition. Since the published data[3-6] for the In-rich liquidus of the In-P system are somewhat inconsistent, the first step in the present investigation was to redetermine this liquidus curve over the temperature range of interest. Next, a series of LPE growth experiments was performed at different temperatures to determine d as a function of t and Δ (using the measured values of T_ℓ to obtain Δ from the initial growth temperatures). We found that d had the functional dependence on t and Δ predicted by Eq. (III-2). It was concluded that the LPE growth of InP is diffusion-limited under the experimental conditions used, and values of D were then found as a function of temperature by adjusting D to give the best fit to the thickness data.

Liquidus temperatures were measured by using an instrumental version[7] of the visual-observation technique. An In-P solution of known composition is heated and cooled in a graphite boat inside a transparent furnace under a slow flow of H_2. The temperature at which solid InP particles completely disappear from the surface of the solution during heating is determined to ±0.5°C by using a microscope-photodetector-recorder combination to monitor the amount of light scattered from the solution surface. For the In-P system, obtaining accurate T_ℓ values is made more difficult because the vapor pressure of P over even In-rich solutions is sufficient to cause significant loss of P by vaporization during the time required for a measurement. To correct for this effect, we determined the rate at which the apparent liquidus temperature (T'_ℓ) decreases when the In-P solution is held at a fixed temperature in our apparatus. Corrected values of T_ℓ were then obtained by adding, to each measured T'_ℓ value, the product of the rate of decrease and the number of hours at temperature.

PRECEDING PAGE BLANK-NOT FILMED

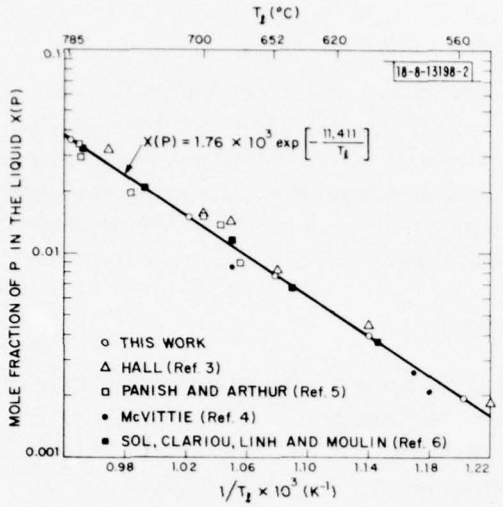

Fig. III-1. In-P solubility curve.

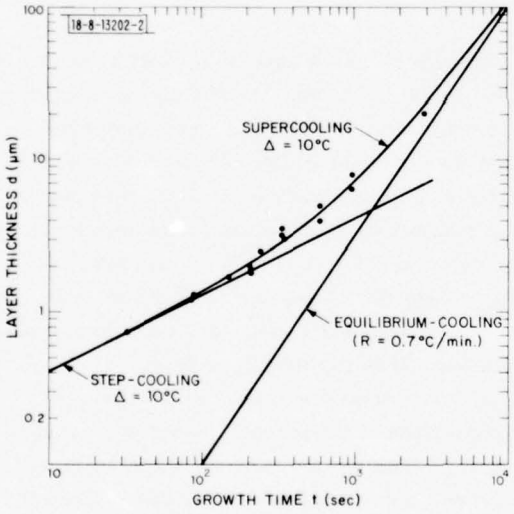

Fig. III-2. Thickness d of InP epitaxial layers vs growth time t for Δ = 10°C, R = 0.7°C/min. Mid-temperature of growth is 630°C. Solid lines were calculated by using P diffusivity of 1.2×10^{-5} cm^2/sec.

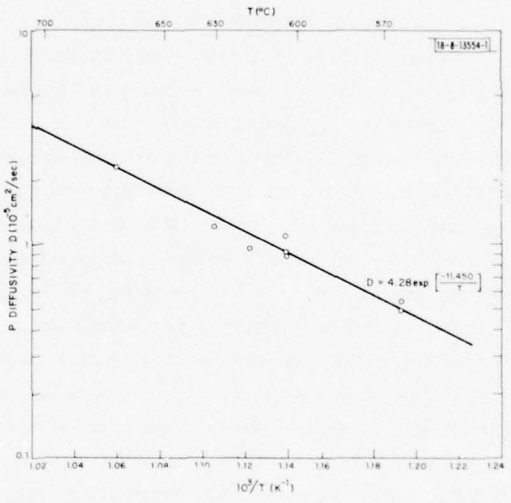

Fig. III-3. Diffusion coefficient D for P in In solutions as a function of reciprocal absolute temperature.

The liquidus data obtained for the In-rich side of the In-P system are shown by the solubility plot in Fig. III-1, where the mole fraction of P dissolved in the liquid phase X(P) is plotted on a logarithmic scale as a function of the reciprocal absolute liquidus temperature. Over the temperature range investigated, from 560° to 785°C, the data are well represented by a straight line corresponding to the equation

$$X(P) = 1.76 \times 10^{3} \exp[-11{,}411/T_{\ell}] \quad . \tag{III-3}$$

These results are in very good agreement with earlier data[6] obtained by using a sliding boat apparatus to determine the weight loss of InP seeds dissolved in molten In. The slope of the In-rich liquidus curve, $m \equiv dT_{\ell}/dX(P)$, corresponding to Eq. (III-3), is given by $m = 11{,}411[X(P)/T_{\ell}^{2}]$.

After the liquidus data had been obtained, the growth rate of LPE layers of InP was measured in a series of experiments using a horizontal graphite slider boat in flowing hydrogen. The experimental techniques were similar to those we used previously for the LPE growth of GaAs (Ref. 2). The solution well was a cylindrical hole 1.07 cm in diameter. The growth charge consisted of 3 g of In and the desired amount of P supplied in the form of InP, giving a solution about 0.7 cm thick. The charge was doped with a small quantity of Zn in order to make the LPE layer p-type so that it could be delineated more clearly from the substrate, which was a (111)B-oriented, n-type wafer 0.84×0.84 cm^2 in area. Immediately after each growth run, the solution was examined to see whether there had been any precipitation of InP on the upper surface. Thickness data were taken only if no precipitation had occurred. After the wafer was removed from the growth furnace, it was cleaved and etched with a solution of $K_3Fe(CN)_6$ and KOH. The layer thickness was then measured with an optical microscope.

Figure III-2 is a log-log plot showing the measured thickness d as a function of growth time t for LPE layers of InP grown at a cooling rate R = 0.7°C/min. from solutions that were supercooled by Δ = 10°C at the time of their initial contact with the substrate. The values of T_{ℓ} used in determining Δ were corrected for the loss of P from the growth solutions by vaporization; the uncertainty in determining T_{ℓ} (and therefore Δ) was less than 1°C in each case. In these experiments, the midpoint of the growth temperature interval was T_m = 630°C, at which the value of 1/m is 8×10^{-5} K^{-1}. The specified values of R, Δ, and 1/m were substituted into Eq. (III-2), and the value of the diffusion constant D was then adjusted to give the best fit between this equation and the experimental data. The value adopted was $D = 1.2 \times 10^{-5}$ cm^2/sec, which gave the upper curve shown in Fig. III-2. For short growth times, this curve for supercooling growth closely approximates the straight line in Fig. III-2 that was calculated for step-cooling growth (with the same values of D and Δ), in which the temperature remains unchanged after contact has been made between growth solution and substrate. At long growth times, the curve for supercooling growth approaches the straight line in Fig. III-2 that was calculated for equilibrium-cooling growth (with the same values of D and R), in which the growth solution and substrate are placed in contact at T_{ℓ}.

In several additional series of supercooling-growth experiments, measurements of d vs t were made for values of T_m between 550° and 680°C. The results for each temperature are in quantitative agreement with Eq. (III-2), showing that LPE growth was diffusion-limited under the experimental conditions employed. For each value of T_m, the value of D was adjusted to give the best fit between Eq. (III-2) and the experimental data. The values of D found in this way are plotted on a logarithmic scale against reciprocal absolute temperature in Fig. III-3. The data

are well represented by the straight line shown, which corresponds to the equation

$$D\ (cm^2/sec) = 4.28 \exp[-11{,}450/T] \quad . \tag{III-4}$$

This expression has the usual form for thermally activated diffusion, $D = D_o \exp[-E_a/kT]$, with $D_o = 4.28\ cm^2/sec$ and $E_a = 0.99$ eV.

J. J. Hsieh

B. CONDITIONS FOR LATTICE MATCHING IN THE LPE GROWTH OF GaInAsP LAYERS ON InP SUBSTRATES

In experiments on the liquid-phase-epitaxial (LPE) growth of GaInP layers on GaAs substrates, Stringfellow[8] observed that over a certain range of liquid compositions the LPE layers all had the composition that was lattice-matched to GaAs, rather than varying in composition in a manner consistent with the bulk equilibrium phase diagram. He explained this observation in terms of the strain energy and dislocation energy resulting when epilayers are not lattice-matched to their substrates. If these energies are large enough, such layers will be higher in free energy than lattice-matched layers, and therefore epilayer compositions that result in lattice matching will be favored.

In developing a procedure for fabrication of double-heterostructure GaInAsP/InP diode lasers, we made a detailed study of the LPE growth of GaInAsP layers on InP substrates. This study revealed no evidence that lattice-matching epilayer compositions are favored in this system. Instead, the composition is found to be a sensitive function of the growth parameters. Close control of these parameters is therefore necessary to obtain lattice-matched epilayers, which are required for efficient operation of the GaInAsP/InP lasers.

The GaInAsP epilayers were grown on single-crystal InP substrates by a supercooling technique described previously,[2] which uses a high-purity graphite slider boat. The quaternary growth solutions consisted of accurately weighed amounts of In, InAs, InP, and GaAs. Usually, an InP buffer layer was grown immediately before the quaternary layer in order to minimize imperfections due to thermal etching of the substrate during heating. The GaInAsP layers were typically 2 to 3 μm thick. The epilayer composition at the substrate interface was estimated by extrapolating measurements made with an electron microprobe on thicker epilayers. The lattice mismatch $\Delta a/a$ was measured by x-ray diffraction. The wavelength λ_T of the epilayer transmission cutoff was found by extrapolating to zero transmission the linear portion of the transmission curve for the epilayer-substrate composite measured with a grating spectrophotometer. The epilayers were generally not intentionally doped, and their residual electron concentration was in the mid 10^{16}-cm^{-3} range. In cases where diode lasers[1] were to be fabricated, the GaInAsP active layer was about 0.5 μm thick and was made n-type by doping with Sn at the level of $3 \times 10^{17}\ cm^{-3}$.

In Fig. III-4, the epilayer Ga content (Ga^S), P content (P^S), and lattice mismatch ($\Delta a/a$) are plotted against the P content (P^ℓ) of the growth solution for experiments in which the Ga and As contents of the solution were kept constant at 0.47 and 0.25 a/o, respectively, the supercooling Δ was zero, the cooling rate R was 0.7°C/min., and the substrate orientation was (111)B. As P^ℓ was increased from 0.20 to 0.31 a/o, P^S increased linearly from 51 to 58 percent, while Ga^S remained almost constant. (The numerical values given for Ga^S and P^S are equal to twice the atomic percentages for these elements in the epilayers; these values give the percentages of Group III and Group V sublattice sites occupied by Ga and P, respectively.) Thus, the principal

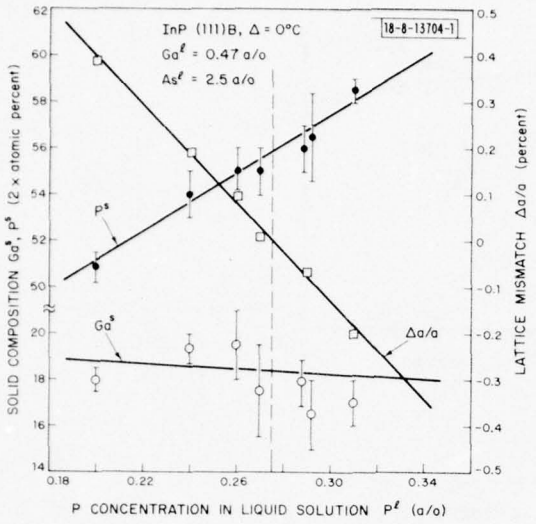

Fig. III-4. Epilayer compositions (Ga^S and P^S) and lattice mismatch ($\Delta a/a$) as functions of growth solution composition P^ℓ for LPE growth of GaInAsP on InP substrates. Liquid compositions Ga^ℓ and As^ℓ were kept constant.

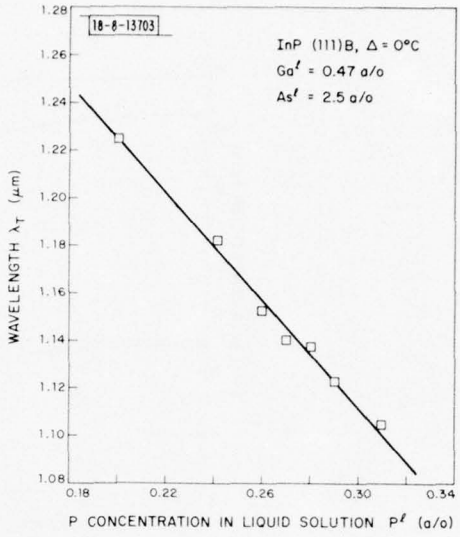

Fig. III-5. Transmission cutoff λ_T of GaInAsP epilayers as a function of P^ℓ for growth conditions of Fig. III-4.

effect of changing the P content of the solution is a linear variation in the composition of the Group V sublattice. This linear variation is confirmed by the data shown in Fig. III-4 for $\Delta a/a$, which varies linearly from +0.40 to −0.20 percent over the P^ℓ range investigated. (In calculating the lattice mismatch, Δa is equal to the lattice constant of the epilayer minus the lattice constant of InP, a = 5.8685 Å.) Exact lattice matching ($\Delta a/a = 0$) would occur for $P^\ell = 0.27$ a/o, the value indicated by the dashed vertical line in Fig. III-4. The linear variation in epilayer composition is further confirmed by the transmission cutoff data shown in Fig. III-5, where it is seen that λ_T also varies linearly with P^ℓ.

The linear variation in solid composition over a range that includes the lattice-matched composition $Ga_{0.185}In_{0.815}As_{0.44}P_{0.56}$ indicates that the composition of GaInAsP epilayers grown on InP substrates is not significantly affected by the degree of lattice mismatch. This result is in sharp contrast with Stringfellow's observation that the composition of GaInP layers grown on GaAs substrates remains constant over an appreciable range of liquid compositions.[8] Furthermore, there is a striking difference in the effect of lattice mismatch on epilayer morphology in the two systems. Stringfellow found that catastrophic degradation of the surface morphology of GaInP layers occurred when Ga^S differed by more than about ±1 percent from the lattice-matched composition $Ga_{0.51}In_{0.49}P$. In contrast, very smooth surfaces are obtained for GaInAsP layers over the entire composition range of Fig. III-4.

In addition to studying the influence of growth solution composition on the GaInAsP epilayers, we have also investigated the effects of substrate orientation and of changes in the amount (Δ) by which the growth solution was supercooled at the time of initial contact with the substrate. Figure III-6 shows P^S and Ga^S as functions of Δ for epilayers grown on (111)B and (100) InP substrates from a solution with the composition $Ga_{0.0047}In_{0.9599}As_{0.0330}P_{0.0024}$. For $\Delta = 0$,

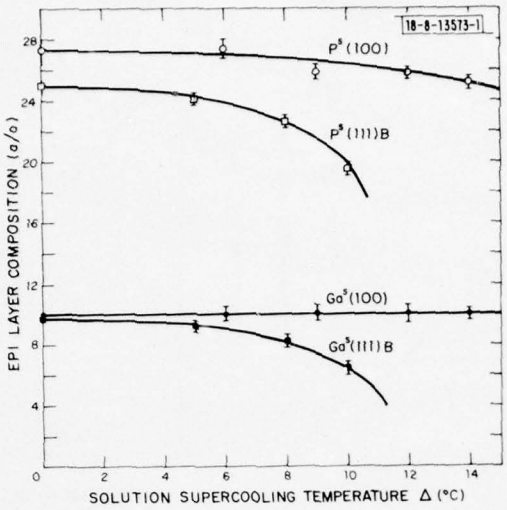

Fig. III-6. Variation of epilayer compositions Ga^S and P^S with degree of solution supercooling Δ. Composition of growth solution is $Ga_{0.0047}In_{0.9599}As_{0.0330}P_{0.0024}$ in all cases.

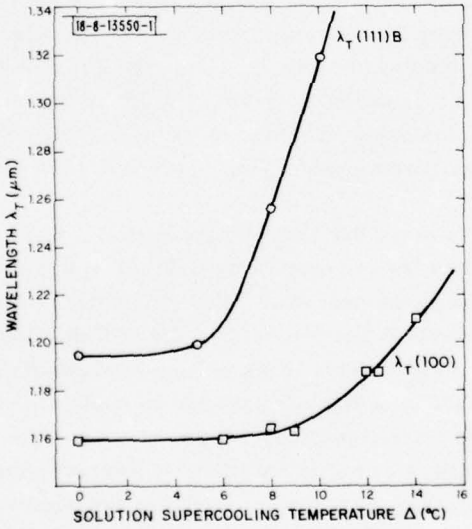

Fig. III-7. Transmission cutoff λ_T as a function of solution supercooling Δ for same liquid composition as in Fig. III-6.

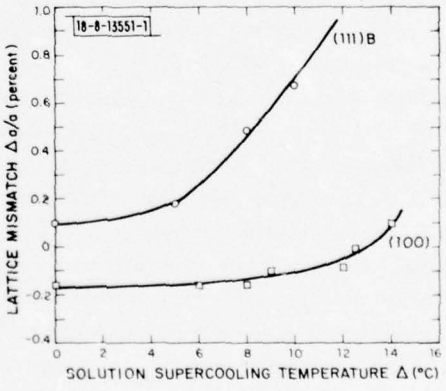

Fig. III-8. Variation of lattice mismatch $\Delta a/a$ with solution supercooling Δ for same liquid composition as in Fig. III-6.

Ga^S is essentially the same for the two orientations, while P^S is significantly lower for the (111)B layers. The composition of the (100) layers is relatively insensitive to changes in Δ, although there is an appreciable decrease in P^S at the highest values of Δ. The effect of supercooling is much stronger for the (111)B layers, with both Ga^S and P^S decreasing markedly as Δ increases.

The composition changes shown in Fig. III-6 are accompanied by changes in bandgap and in lattice constant. The bandgap changes lead to variation in the transmission cutoff λ_T, as shown in Fig. III-7. For $\Delta = 0$, λ_T is longer for (111)B than for (100) layers. As Δ increases, the wavelengths are initially almost constant, but eventually they begin to increase. This occurs sooner and much more rapidly for the (111)B layers, so that the wavelength differences between the two orientations increase markedly.

Figure III-8 shows the lattice mismatch as a function of Δ for GaInAsP layers grown on (111)B and (100) substrates from growth solutions with the same composition used for the layers of Figs. III-6 and III-7. At $\Delta = 0$, $\Delta a/a$ is positive for the (111)B layers and negative for the (100) layers. With increasing Δ, $\Delta a/a$ increases algebraically for both orientations, sooner and much more rapidly for the (111)B than for the (100) layers. Therefore, lattice matching can never be achieved for (111)B layers grown from a solution of this composition, but lattice-matched (100) layers are obtained for $\Delta = 12.5°C$.

Because the composition of GaInAsP epilayers is sensitive to substrate orientation, high-quality layers cannot be grown directly on InP substrates that are thermally etched by vaporization of P. Thermal etching produces roughened surfaces on which different crystallographic orientations are exposed. Growth of GaInAsP on such surfaces produces local variations in composition, and the resulting variations in lattice constant lead to the formation of polycrystalline mounds. Such imperfections are not formed during the growth of InP epilayers on thermally etched InP substrates, since InP is always essentially stoichiometric, so there is no variation in lattice constant. In fact, after sufficient growth, the surface of the InP layers becomes smooth. Therefore, high-quality GaInAsP can be obtained by growing an InP buffer layer on the InP substrate, and then immediately growing the GaInAsP before there is time for the buffer layer to become thermally etched.

Since the composition of GaInAsP layers grown on InP substrates is a sensitive function of the growth parameters, rather than being automatically adjusted to produce lattice matching, close control of these parameters is necessary in order to obtain reproducible, lattice-matched layers of the quality required for diode lasers. The degree to which this has been accomplished is indicated by results given in Tables III-1 and III-2. Table III-1 lists the peak emission wavelengths of a number of randomly selected stripe-geometry double-heterostructure GaInAsP/InP lasers made from a single wafer. The relative wavelength variation is ±0.22 percent, and the total variation (53 Å) is comparable to the wavelength spread of the modes for each diode, which ranges from 30 to 50 Å. Table III-2 lists the peak emission wavelengths for diodes made from layers prepared in five different runs under nominally the same growth conditions. In this case, the relative wavelength variation is ±0.65 percent, and the total variation (148 Å) is again comparable to the total mode spacing, which ranges from 100 to 150 Å.

J. J. Hsieh
M. C. Finn
J. A. Rossi

TABLE III-1

EMISSION WAVELENGTHS OF DOUBLE-HETEROSTRUCTURE DIODE LASERS FROM A WAFER WITH ACTIVE REGION COMPOSITION OF $Ga_{0.11}In_{0.89}As_{0.30}P_{0.70}$

Diode No.	λ_L (Å)	$\Delta\lambda_L$ (Å)
1	11,317	−11
2	11,349	21
3	11,339	11
4	11,339	11
5	11,296	−32
	Average 11,328	

TABLE III-2

EMISSION WAVELENGTHS OF DOUBLE-HETEROSTRUCTURE DIODE LASERS FROM DIFFERENT WAFERS WITH ACTIVE REGION COMPOSITION OF $Ga_{0.16}In_{0.84}As_{0.40}P_{0.60}$

Run No.	λ_L (Å)	$\Delta\lambda_L$ (Å)
302	11,439	−32
318	11,492	21
324	11,400	−71
326	11,548	77
327	11,476	5
	Average 11,471	

C. DOUBLE-HETEROSTRUCTURE GaInAs/InP DIODE LASERS

Quaternary GaInAsP alloys having the same lattice constant as InP can be prepared over a range of compositions that give room-temperature energy gaps corresponding to any wavelength between 0.92 and 1.7 μm. By using such lattice-matched alloys for the active region of double-heterostructure (DH) GaInAsP/InP diode lasers, we achieved room-temperature CW operation of lasers emitting at 1.1 μm (Ref. 1). In order to determine whether this type of operation can be obtained over the entire range of lattice-matched compositions, we have prepared DH diodes with an active-region composition of $Ga_{0.465}In_{0.535}As$, the P-free limit of the range. Preparation of these diodes required modification of the structure and growth procedure used for GaInAs/InP lasers. Room-temperature laser operation of the GaInAs/InP diodes has not been achieved, although pulsed operation has been obtained at liquid nitrogen temperature, where the emission wavelength is 1.58 μm. Similar results have recently been reported by Nagai and Noguchi.[9]

The GaInAs/InP diodes were fabricated from wafers prepared by using a supercooling technique described previously[2] to grow three successive LPE layers on (111)B-oriented, Sn-doped, n-type InP substrates. The layer structure is shown in Fig. III-9, which is an optical micrograph of a cleaved edge of one of the wafers. The three layers are: an Sn-doped, n-type $Ga_{0.465}In_{0.535}As$ active layer; a Zn-doped, p-type $Ga_{0.20}In_{0.80}As_{0.48}P_{0.52}$ barrier layer with the same lattice constant as InP; and a Zn-doped, p-type InP layer.

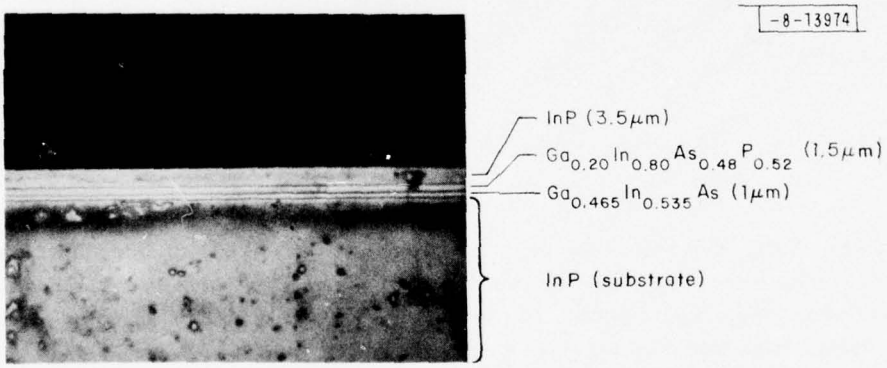

Fig. III-9. Cleaved edge of GaInAs/InP double heterostructure.

The GaInAs/InP structure differs from that of GaInAsP/InP DH diode lasers in having a lattice-matched GaInAsP alloy, rather than InP, grown on the active layer. This change was made in order to prevent melt-back of the GaInAs active layer, which was found to occur when this layer was placed in contact with the supercooled In-P solution used for growth of InP. The GaInAsP composition selected for the third layer has a sufficiently large energy gap (at 80 K, 1.12 eV compared with 0.81 eV for the active layer) and sufficiently small refractive index (estimated to be 6 percent lower than that of the active layer) to provide carrier and optical confinement if the layer thickness is greater than about 2 μm.

In addition to the change in the structure of the GaInAs/InP DH diodes, a modification of the growth procedure was also necessary. In preparing GaInAsP/InP diodes, all the LPE layers

are grown in a single run, without removing the growth boat and wafer from the furnace. When the same procedure was followed for the GaInAs/InP devices, laser operation could not be obtained even at 80 K. However, lasers could be prepared by using two growth runs – one for the active layer and the other for the last two – with the wafer being removed from the furnace and exposed to air between the two runs. It was also necessary to increase the cooling rate used during the second run to 7°C/min., compared with the rate of 0.5°C/min. used in the first run (as well as in the growth of GaInAsP/InP heterostructures). All three layers were grown within the cooling range of 570° to 540°C.

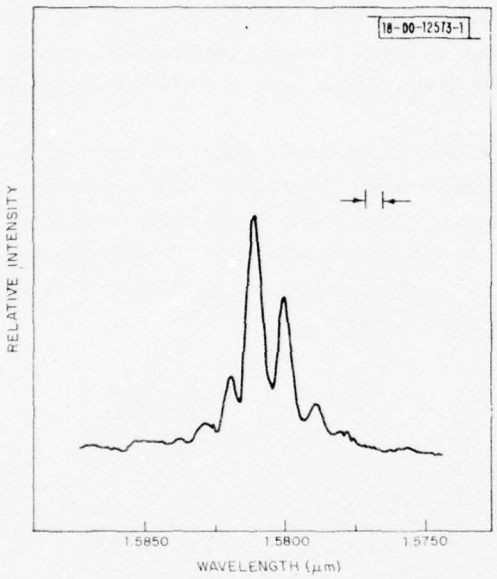

Fig. III-10. Emission spectrum of pulsed GaInAs/InP DH diode laser at 80 K for current density 30 percent above threshold.

The wafer of Fig. III-9 was prepared by the procedure described. A diode fabricated from this wafer gave the laser emission spectrum shown in Fig. III-10, which was obtained for pulsed operation at 80 K for a current density 30 percent above the threshold of 3 kA/cm^2. The lowest threshold that we have observed for these GaInAs/InP devices is 2.8 kA/cm^2, which is about 5 times higher than the value obtained at 80 K for GaInAsP/InP DH diode lasers (with the same active layer thickness) emitting at 1.1 to 1.3 μm. The difference may be due to the exposure of the wafer to air after the growth of the active layer, a step that we have found to increase the threshold of GaInAsP/InP lasers by at least a factor of 5.

Since the laser threshold of GaInAsP/InP diodes increases by about an order of magnitude when the temperature is raised from 80 to 300 K, we expected the GaInAs/InP diodes to have pulsed thresholds of 20 to 40 kA/cm^2 at room temperature. However, laser operation has not been achieved at room temperature, even though current densities much higher than the expected thresholds were applied in experiments where the current was increased until diode failure occurred.

J. J. Hsieh

D. SEEDED BRIDGMAN GROWTH OF $AgGaSe_2$ SINGLE CRYSTALS

The I-III-VI_2 compound $AgGaSe_2$ is potentially an effective nonlinear material for frequency-doubling and mixing in the infrared.[10] However, the yield of crack-free single crystals obtained by unseeded Bridgman growth is very low. We have previously shown[11] that the low yield results because the thermal expansion coefficient of $AgGaSe_2$ is negative for directions within about 25° of the crystallographic c-axis. As a crystal cools to room temperature following solidification, it expands in these directions. Unless the growth axis happens to lie within 25° of the c-axis, this expansion produces a force normal to the walls of the growth ampoule that is strong enough to break the ampoule and crack the crystal. A marked increase in the yield of crack-free crystals can therefore be achieved by finding experimental conditions which ensure that the growth axis is parallel, or nearly parallel, to the c-axis. We have found that this can be accomplished routinely by using properly oriented seeds.

Starting charges up to 250 g have been synthesized from 6-9's Ag, 7-9's Ga, and 5-9's Se in fused-silica ampoules. The ampoule is first etched with HF and then coated with a layer of pyrolytic graphite by cracking methane gas at 100 Torr and 1100°C. It is then loaded with the elements, evacuated to a pressure of 10^{-7} Torr, and sealed. A tubular horizontal rocking furnace is used to obtain good mixing during synthesis. Because Se is so volatile and its reaction with Ag and Ga is highly exothermic, the ampoule will explode if the reaction mixture is heated too rapidly. No explosions have occurred with the following heating schedule. The furnace temperature is raised to 650°C in about 4 hr, held overnight, then raised to about 1000°C and held for 24 hr, all with continuous rocking. An outer sealed silica ampoule is used to house the reaction ampoule, which nearly always breaks during cooling.

The ampoules used for seeded Bridgman growth consist of an upper cylindrical section 13 to 36 mm in diameter, and a lower square section 5 to 6 mm on a side and 25 to 35 mm long, joined by a central tapered section. A silica rod 5 to 6 mm in diameter and 5 cm long is fused to the bottom of the ampoule. The ampoule is then graphite-coated. A square seed 20 to 30 mm long, oriented with its length parallel to the c-axis, is placed in the lower section. Even shorter seeds could be used successfully, and a close fit between the seed and the ampoule is not necessary. (The initial seeds were cut from uncracked portions of boules grown without seeding.)

The pre-reacted $AgGaSe_2$ is crushed and sealed into the growth ampoule at a pressure of about 10^{-7} Torr. A Pt/Pt-Rh thermocouple junction is tied to the outside of the square section halfway up the seed, and the ampoule is placed in the lower part of a preheated two-zone growth furnace. The two heating elements are separated by an ~1-cm air space to produce a steep temperature gradient between the zones, as shown in Fig. III-11. The ampoule is manually raised into the upper hot zone, until the thermocouple reads 850°C, to partially melt the seed. It is then mechanically lowered through the furnace at a rate of about 1 cm/day. The temperature during growth is controlled to about ±1/4°C. After solidification is complete, the power to the furnace is turned off and the ingot is furnace-cooled to room temperature.

This technique has resulted in a high yield of crack-free single crystals. Eleven ingots have been grown to date. None of the growth ampoules broke during cooling, and, in fact, the ingots were quite loose in the ampoules. Laue x-ray patterns taken at different points along several ingots showed that each one was a single crystal with the same orientation as the seed. Two of the ingots were partially cracked, but even these had large crack-free regions. Figure III-12 is a photograph of a single crystal 26 mm in diameter.

G. W. Iseler

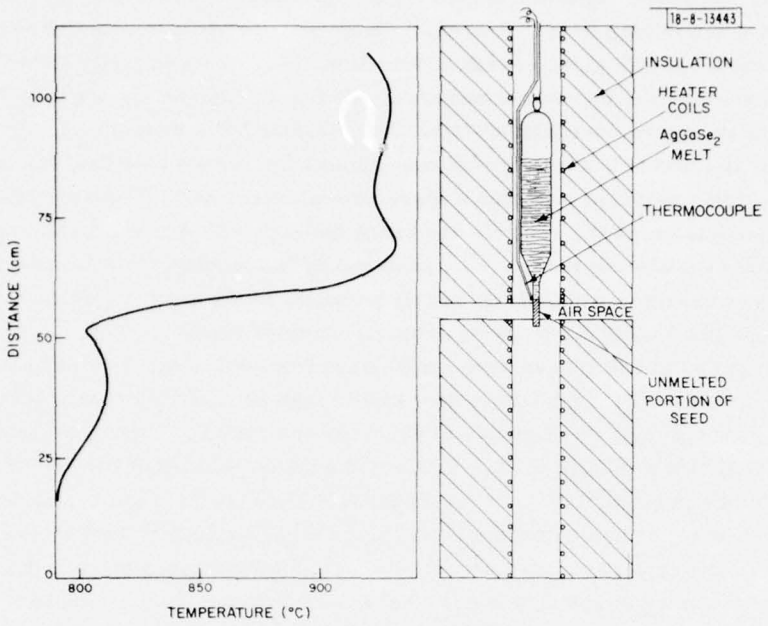

Fig. III-11. Schematic diagram of apparatus and temperature profile used for seeded Bridgman growth of $AgGaSe_2$ single crystals.

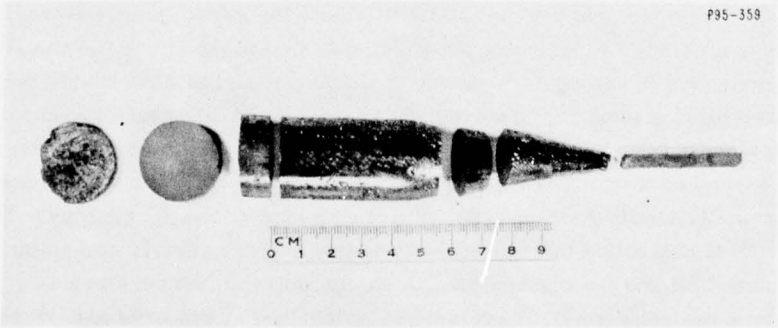

Fig. III-12. Single crystal of $AgGaSe_2$ grown by seeded Bridgman method.

E. SELECTIVE BLACK ABSORBERS USING RF-SPUTTERED Cr_2O_3/Cr CERMET FILMS

Selective black absorbers[12-14] with high solar absorption and low infrared emissivity can be used to increase the efficiency of flat-plate solar collectors. In principle, a single material could have this combination of properties. However, most of the selective black absorbers now available are prepared by coating a metal of high-infrared reflectivity (and therefore low-infrared emissivity) with a thin film that is transparent in the infrared but highly absorbing in the visible, where solar radiation is concentrated. The most popular of these coatings, known as chrome black or black chrome, is deposited on metal sheets by electroplating. The solar absorptivity obtained in this way is over 0.9; the infrared emissivity, which is determined by the infrared reflectivity of the metal, ranges from 0.04 for Cr-black on Cu (Ref. 14) to 0.12 for Cr-black on Ni (Ref. 13). For operation in air, the optical properties of Cr-black on Cu degrade at temperatures above 200°C, while Cr-black on Ni is stable up to 300°C.

Although electroplated Cr-black coatings have been in use for a number of years, their nature is not well understood and their properties are not very reproducible. They are so thin (less than 0.2 μm thick[15]) that quantitative chemical or structural analysis is difficult, and their optical properties cannot be measured directly, since they are prepared on opaque metal substrates. We made composition profile studies on Cr-black coatings by means of Auger spectroscopy, and also made x-ray diffraction studies on powders obtained by scraping coatings off their substrates. The results of these studies suggested that the coatings are cermet films composed of polycrystalline Cr_2O_3 and amorphous or extremely fine-grained Cr metal, in which the front surface is almost entirely Cr_2O_3, and the metal concentration increases toward the coating-substrate interface. A similar variation in the Cr/O ratio has been observed in earlier Auger studies, and evidence from x-ray photoemission for the presence of Cr_2O_3 has been reported.[15]

We recently prepared excellent selective black absorbers by using RF sputtering to deposit MgO/Au cermet films on metal substrates.[16] By analogy, this result supports the hypothesis that Cr-black coatings are Cr_2O_3/Cr cermets, and it led us to investigate the properties of Cr_2O_3/Cr cermet films deposited by RF sputtering. We found that deposition of these films on metal substrates also yields excellent selective black absorbers, with properties quite similar to those obtained with electroplated Cr-black coatings. This similarity is strong evidence that the electroplated coatings are actually Cr_2O_3/Cr cermets.

For convenient control of composition, the Cr_2O_3/Cr films were prepared by simultaneous RF sputtering of two hot-pressed targets, one of Cr_2O_3 and the other of Cr, each 12.7 cm in diameter. The deposition substrates were placed on a water-cooled platform that rotated at 10 rpm so that each substrate alternately intercepted the ions arriving from the two targets. Therefore, the film composition could be adjusted by changing the sputtering rates of the targets, which had been determined as a function of RF voltage in individual calibration experiments. In the present study, the deposition rate of Cr_2O_3 was kept constant at 14.5 Å/min., and the Cr deposition rate was changed to give films with Cr concentrations of 11, 21, 29, and 35 vol-percent. The substrate rotation rate and the deposition rates were such that the films consisted of an intimate mixture of Cr_2O_3 and Cr, rather than discrete layers of the two constituents. Transmission-electron microscope studies of specimens deposited on carbon substrates (carbon films 150 Å thick deposited on 200-mesh copper grid) showed that the films consist of individual Cr_2O_3 and Cr crystallites ranging in size up to about 150 Å.

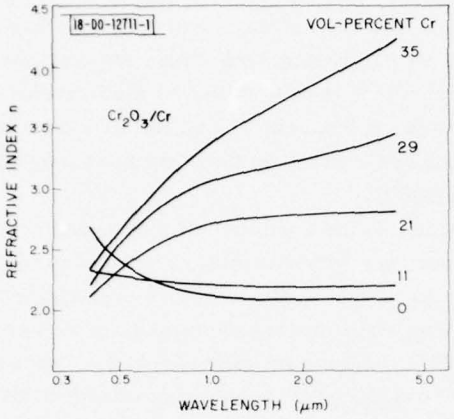

Fig. III-13. Refractive index as a function of wavelength for RF-sputtered Cr_2O_3/Cr cermet films.

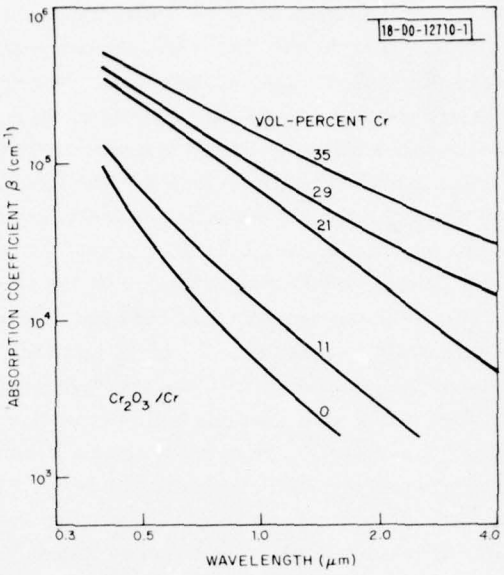

Fig. III-14. Absorption coefficient as a function of wavelength for RF-sputtered Cr_2O_3/Cr cermet films.

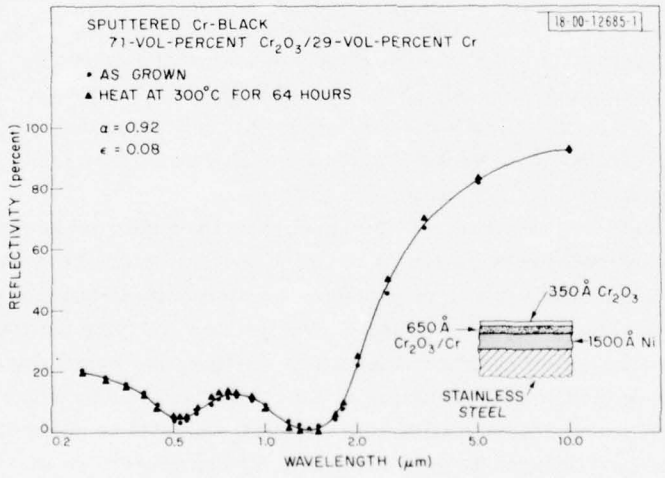

Fig. III-15. Reflectivity as a function of wavelength for composite prepared by successive deposition of Cr_2O_3/Cr and Cr_2O_3 films on Ni-coated stainless-steel substrate.

In order to determine the optical constants of the Cr_2O_3/Cr films, reflectivity and transmission measurements were made as a function of wavelength on specimens that had been deposited on single-crystal BaF_2 substrates. Values of the refractive index n and extinction coefficient k were obtained by fitting the data to expressions giving the reflectivity and transmission in terms of complex dielectric constants. The fitting procedure has been described in detail earlier.[16,17]

The wavelength dependence of n and the absorption coefficient β, which was calculated from k by using the expression $\beta = 4\pi k/\lambda$, is shown in Figs. III-13 and III-14, respectively. For wavelengths longer than about 1 μm, n increases monotonically with increasing Cr content, but at shorter wavelengths the variation is more complex. The value of β increases monotonically with Cr content over the whole wavelength range.

On the basis of the optical constants determined for the Cr_2O_3/Cr films, it appeared that good selective black properties could be obtained by deposition of such films on metal substrates. Approximate computer calculations indicated that the optimum film thickness would be less than 0.1 μm and that, of the various compositions investigated, 29-vol-percent Cr would be closest to the optimum. These calculations also showed that films with this composition would have a reflectivity of over 20 percent in the visible spectrum, causing a significant reduction in their solar absorptivity, unless they were antireflection-coated. Therefore, a number of composite specimens was prepared by successively depositing a cermet film of 29-vol-percent Cr and an antireflection coating of Cr_2O_3 on various metal substrates. The solar absorptivity α with respect to air mass a, and the infrared emissivity ϵ for an absorber temperature of 121°C were then determined by means of reflectivity measurements made with an integrating sphere. (The definitions of α and ϵ have been given previously.[12,14]) The reflectivity for one of these composites, consisting of a cermet film 650 Å thick and a Cr_2O_3 film 350 Å thick on a Ni-coated stainless-steel substrate, is plotted against wavelength in Fig. III-15. Note that the reflectivity is quite low in the visible spectrum, but beginning at about 2 μm it rises quite steeply to high values, as desired for low infrared emissivity. This composite has excellent selective black properties, with α of about 0.92 and ϵ of about 0.08 – values quite similar to those obtained by electroplating Cr-black coatings on metals. Comparable optical properties were also obtained for cermet films deposited on copper, aluminum, and uncoated stainless steel.

To investigate the stability of the composites, specimens were heated in air for several days at various temperatures and the reflectivity measurements were repeated. As shown in Fig. III-15, no significant change in the reflectivity of the specimen on Ni-coated stainless steel occurred on heating to 300°C for 64 hr. Heating to 400°C for 60 hr caused the film to crack, and in some areas to peel off the substrate, probably due to differences in thermal-expansion coefficients. As in the case of electroplated coatings, the composites involving the other metals were less stable, exhibiting significant degradation after heating to 300°C in air.

In view of the close similarity between the properties of the RF-sputtered films and the electroplated Cr-black coatings, we conclude that these coatings are Cr_2O_3/Cr cermets in which the high Cr_2O_3 concentration at the upper surface effectively reduces the solar reflectivity.

J. C. C. Fan
S. A. Spura

REFERENCES

1. J. J. Hsieh, J. A. Rossi, and J. P. Donnelly, Appl. Phys. Lett. 28, 709 (1976), DDC AD-A028550/2.
2. J. J. Hsieh, J. Crystal Growth 27, 49 (1974).
3. R. N. Hall, J. Electrochem. Soc. 110, 385 (1963).
4. J. P. McVittie, Technical Report No. 2-KSG-821, Stanford Electronics Laboratory, Stanford University (July 1972).
5. M. B. Panish and J. R. Arthur, J. Chem. Thermodynamics 2, 299 (1970).
6. N. Sol, J. P. Clariou, N. T. Linh, and M. Moulin, J. Cryst. Growth 27, 325 (1974).
7. J. J. Hsieh, J. Electrochem. Soc. 121, 99c (1974).
8. G. B. Stringfellow, J. Appl. Phys. 43, 3455 (1972).
9. H. Nagai and Y. Noguchi, Appl. Phys. Lett. 29, 740 (1976).
10. H. Kildal and J. C. Mikkelsen, Opt. Commun. 9, 315 (1973), DDC AD-777560/4.
11. Solid State Research Report, Lincoln Laboratory, M.I.T. (1975:1), p. 49, DDC AD-A009848/3.
12. G. E. McDonald, NASA TMX-3136, NASA Lewis Research Center (December 1974).
13. H. Y. B. Mar, J. H. Lin, P. B. Zimmer, R. E. Peterson, and J. S. Gross, "Optical Coatings for Flat Plate Solar Collectors," Contract No. NSF-C-957 (AER-74-09104), Final Report (September 1975).
14. J. C. C. Fan, Proceedings of Symposium on Optical, Electro-optical, Laser and Photographic Technology, Society of Photo-Optical Instrumentation Engineers, San Diego, August 1976 (to be published).
15. D. M. Mattox, J. Vac. Sci. Technol. 13, 127 (1976).
16. J. C. C. Fan and P. M. Zavracky, Appl. Phys. Lett. 29, 478 (1976).
17. J. C. C. Fan, Ph. D. Thesis, HR-28, Gordon McKay Laboratory, Harvard University, 1972 (unpublished); O. S. Heavens, Optical Properties of Thin Solid Films (Dover, New York, 1965), Chap. 4.

IV. MICROELECTRONICS

A. ION-IMPLANTED LO-HI-LO ANNULAR GaAs IMPATT DIODES

Large-area annular IMPATT diodes have been fabricated from GaAs having a lo-hi-lo impurity profile created by silicon ion implantation. Proton bombardment was used to define the annuli. Measurements of the thermal resistance of annular diodes and disk diodes of equivalent active area have indicated that the thermal resistance has been reduced by as much as 30 percent by virtue of the annular geometry. An efficiency of 35 percent with an output power of 7.4 W has been achieved at 3.0 GHz, and another device has generated an output power of 12.1 W with an efficiency of 21.6 percent at 3.15 GHz.

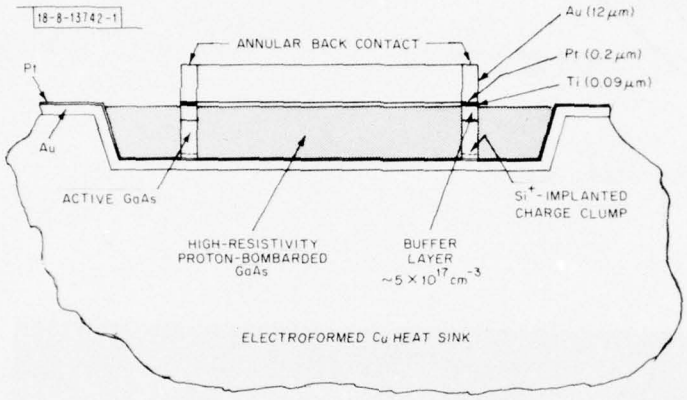

Fig. IV-1. Cross-section sketch of ion-implanted lo-hi-lo annular GaAs IMPATT diode. Active junction is Pt-GaAs Schottky barrier, and Si^+ implantation has been used to create high-efficiency profile. Device area is defined by proton bombardment.

The details of device construction are illustrated in Fig. IV-1. The procedures used to create the comparatively thin pockets of GaAs imbedded in a metallic heat sink are identical to those used in the fabrication of previously reported K_a-band, proton-guarded, GaAs IMPATT diodes.[1] Although a p-n junction has been shown to be better for high-temperature operation,[2] the active junction chosen for these devices was a Pt-GaAs Schottky barrier in order to simplify fabrication. The heat-sinking of the device is accomplished by a 10-mil-thick electroformed copper layer. The device is defined by proton-bombarding the wafer using the back contact as a shield against the proton flux. The bombardment schedule has been chosen to fully convert the entire, approximately 18-μm-thick, layer of unshielded GaAs to high-resistivity material. The resulting active device is the shielded GaAs lying beneath the back contact. The starting material, which is epitaxially grown in an H_2-$AsCl_3$-Ga vapor-phase system using sulfur as the dopant, consists of a 16-μm-thick, 2×10^{15}-cm^{-3} n-layer grown upon a 4-μm-thick buffer layer with a carrier concentration of approximately 5×10^{17} cm^{-3}. These layers are grown upon a heavily doped substrate which is normally completely removed during wafer processing.

The Si^+ implantation is the next step in wafer processing. The procedures connected with the implantation are, by far, the most critical aspect of the device's fabrication, and must be

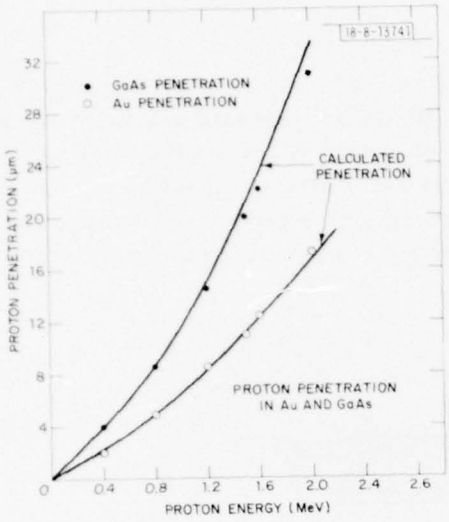

Fig. IV-2. Proton penetration in Au and GaAs. Data are obtained from capacitance measurements of bombarded samples, and are compared with calculation based on Bethe theory for proton-energy loss.

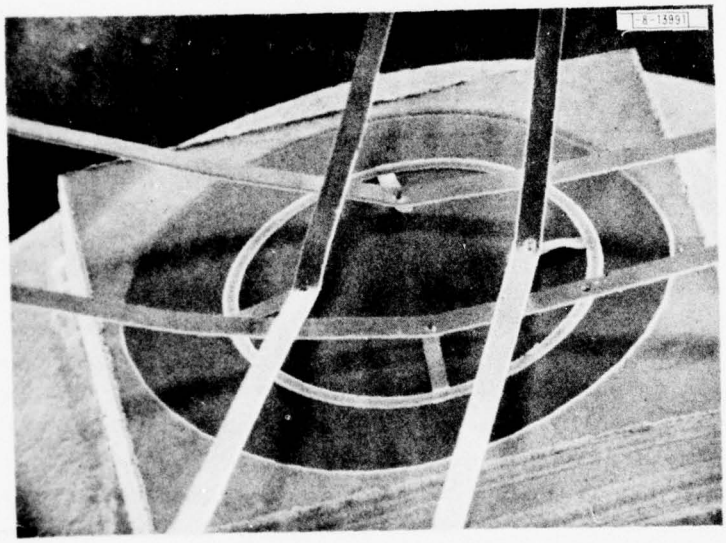

Fig. IV-3. Scanning electron micrograph of packaged device. Annulus shown has inner diameter of 39 mils and outer diameter of 42 mils. Four leads are fabricated onto annulus during wafer processing, and gold drop ribbon is TC-bonded to these leads in packaging.

done carefully in order to obtain the benefits of the ion-implantation technique. The starting epitaxial wafer is evaluated by using cleave and stain methods to determine the epitaxial-layer thickness, and by CV profiling to determine the n-layer carrier concentration. The wafer surface is also inspected under dark-field illumination for any irregularities, as our experience has been that pitted surfaces tend to produce leaky diodes.

The sample must be thoroughly cleaned. Our current procedure involves a solvent rinse, followed by a 5-min. hydrochloric acid soak to remove any native oxide. After a brief aqueous rinse, the wafer is vigorously sprayed with an aqueous detergent solution for 5 to 10 sec to remove particulates, and then rinsed in flowing distilled water for 3 min. Finally, the wafer is chemically etched in room temperature 5:1:1 H_2SO_4:H_2O_2:H_2O for 5 sec and again rinsed in flowing distilled water. Any form of metallic contamination must be scrupulously avoided in these steps.

The pyrolytic silicon nitride used as the encapsulant is deposited on the sample as quickly as possible after cleaning. The deposition system and the parameters used have been designed to avoid thermal damage to the GaAs surface during the deposition process.[3,4] The sample is resistively heated very rapidly, within 5 sec, to the deposition temperature of 690°C. The silane, ammonia, and nitrogen gas flows have been chosen to deposit the 500-Å silicon nitride layer in 10 additional seconds at this temperature. After deposition, the silicon nitride layer is densified by annealing in flowing nitrogen for 5 min. at 750°C.

The Si^+ is implanted through the 500-Å silicon nitride layer. The sample is then overcoated with 4000 Å of pyrolytic silicon dioxide on both sides to protect the sample from mechanical damage and annealed at 850°C for 15 min. in flowing nitrogen. After taking into account the ions lost in the nitride layer, the net donor activation is approximately 70 percent. The dose and energy of the Si^+ implant were determined empirically by measurements on test devices,[3,4] and are nominally 3×10^{12} cm^{-2} and 250 keV, respectively, for an n-layer concentration of 2×10^{15} cm^{-3}. We have, however, varied the dose of the implant slightly from epitaxial wafer to epitaxial wafer in order to maintain the drift region at the desired length.

The determination of the penetration of high-energy protons in GaAs and in the shielding material, gold, was necessary in order to fabricate these devices. GaAs samples with gold Schottky-barrier metallizations ranging in thickness from 0.1 to 30 μm were prepared and bombarded with protons of the energy of interest. The penetration of both Au and GaAs by the protons was inferred from capacitance measurements, and Fig. IV-2 shows the results. In addition to the measured data, the calculated penetration based on the Bethe theory for proton-energy loss is shown.[5] The data indicate that the penetration-energy relationship becomes significantly nonlinear at energies greater than 0.8 MeV.

Figure IV-3 is a scanning electron micrograph of a packaged annular device. Annuli of three different mean diameters have been fabricated, in addition to a disk device. All four of the device types have approximately the same area, equal to that of a disk having a diameter of 16.5 mils. The device shown in Fig. IV-3 is the largest annulus, having an inner diameter of 39 mils and an outer diameter of 42 mils. Leads are attached to the annulus in the wafer fabrication process, and a gold drop ribbon is TC-bonded to each of these leads in packaging, as shown. The four leads promote uniform current distribution and raise the self-resonant frequency of the packaged device to 12 GHz. The total spread of the breakdown voltage of these large-area diodes at 1 mA has typically been ±10 percent across a 1.3- by 1.3-cm wafer, very similar to that of the smaller devices reported earlier.[3,4] However, there has been a lower

percentage of acceptable large devices because of the higher incidence of diodes with leaky or soft current-voltage characteristics. This appears to be related to the greater probability of a larger-area device encompassing a defect in the gallium arsenide. The yield of devices with acceptably low leakage current prior to breakdown has been approximately 50 percent.

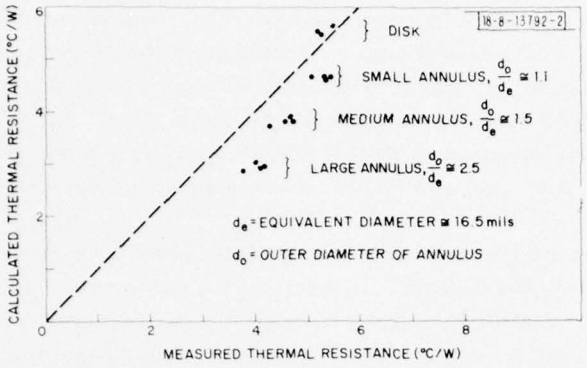

Fig. IV-4. Comparison of measured and calculated thermal resistances. Calculated thermal resistance is plotted vs measured resistances. A 45° line passing through origin is also shown for reference. Areas of each of devices measured are approximately equal to that of 16.5-mil disk.

Figure IV-4 compares calculated and measured thermal resistances. The calculation assumes circular symmetry and takes into account the chip edge, the spreading of heat through the gold, copper, and solder interface layers,[6] and the spreading into a semi-infinite heat sink on which the chip is assumed to be mounted. The assumed thermal boundary condition is a uniform thermal flux in the active device area. The measured data indicate an improvement in thermal resistance arising from the annular shape. However, the improvement is not as great as that predicted by the calculation. For example, the difference in thermal resistance between the largest annulus and the disk is measured to be about 1.5°C/W, compared with a predicted difference of 2.5°C/W. The measured improvement is nevertheless significant, amounting to a 30-percent reduction in thermal resistance. We feel that the difference between the measured and calculated thermal resistances arises from a thermal resistance in the diode mount of about 1°C/W (a reasonable estimate for our mount), and the fact that the uniform thermal flux boundary condition assumed in the calculation becomes less realistic for thicker annuli. Because of the dependence of breakdown voltage upon temperature, the nonuniform temperature distribution associated with the uniform thermal flux condition causes the device current to crowd toward the periphery of the active area. This tends to establish a more isothermal boundary condition at the device and would reduce the thermal resistance of thicker annuli more, producing the trend necessary for agreement with our data.

Devices were tested in a 14-mm coaxial cavity tuned by a pair of low-impedance noncontacting quarter-wavelength transformers. The axial position of the transformers, or slugs, could be adjusted through a slot in the coaxial outer conductor. Bias was supplied from a constant-current regulator through an inductively loaded line. This bias arrangement, although somewhat lossy, has suppressed bias circuit oscillations and has eliminated the tuning-induced failures[7] which had been a persistent problem with other arrangements.

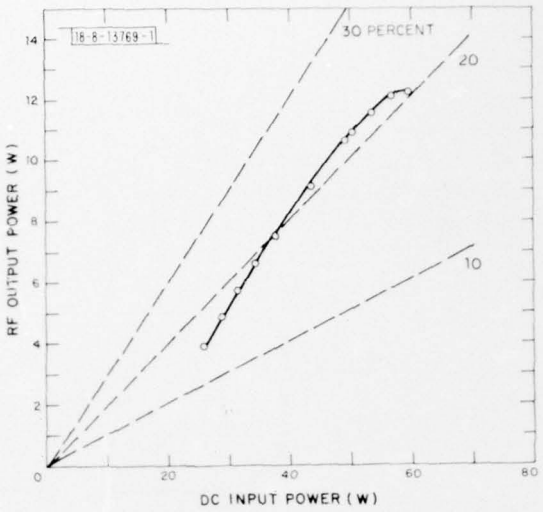

Fig. IV-5. Oscillator performance of lo-hi-lo device. RF output power at 3.15 GHz is plotted vs DC input power. Lines of constant efficiency are shown. Device generated 12.1 W with efficiency of 21.6 percent.

A plot of RF output power vs DC input power is shown in Fig. IV-5. This device generated 12.1 W of power at 3.15 GHz with an efficiency of 21.6 percent. A device tested with a different bias circuit had an efficiency of 35 percent with an output power of 7.4 W at 3.0 GHz, but this circuit caused many tuning-induced failures.

We feel that these studies have demonstrated that Si^+-ion implantation can be used to fabricate large-area lo-hi-lo IMPATT diodes, and that deep proton bombardment can be used to define the small geometries of the annuli we have fabricated. The RF performance obtained is consistent with our earlier measurements on smaller devices, and the thermal impedance of these devices has also been significantly reduced by virtue of the annular geometry.

R. A. Murphy
C. O. Bozler
J. P. Donnelly
R. W. Laton (Group 33)
G. A. Lincoln
R. W. Sudbury (Group 33)
W. T. Lindley

B. CHARGE-COUPLED DEVICES (CCDs): IMAGING SENSOR

Fabrication of a 100- × 400-cell CCD imaging sensor for the GEODSS (Ground Electro-Optical Deep Space Surveillance) Program has begun. Processing of the first set of silicon wafers has been completed, and approximately 13 percent were free of gate-gate and gate-substrate shorts and were thus suitable for dynamic testing. Successful operation of one of these devices with electrical input signals has been achieved at the design goal data rate of 400 kHz.

A schematic of the device is shown in Fig. IV-6, and is similar in structure to a 30- × 30-element prototype device described previously.[8] An input register at the top and a separate electrical input to the output register facilitate electrical characterization of the device. Figures IV-7(a) and (b) are photographs of the device: (a) shows the full chip, whose size is 13.3 × 3.6 mm, of which the imaging cells occupy an area 12.2 × 3.1 mm; (b) shows expanded views of the two ends of the device which contain all the bonding pads, input and output circuitry, and test structures. The need to restrict the bonding pads to the ends of the chip arises from the manner in which several of these chips will be assembled in a hybrid sensor array.[9] The test structures include gate-controlled diodes for monitoring dark-current and implantation

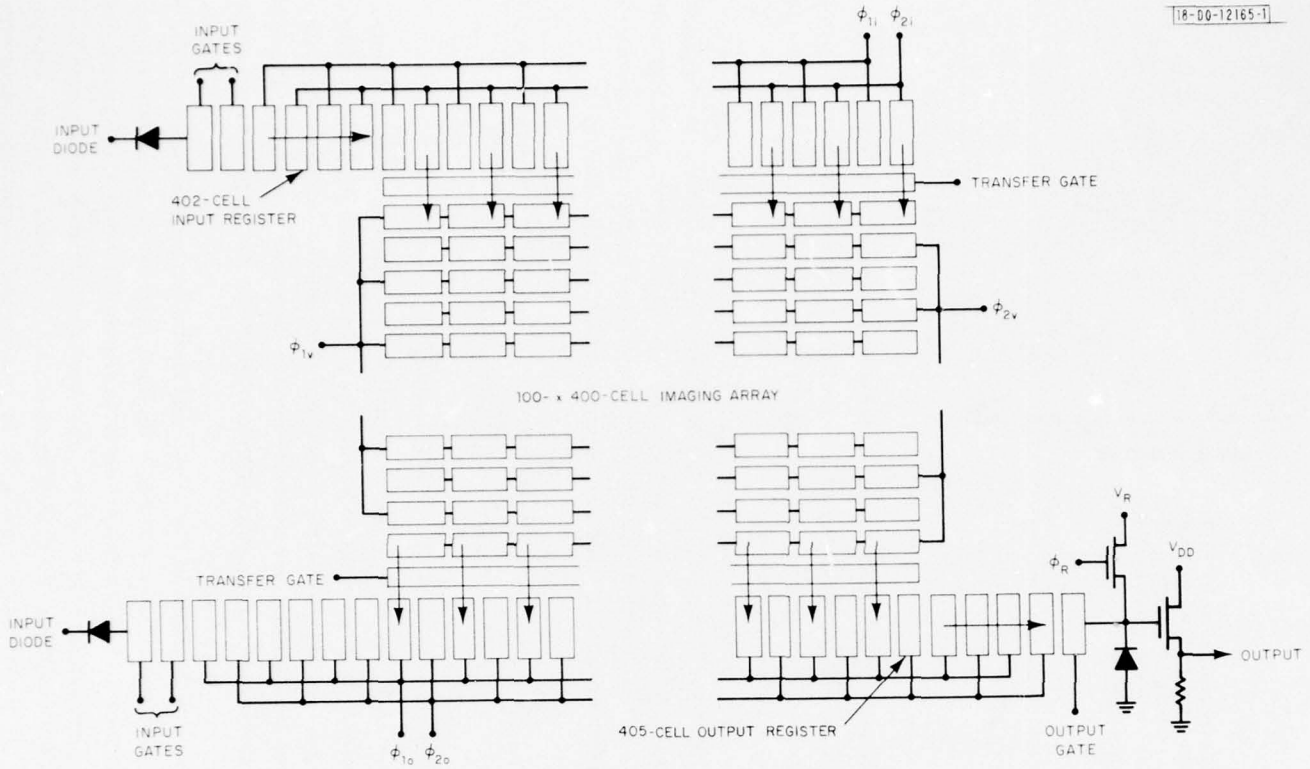

Fig. IV-6. Schematic of 100- × 400-element CCD imaging sensor. Device structure includes 40,000 imaging cells, input and output registers with electrical inputs to each, and output detection circuitry.

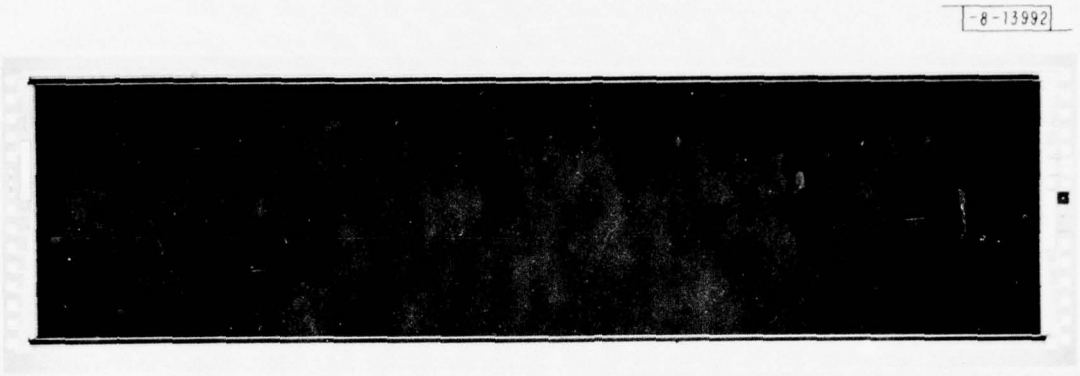

(a)

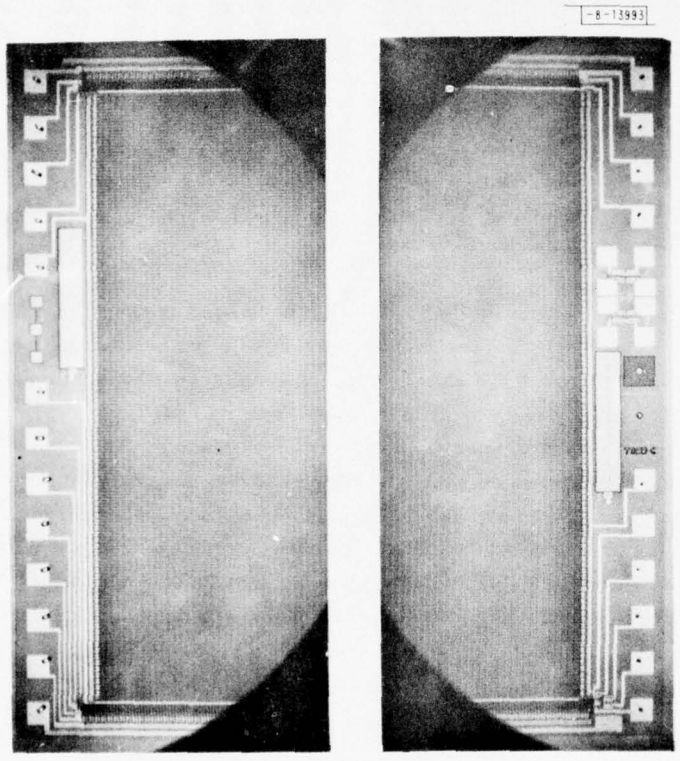

(b)

Fig. IV-7. Photograph of (a) 100- × 400-element CCD chip measuring 13.3 × 3.6 mm, and (b) magnified view of ends of chip.

profiles, MOSFETs for measuring the threshold voltages resulting from the different ion implantations used in the process, and polysilicon resistors for sheet-resistance measurements.

The devices were fabricated on 2-in. silicon wafers, with each wafer having 28 devices. Three such wafers have been completed and have been tested for shorts on an automatic wafer prober. The major yield loss has been shorts between the φ_1 and φ_2 sets of gates. This indicates failure of the thermal oxide grown on the first polysilicon layer to provide insulation between the two levels of polysilicon. However, in spite of the very large chip area, the initial run resulted in about 13 percent of the chips having no DC shorts.

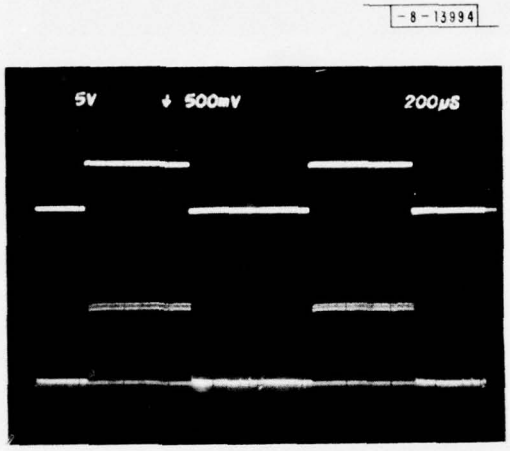

Fig. IV-8. Example of operation of device shown in Fig. IV-7(a) as an SPS analog delay line. Upper trace is signal applied to input register, while lower trace is resulting output signal 100 msec later. Data rate in this case is 400 kHz, and each output pulse consists of about 200 time-samples of input.

Devices which have passed to the DC probe test have been packaged and are now undergoing further evaluation. One of the devices has been successfully operated with an electrical input signal which was clocked through the entire device. This mode of operation is termed serial-parallel-serial (SPS) to denote the serial loading of signals to the input register, parallel transfer down the columns of the imaging array, and serial transfer in the output register to the output circuitry. Figure IV-8 shows an example of operation at a data rate of 400 kHz, which is the frequency at which the device is intended to operate. The input signal consists of rectangular pulses shown in the upper trace, while the lower trace is the output signal delayed by 100 msec. Measurements on the output register indicate transfer inefficiencies of about 3×10^{-4} per transfer at 400 kHz. Further electrical and optical evaluations of these devices are under way.

B. E. Burke R. W. Mountain
R. A. Cohen W. H. McGonagle

C. CHARGE-COUPLED DEVICES: PROGRAMMABLE TRANSVERSAL FILTER

A new transversal-filter structure is described which uses CCD technology and is capable of handling signals at data rates much higher than existing CCD implementations. This structure allows the tap weights to be programmed as digital words which can be stored on the device in static shift registers. A 32-stage prototype device has been designed and tested at clock rates up to 20 MHz, which is the limit of our present circuitry. Operation at even higher data rates appears feasible.

CCD transversal filters have received much attention recently as potential replacements for digital-signal processing systems in radar and spread-spectrum communications. A number of CCD[10-14] and bucket-brigade device[15] approaches have been demonstrated, but generally they are limited to sampling rates of less than 5 MHz. Applications exist where processing of wider bandwidth signals is needed while retaining the advantages of CCDs over digital implementations (i.e., lower package count, lower power consumption, and the ability to operate directly on an analog signal).

The evolution of the new device structure is described in Figs. IV-9(a-c) and IV-10. Figure IV-9(a) is the usual representation of a transversal filter as a tapped delay line. The time-delayed samples $v_i(t-nT)$ are nondestructively sensed at each stage of delay, multiplied by the tap weights h_n, and simultaneously summed to form the output signal $v_o(t)$. CCD implementations of this device are faced with two problems when sampling rates are pushed above a few megahertz. In most devices reported to date the signals are obtained as currents, either directly from the tapping electrodes or from intermediate MOSFET buffers. These currents are then summed in an off-chip operational amplifier. The difficulty lies in obtaining the high-speed current summation in an operational amplifier. The second problem is that the analog multipliers thus far proposed use on-chip transistors which are limited to speeds of a few megahertz.

In Fig. IV-9(b) the tapped delay line has been replaced by N separate delay lines resulting in a structure which, by removing the necessity for nondestructive sensing, will permit the summation process to be performed on charge rather than currents. A solution to the high-speed analog multiplication problem is shown in Fig. IV-9(c), where the tap weights are used in a binary representation. This reduces the problem to multiplication by 0 or 1, which can be done straightforwardly in a CCD. In the form shown in Fig. IV-9(c), the input signal $v_i(t)$ is weighted before entering each section of the device. This is the most attractive format since the resulting output will consist of charge summation at a single node. In some cases, however, it may be necessary to perform the charge summation in one or more sections separately, followed by weighting and summation of the signals as voltages. Such a case would occur, for example, if the binary words were expressed in a two's-complement format.

A CCD implementation of a 1-bit section is illustrated in Fig. IV-10. The binary multiplication is performed by means of a gate at the input to each of N CCD delay lines. This multiplication could be performed at either end of each delay line, but in the device to be described it was more convenient to do so at the input. The bits $a_1 \ldots a_N$ are stored in an MOS static shift register. The signal is sensed at a common charge collection bus by an on-chip MOSFET. Since signal input and charge transfer through a buried channel CCD are processes capable of clock rates greater than 100 MHz, the speed limitation of this device is in the output-detection circuitry. In the device to be described, the output circuit performed satisfactorily at 20 MHz, and operation at higher data rates is expected.

A prototype device consisting of two sections of 32 delay lines each is shown in Fig. IV-11. The device is a two-phase, implanted-barrier structure employing polysilicon for the storage gates and aluminum for the barrier gates.[16] An n-type, ion-implanted buried channel is used to enable high-speed operation. To reduce the RC time constant associated with the polysilicon gates and input diodes, the 32 delay lines are segmented into groups of eight, and the high-speed clocking waveforms are carried to each group on low-resistance aluminum lines. The gates controlling the digital reference function are brought out to bonding pads for external control in this first version of the device which does not incorporate the MOS static shift register shown

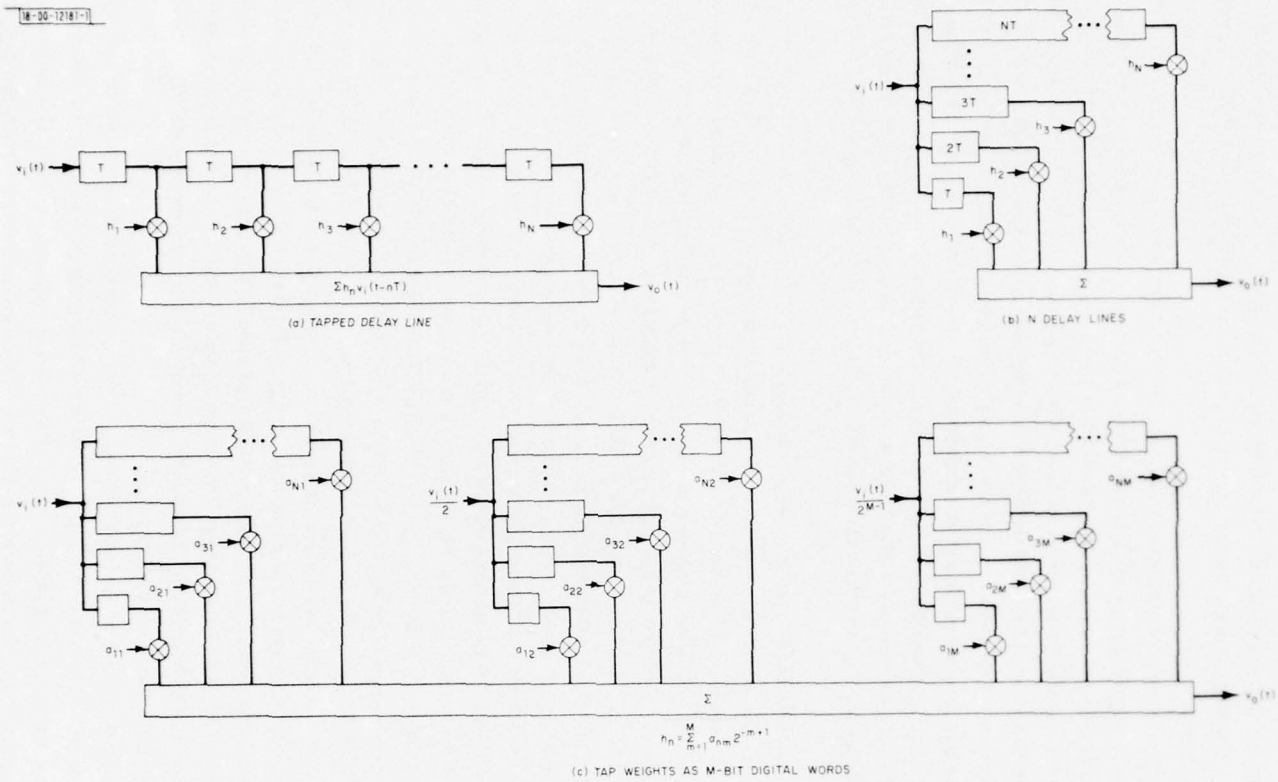

Fig. IV-9. *Evolution of transversal filter structure suitable for high-speed CCD implementation:* (a) conventional representation of transversal filter with an N stage tapped delay line and tap weight multipliers $h_1 \ldots h_N$; (b) single tapped delay line replaced with N separate delay lines; (c) tap weights are expressed in binary form, resulting in structure which does not require nondestructive tapping and replaces analog multipliers with multiplication by 0 or 1.

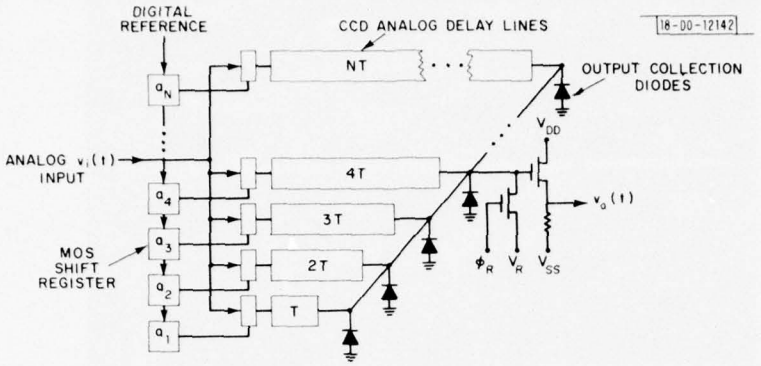

Fig. IV-10. Description of CCD implementation of 1-bit section of transversal filter shown in Fig. IV-9(c). Multiplication is accomplished on gates at input to each CCD delay line, and binary bits of reference words are stored in MOS shift register. Output signal is obtained by charge summation from all delay lines at single collection point.

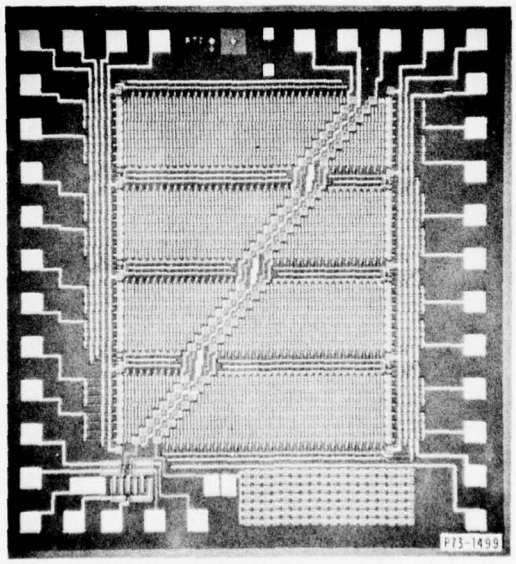

Fig. IV-11. Photograph of 32-stage prototype CCD programmable transversal filter consisting of two bit-weighted sections. Device is two-phase buried channel structure using polysilicon-aluminum overlapping gates. Chip size is 2.5 × 2.5 mm.

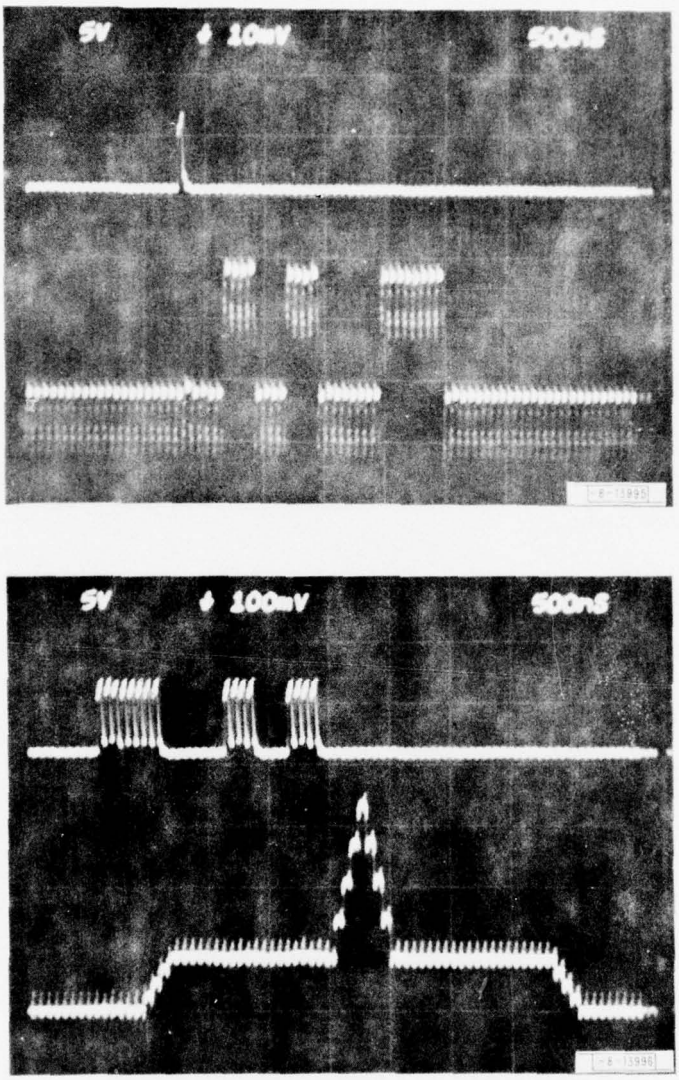

Fig. IV-12. Example of programmable matched filtering using one section of device in Fig. IV-11 at 15-MHz sampling rate. In (a), impulse response has been set for optimum stagger sequence 1010011 where each 1 or 0 of code corresponds to four "ones" or "zeros" of response. In (b), analog input to device corresponds to time-reversed impulse response, and resulting output gives autocorrelation function for this code.

in Fig. IV-10. Also, to reduce package IO pin count, the gates are tied together in groups of four on the chip. The outputs of each triangular section are sensed separately by two MOSFETs at the bottom left of the device. A series of diodes at the bottom of the chip simulates the capacitive loading on the output MOSFET circuitry of four additional sections. By means of a simple bonding operation, these diodes can be connected to the output of the section on the right, thus determining whether the reset transistor (the interdigitated structure at the bottom left) can reset a large output capacitance (approximately 10 pF) in a few nanoseconds. The device has been operated at data rates up to 20 MHz, even with this capacitive loading.

As an example of programmable matched filtering using one section, the reference gates were set so that the impulse response would represent the optimum stagger sequence 1010011 (Ref. 17). Because the reference gates are tied together in groups of four, each "zero" or "one" of the sequence is represented by four zeros or ones in the impulse response shown in Fig. IV-12(a); in Fig. IV-12(b) the same sequence but time-reversed is the input signal to the device, and the output has the expected shape and peak-sidelobe ratio for the autocorrelation function of this sequence. The data rate in this case was 15 MHz, which is the limiting speed of the word generator used for the input signal. A high-speed sample-and-hold circuit has been used to remove feedthrough of the clocking waveforms to the output circuitry.

Some nonuniformity in the impulse response can be seen in Fig. IV-12(a). This "fixed pattern noise" has been noted previously in CCD multiplexers,[18] and has been attributed to spatial fluctuations in substrate doping which, in turn, cause variations in the threshold voltages of the input signal gates. In our case, the dominant cause is a variation on the order of 5 percent in the capacitances of the 32 polysilicon input signal gates. It appears that this variation is a result of the polysilicon etching process that determines the gate widths. Alternative etching methods or a design change which replaces polysilicon with aluminum for this part of the device may alleviate this problem.

B. E. Burke
W. T. Lindley
R. A. Cohen
R. W. Mountain
W. H. McGonagle

D. EIGHT-BIT MULTIPLIER CIRCUIT USING MULTILAYER THIN-FILM HYBRID TECHNOLOGY

A two's-complement multiplier which can multiply two 8-bit signed numbers in less than 75 nsec has been fabricated in hybrid-integrated-circuit form using commercially available Schottky TTL dice. This project was undertaken in order to demonstrate the possible reduction in size of complex digital systems. The multiplier circuit was selected because we felt it would have greater applicability than a more specialized circuit. By putting 8 dice into one package, we have enabled a 6-to-1 reduction in system size over standard DIP packaging.

This particular multiplier consists of eight 4- by 2-bit multiplier chips connected in an array, and was designed for maximum speed and for ease of use in a 16- or 32-bit array for higher precision. It is a static device (no clocks required), and the 16-bit output is $Z = X Y + K$, where X, Y, and K are 8-bit two's-complement numbers. The constant (K) input is necessary in order to make possible the addition of the partial products when two or more multipliers are connected together in an array for precision greater than 8 bits.

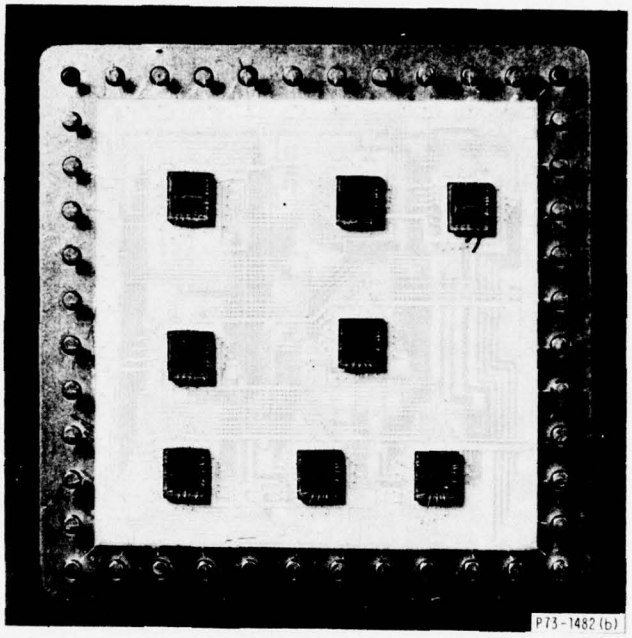

Fig. IV-13. A hybrid integrated circuit, 8- by 8-bit, two's-complement multiplier fabricated using a two-layer thin-film aluminum interconnect substrate and chip-and-wire assembly techniques.

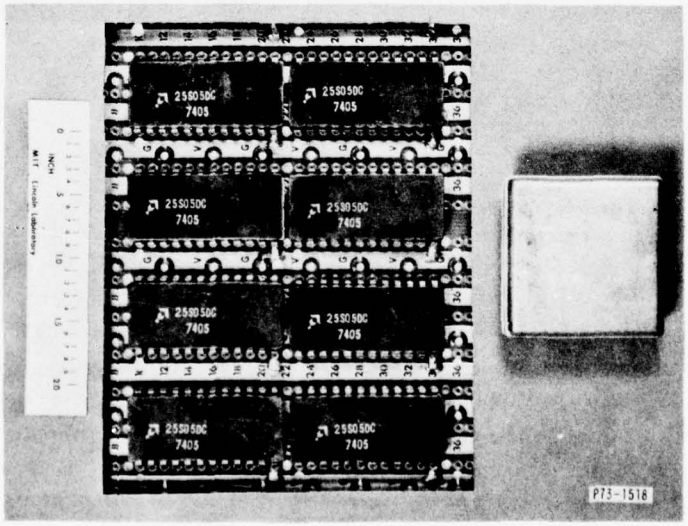

Fig. IV-14. Packaged hybrid multiplier microcircuit compared with wire-wrapped printed-circuit board realization of same function containing eight single-chip DIP packages.

The electrical parameters measured on the first prototype are:

Worst-case delay	72 nsec
Power dissipation	2.4 W at 5 V
Minimum power supply voltage	4.63 V

The high power-dissipation means that heat-sinking or forced-air cooling is required.

This device was fabricated using conventional chip and wire assembly techniques on a 1-in.^{2} substrate. Care was taken to insure that power supply and ground lines were arranged to minimize voltage drops, and were wide enough to prevent electromigration in the aluminum conductors. The mask layout was verified by drawing a schematic diagram from the layout and then building a working wire-wrap breadboard from this schematic. Such precautions greatly improve the chances of fabricating a working hybrid of this complexity. The completed circuit was electrically tested prior to capping in order to facilitate any repair which might be necessary, such as replacing open bond wires or defective die. Figure IV-13 is a photograph of the device. Figure IV-14 illustrates the 6-to-1 reduction in system volume that is achieved by eliminating the eight DIP packages, each containing a single die, and replacing these with a single 8-dice hybrid.

The conductors on the alumina substrate consist of two layers of 1-μm-thick sputtered aluminum separated by 1.5 μm of sputtered silicon dioxide. The conductors and vias were etched using conventional photolithographic techniques. We encountered no problems with shorts caused by pinholes in the oxide insulator, or with opens resulting from improperly etched vias.

D. L. Smythe
W. K. Hutchinson (Group 66)
J. Gorski-Popiel (Group 66)

E. INTEGRAL STRIPLINE FILTERS FOR SUBMILLIMETER-WAVE MIXER DIODES

The bias filter in a mixer diode circuit supplies DC bias to the mixer diode and provides the intermediate-frequency output, while presenting an almost perfect reflection at the signal and local-oscillator frequencies. At centimeter wavelengths, the bias filters are usually made by using quarter-wavelength low- and high-impedance coaxial-line sections to form a low-pass filter structure. However, at millimeter and submillimeter wavelengths the low-pass bias filters cannot be constructed in coaxial form since the coaxial line dimensions become too small to fabricate by conventional machining operations. Bias filters for submillimeter wave mixers have been provided by an integral stripline filter which is incorporated into the diode package. The characteristics of these filters at submillimeter wavelengths were inferred from measurements made on dimensionally scaled filter models in the frequency range from 1.0 to 9.0 GHz. This use of scaled models is essential in the evaluation of mixer components for potential operation in the submillimeter-wave region.

The integral filter concept is shown in Fig. IV-15. The whisker antenna contacting the Schottky-barrier diode is bonded to a pad at the end of the stripline filter. A 7-section filter with 20- and 100-ohm quarter-wavelength line sections was selected since this gave adequate filter characteristics and could be accommodated in the center of the 0.64-mm-diameter whisker stud used in the Lincoln Laboratory 38-GHz LES-8/9 mixer-diode package. The LES-8/9 mixer-diode packaging concepts and equipment were utilized as much as possible to provide

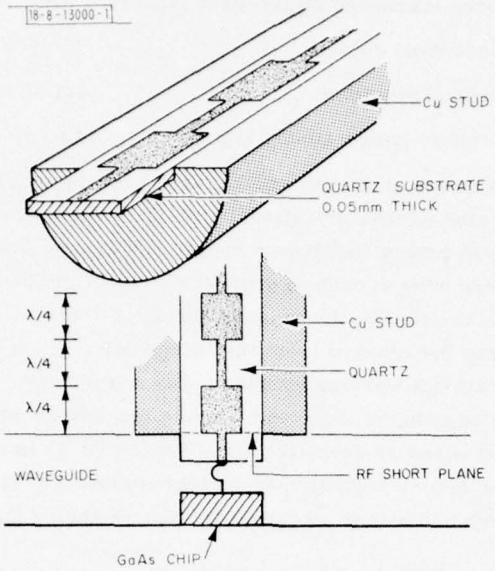

Fig. IV-15. Detailed view of stripline filter incorporated into diode stud and mounted in waveguide section. A channel is milled into one of the copper studs into which is inserted a substrate on which a photolithographically defined IF filter has been fabricated. In addition to creating an RF shorting plane at opening of waveguide, this configuration allows a good deal of design flexibility through variation of height of guide, thickness of GaAs chip, and length of antenna whisker.

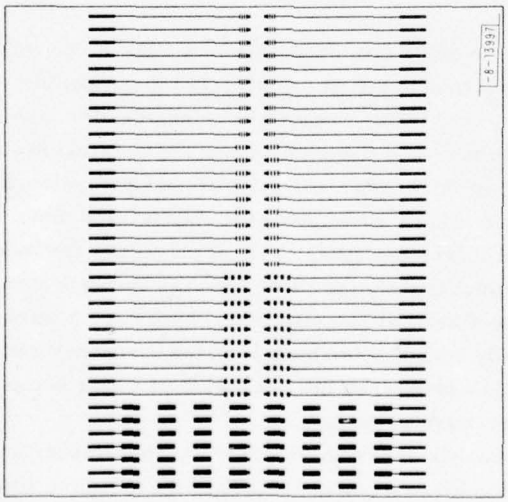

Fig. IV-16. Photolithographic masks for making filters at several frequencies. Group of largest patterns represents filters designed for RF of 55 GHz; progressively smaller patterns are filter masks for 300, 600, and 890 GHz.

for rapid development of the new submillimeter devices, and to maintain the ruggedness and reliability inherent in the LES-8/9 mixer-diode package.

The filters are fabricated on quartz substrates 19 mm square by 0.05 mm thick using conventional photolithographic techniques. The quartz substrates are solvent and detergent-cleaned, and are plasma-ashed to remove residual organics from the surfaces prior to the evaporation of 250 Å of chromium and 3 μm of gold onto both sides of the substrate. A mask having four groups of filter structures designed to operate at 55, 300, 600, and 890 GHz is shown in Fig. IV-16. After fabrication, the filters are separated by sawing the quartz into 0.36- by 6.1-mm strips. A shaped tungsten whisker is soldered to the bonding pad at the end of the filter section. The quartz strip is then soldered into a rectangular channel 0.38 mm wide by 0.08 mm deep which has been milled into one-half of a 0.64-mm-diameter copper stud (Fig. IV-17). A quartz cover section to form the other half of the stripline circuit environment is placed in the channel over the filter strip, and a copper cover stud is soldered in place to complete the integral-filter whisker-stud assembly. Etching the tungsten whisker to length and final whisker-shaping complete the whisker stud fabrication procedure. A completed submillimeter-wave diode with an integral-bias-filter and waveguide package is shown in Fig. IV-18.

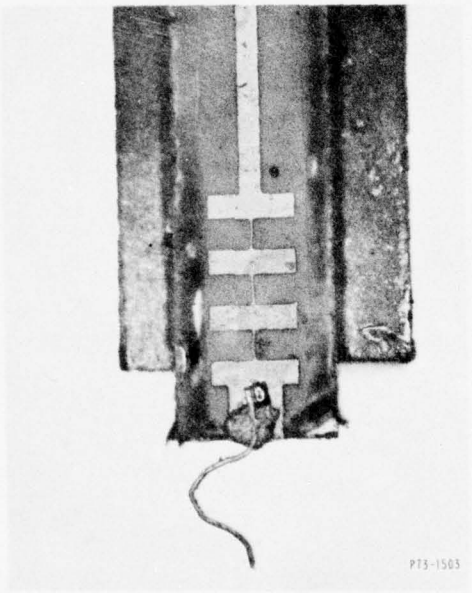

Fig. IV-17. Stripline filter in coaxial stud with attached antenna whisker. (Quartz cover and stud cover have been removed.) Separation between filter pads is $\lambda/4$ at operating wavelength. Channel width is about 0.4 mm.

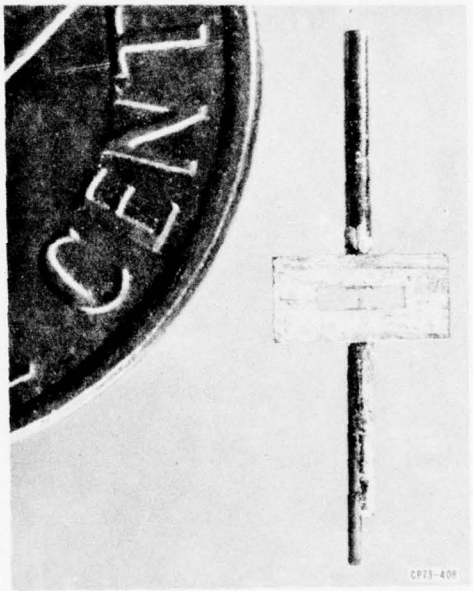

Fig. IV-18. Diode-waveguide mount with stripline filter inside bottom stud.

Calculations indicated that for 0.05-mm-thick quartz substrates the fringing fields associated with the step changes in stripline width would considerably modify the behavior of filters designed to operate above 600 GHz. Since measurements of filter characteristics at submillimeter wavelengths is extremely difficult, filter dimensions were scaled up by a factor of 100

so that measurements made on the scaled-filter models at frequencies in the range 1.0 to 9 GHz would correspond to measurements on the submillimeter filters in the range 100 to 900 GHz. The quartz substrate in the model filter became 38 mm wide by 5 mm thick, and a length of 152 mm was chosen as being adequate to accommodate the 7-section quarter-wavelength filters scaled to operate at 3.0, 6.0, and 8.9 GHz. In the model, the chrome-gold metallization was replaced by adhesive-backed copper foil which was readily cut to the scaled-filter dimensions using a sharp scalpel and rule under a low-power microscope. Time-domain reflectometry using a 35-psec risetime system provided a measurement of the stripline impedance levels, provided a measurement of the effective line lengths, and enabled the location and measurement of discontinuity reflections. The transmission and reflection characteristics of the scaled-model filters were measured on an automatic network analyzer over the frequency range 1 to 12 GHz. Measurements on the scaled-model filters indicated that the 300- and 600-GHz submillimeter filters should perform as designed, but that edge effects would limit the operation of the 890-GHz filter structure to a frequency only slightly greater than 600 GHz. The scaled models provided an easy way to measure and predict filter performance, and allowed easy adjustment and trimming of the filter characteristics. Modeling proved to be a powerful diagnostic tool, and essential to evaluate the potential performance of mixer components in the submillimeter-wave region.

B. J. Clifton

REFERENCES

1. R. A. Murphy, W. T. Lindley, D. F. Peterson, A. G. Foyt, C. M. Wolfe, C. E. Hurwitz, and J. P. *Donnelly, in* Gallium Arsenide and Related Compounds (The Institute of Physics, London, 1973), pp. 224-230, DDC AD-771891/9.
2. P. Staecker, W. T. Lindley, and R. A. Murphy, Proc. 12th Annual Reliability Physics Symposium, Las Vegas, 2-4 April 1974.
3. C. O. Bozler, J. P. Donnelly, R. A. Murphy, R. W. Laton, R. W. Sudbury, and W. T. Lindley, Appl. Phys. Lett. 29, 123 (1976), DDC AD-A030622.
4. Solid State Research Report, Lincoln Laboratory, M. I. T. (1976:1), p. 62, DDC AD-A027261/7.
5. J. F. Janni, "Calculations of Energy Loss, Range, Pathlength, Straggling, Multiple Scattering, and the Probability of Inelastic Nuclear Collisions for 0.1-TO 1000-MEV Protons," Air Force Weapons Laboratory Technical Report No. AFWL-TR-65-150 (September 1966).
6. P. Brook and J. G. Smith, Electron. Lett. 9, 253 (1973).
7. C. A. Brackett, Bell Syst. Tech. J. 52, 271 (1973).
8. Solid State Research Report, Lincoln Laboratory, M. I. T. (1976:3), pp. 43-45, DDC AD-A034647.
9. Ibid. (1975:4), pp. 46-48, DDC AD-A025489/6.
10. D. D. Buss, D. R. Collins, W. H. Bailey, and C. R. Reeves, IEEE J. Solid-State Circuits SC-8, 138 (1973).
11. D. R. Lampe, M. H. White, J. L. Fagan, and J. H. Mims, ISSCC Digest of Technical Papers, pp. 156-157 (1974).
12. J. J. Tiemann, R. B. Baertsch, and W. E. Engeler, ISSCC Digest of Technical Papers, pp. 154-155 (1974).
13. P. Bosshart, ISSCC Digest of Technical Papers, pp. 198-199 (1976).
14. D. J. MacLennan, J. Mavor, G. F. Vanstone, and D. J. Windle, Electron. Lett. 9, 610 (1973).
15. F. L. J. Sangster, Philips Tech. Rev. 31, 97 (1970).
16. D. M. Erb, W. Kotyczka, S. C. Su, C. Wang, and G. Clough, IEEE International Electron Devices Meeting, Session 2, Washington, D. C., 3-5 December 1973.
17. C. E. Cook and M. Bernfeld, Radar Signals: An Introduction to Theory and Application (Academic Press, New York, 1967), pp. 239-240.
18. S. P. Emmons, A. F. Tasch, Jr., and J. M. Caywood, IEEE International Electron Devices Meeting, Session 11, Washington, D. C., 9-11 December 1974.

V. SURFACE-WAVE TECHNOLOGY

A. SUPPRESSION OF BULK-SCATTERING LOSS IN SAW RESONATORS

A major goal in the development of surface-acoustic-wave (SAW) resonators has been to identify the loss mechanisms which occur in resonators and then to minimize these losses in order to obtain the maximum Q. With the push toward the fundamental limit on Q set by material propagation loss, small residual losses become important. One such loss degrades the efficiency of the grating reflector, and is due to scattering from the surface wave into bulk waves at the edge of the grating, as shown schematically in Fig. V-1. This surface-to-bulk mode conversion is confined to the immediate vicinity of the grating edge. The mode conversion results from abrupt discontinuities in the gratings. Such discontinuities occur at the boundary between the free surface and grating regions, or at the phase reversal between the two adjacent gratings in a SAW resonator.[1]

A technique has been demonstrated for suppressing the bulk-scattering loss which occurs in resonators whose reflective gratings consist of shallow grooves. The suppression itself is achieved by tapering the groove depth up to its final value over a relatively short distance (typically on the order of 20 to 30 grooves), as shown in Fig. V-2.

A schematic of the tapering process is shown in Fig. V-3. The grating reflectors are first defined in photoresist on the crystal surface, and the grooves are then etched by means of ion-beam bombardment through an aperture mask whose central obstacle is much wider than the gap between gratings. A taper in groove depth results from a slight divergence of approximately 12° (from normal) of the incident beam. With the parameters shown in Fig. V-3, the tapers obtained are basically linear and extend over roughly 25 grooves. The wide central obstacle results in an unetched (cavity) region of roughly 55 grooves between the two gratings (measured from the beginning of the tapers) in which coupling transducers may be placed.

The impact of such tapering on resonator Q was evaluated by measuring the Q of a number of different resonators, each consisting only of a pair of gratings without any transducers placed between the gratings. The Q was determined by measuring the transmission between a pair of transducers placed outside the gratings. Such measurements of Q do not include those additional loss processes which are known to occur when transducers are placed between the gratings.

Figure V-4 shows the Q of an empty $LiNbO_3$ resonator measured as a function of reflector groove depth. The lower data points for gratings of 200 and 300 grooves correspond to a regime in which the Q is limited by grating-reflection loss, and increasing groove depth leads to increasing reflectivity and hence Q. With the use of 600 grooves per reflector, however, a maximum Q of 33,000 is obtained, and increasing groove depth beyond 0.01 λ actually leads to decreasing Q. At this stage, bulk-scattering loss, and not reflection loss, becomes limiting. The use of deeper grooves only enhances the bulk scattering, and thus leads to lower Q.

Tapering the grooves from zero depth at the grating edge to a final depth of 0.012 λ over a distance of roughly 25 grooves yields Qs of 50,000 in air and 80,000 in vacuum at 170 MHz. These results, shown in Fig. V-4, are considerably improved over the corresponding untapered results, and clearly demonstrate the value of tapering. The remaining discrepancy between the measured and theoretical Qs is attributed to the nonoptimum nature of the tapers employed. It is important to note that a similar measurement of tapered-grating resonators on ST-quartz has yielded a Q of 61,000 in vacuum, which is essentially the material limit of the

PRECEDING PAGE BLANK-NOT FILMED

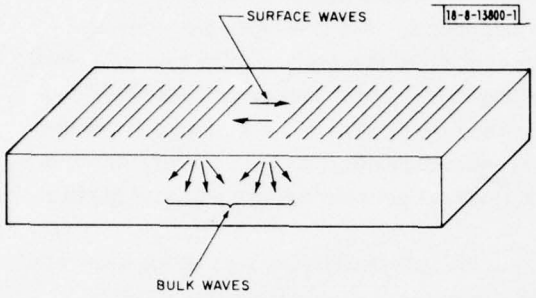

Fig. V-1. Surface-to-bulk mode conversion at grating edges.

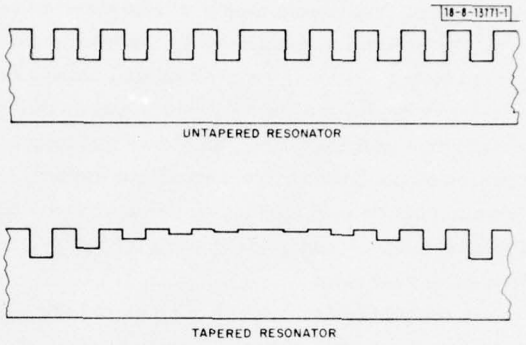

Fig. V-2. Depth tapering of grooved SAW resonator.

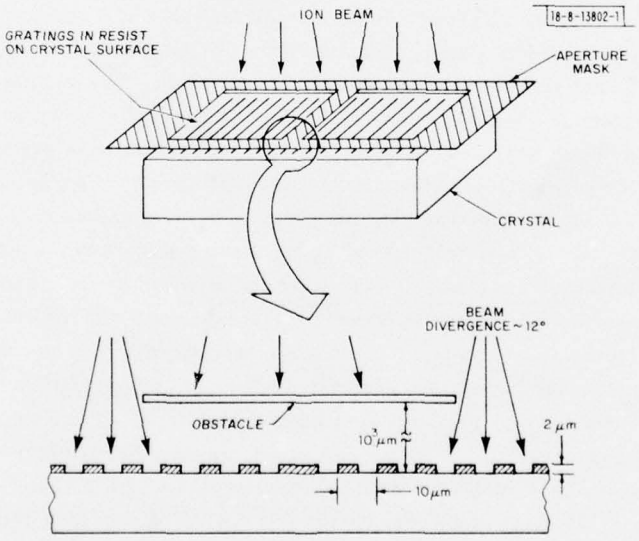

Fig. V-3. Schematic of depth tapering process.

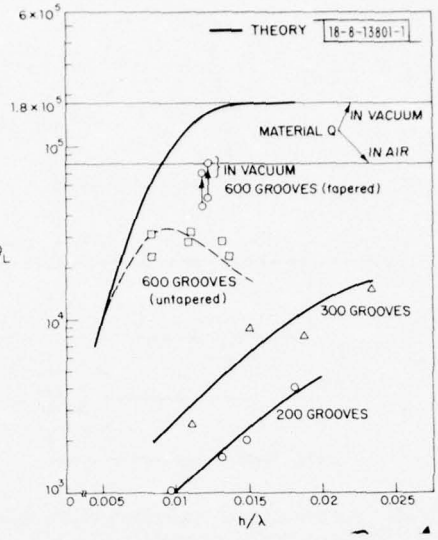

Fig. V-4. Comparison of measured and calculated Q values of empty $LiNbO_3$ resonators at 171 MHz.

substrate. This means that tapering the gratings has reduced bulk-wave scattering loss to a level which is small in comparison to the propagation loss at the resonant frequency. For resonators operating near or above 158 MHz, refinements of the taper profile to further reduce bulk scattering would be pointless.

R. C. M. Li
J. A. Alusow

B. VARIABLE-BANDWIDTH FILTER

Characteristic features of SAW reflective-array compressors (RACs) are a relatively flat response (typically ±0.5 dB) over a wide bandwidth, a very steep falloff at the band edges, and good out-of-band rejection (typically >70 dB). Given these features, it is possible to use RAC devices to make a variable-bandwidth filter which yields good shape factors over a wide and continuously variable range of bandwidths. The configuration of such a filter is shown in Fig. V-5. By varying the local-oscillator frequencies (derived from the VCOs) of the two pairs of mixers surrounding the two RAC devices, the overlap of the two passbands of the RACs effectively seen by the input signal can be varied as shown in the upper part of Fig. V-5. The overall filter characteristic from input to output is then the overlap of the two individual frequency responses of the RACs. In effect, one RAC cuts off the high-frequency end of the input spectrum, and the other RAC cuts off the low-frequency end. One VCO frequency is above the band of input frequencies and one is below this band, so that the linear dispersions of the two RAC devices cancel. The variable bandwidth filter has the property that it is nondispersive, but the delay through the filter is dependent on the bandwidth selected.

The feasibility of this type of variable bandpass filter has been demonstrated by connecting two existing RAC devices (described in Ref. 2) in a circuit such as in Fig. V-5. The RAC devices used had a bandwidth of 22 MHz centered at 95 MHz, and were flat to ±0.5 dB over the passband. At the band edges, the response fell from −3 to −70 dB in less than 0.8 MHz. By varying the two VCO frequencies in the two halves of the circuit in Fig. V-5, the 3-dB bandwidth can be varied continuously from 0.8 to 22 MHz. The response of the filter was measured for a sequence of bandwidths and is shown in Fig. V-6(a-c). Except for the very-narrow-bandwidth case, the

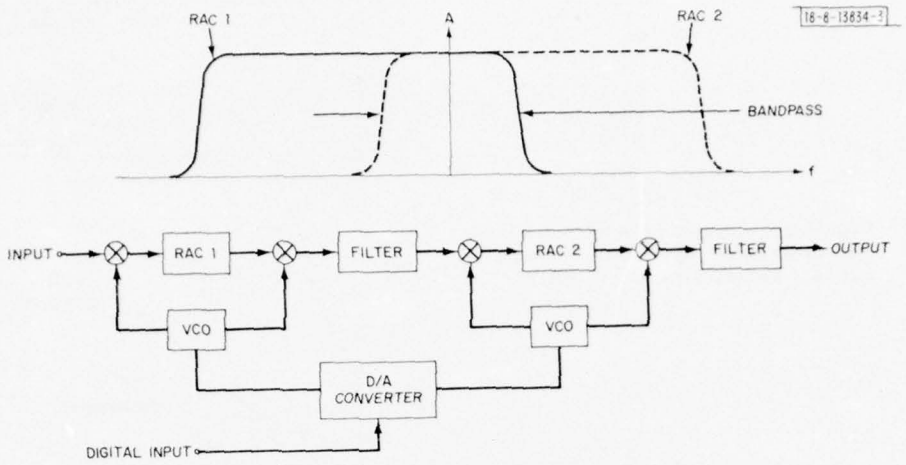

Fig. V-5. Schematic of operation of variable-bandwidth filter. By varying frequencies of two voltage-controlled oscillators (VCOs), the two RAC responses can, in effect, be offset with respect to input signal as shown at top. This produces a variable bandpass filter. VCOs can, in turn, be controlled by digital inputs.

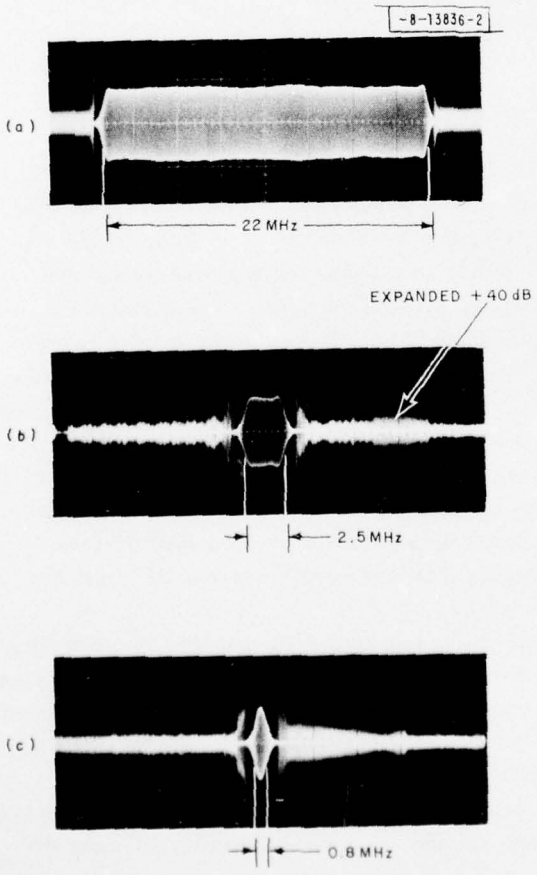

Fig. V-6. Response of variable-bandpass filter displayed as amplitude vs frequency. Horizontal scale is 3 MHz/division with center of each plate corresponding to an input frequency of 400 MHz. Outside of passband, vertical scale is expanded 100 times in amplitude (40 dB). Two local-oscillator frequencies (put out by two VCOs) are: (a) 305 and 495 MHz, (b) 295.3 and 504.7 MHz, and (c) 294.5 and 505.5 MHz.

out-of-band signal is seen to be at least 50 dB suppressed. Other measurements have shown that most of this out-of-band signal is, in fact, due to noise, which can be reduced by the proper choice of amplifier bandwidths.

A variable-bandwidth filter with 100-MHz bandwidth similar to the one described above is now being designed.

J. Melngailis
R. C. Williamson

C. ACOUSTOELECTRIC MEMORY CORRELATOR

Significant advances have been made in acoustoelectric-memory-correlator technology. We report these technological improvements and describe the accompanying benefits to the RF correlation performance. The feasibility of programmable matched filtering with an acoustoelectric-memory-correlator device was successfully demonstrated by Ingebrigtsen et al.[3] The device was a gap-coupled structure consisting of a matrix of free-standing Schottky-barrier diodes on a silicon strip in close proximity (~300-nm gap) to the surface of an $LiNbO_3$ SAW delay line.

The operation of a memory correlator involves first the storage of a reference signal, and subsequently the cross correlation of other signals with the stored reference. The phase and amplitude of a reference surface wave launched into the delay line of a memory correlator are recorded as a spatially varying charge pattern on the diode matrix by applying a forward-bias voltage pulse across the composite Si-$LiNbO_3$ structure for a fraction of an RF cycle. Upon removal of the impulse, the charge induced on the diodes serves to self-reverse-bias the diodes, and the reference signal is retained as a spatially varying depth modulation of the depletion layer behind the diodes. The maximum storage time is determined by the diode leakage current. During this storage time, a second signal may be launched into the delay line, wherein the piezoelectric fields of the second signal will interact with the spatially varying stored charge pattern of the reference signal. The resulting acoustoelectric voltage induced across the memory-correlator structure is the correlation between the second signal and the reference wave. The device then functions as a programmable matched filter, with the response determined by the stored reference wave.

Fabrication details and experimental results for the initial memory correlator devices have been reported elsewhere.[3-5] In addition to demonstrating feasibility of the concepts, these early results served to focus attention on several critical design areas for the memory correlator: mechanical assembly, diode array, and erase mechanism. Several improvements have now been made in these areas. We describe below the current device structure, and report substantial improvements in memory-correlation performance.

1. Mechanical Assembly

The correlator can operate well only if the correct acoustoelectric coupling is achieved across the air gap. For typical device parameters, this requires a mechanical assembly which achieves and maintains a 300-nm spacing, with ±10-nm uniformity between Si and $LiNbO_3$ surfaces over a 3.5- × 0.1-cm interaction region. An improved packaging technique which yields reproducibly uniform and stable gaps for acoustoelectric devices has been developed. A partially assembled device is shown in Fig. V-7. As in previous gap-coupled devices, the desired air gap is maintained by a pseudorandom array of microscopic spacer posts which are fabricated as an integral part of the $LiNbO_3$ surface.[6]

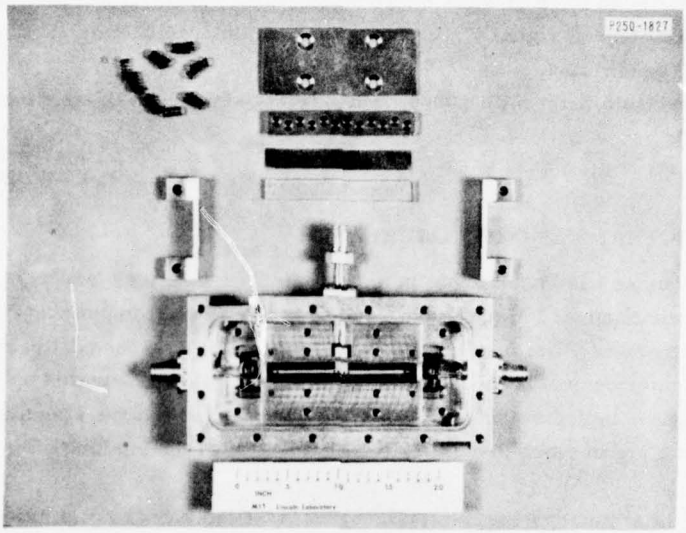

Fig. V-7. Partially assembled memory correlator. Visible within central cavity is low-inductance contact which has been fabricated on one surface of flexible Kapton sheet. Plated-through holes provide connection to silicon strip (not visible) which is indium-bonded to opposite Kapton surface. After alignment of silicon with acoustic beam path, strip is pressed against spacer posts on $LiNbO_3$ surface by means of an RTV gel, metal diaphragm, and springs which are placed above Kapton.

The major improvements over earlier configurations are: (a) the silicon is indium-bonded to a flexible Kapton sheet which incorporates a low-inductance output lead; (b) the uniform gap is maintained over a wide temperature range by a multi-component pressure assembly which acts on the back of the Si/Kapton element; and (c) direct EM feedthrough from input to output is suppressed by both metallic-film ground planes around the transducers and by metal septums which are placed between each transducer and the Si element. This packaging technique was first implemented for a convolver structure, and further details are contained in Ref. 7.

2. Diode Array

A high-quality diode matrix is the most critical feature of the memory correlator. Schottky barriers are the logical choice since, as majority-carrier devices, they offer high-frequency response and the possibility of storing wide-bandwidth signals. PtSi-to-n-type-Si barriers are appropriate because of the high (~0.85 eV) barrier height and potential for low-leakage currents.

Initial memory-correlator experiments utilized a diode matrix with 12.5-μm periodicity. Each diode consisted of a 5-μm-square PtSi region overlayed with an extended Cr/Au top contact 10-μm square.[4] The wide spacing of the diodes prevented adequate sampling (i.e., a minimum of 2.5 diodes per wavelength) of the SAW at frequencies above 100 MHz. Because efficient SAW transducers on $LiNbO_3$ are limited to approximately one-third relative bandwidth, a direct consequence of the wide diode spacing was to impose a 25-MHz-bandwidth constraint on these first memory correlators. An additional limitation, caused by nonuniformities in both air-gap and diode characteristics, was the restriction of waveform duration to $\lesssim 3$ μsec.

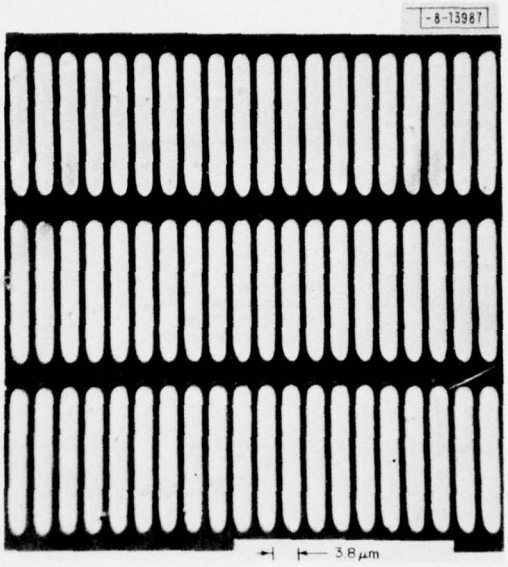

Fig. V-8. Photomicrograph of small segment of high-density PtSi Schottky-diode array. Slight granularity is due to small defects in electroplated gold-top contacts.

We have recently fabricated large, uniform, high-density diode arrays which allow correlation of waveforms of up to 10-μsec duration with a 70-msec storage time for the reference waveform. The 3.8-μm periodicity of the diodes in the direction of SAW propagation will permit adequate sampling of up to 350-MHz signals on the $LiNbO_3$ delay line. Figure V-8 is a photomicrograph of a small segment of such a high-density Schottky array. Each lozenge-shaped pattern is a PtSi diode topped with an electroplated Au contact. Fabrication of this new pattern is simplified by the use of plated contacts, hence the need for only a single photolithographic step which is used to define the matrix of windows in a 1000-Å-thick field of oxide prior to PtSi formation. This process was deemed essential because of difficulties experienced in reproducibly aligning successive patterns to within 1-μm tolerance over an entire 2-in.-diameter Si wafer with conventional techniques on commercially available equipment.

The procedure used to form the diodes precludes the fabrication of top contacts which extend beyond the PtSi periphery. Extended contacts would be beneficial in that they would act as guard rings and thereby reduce leakage currents by preventing intensification of reverse-bias electric fields at each diode perimeter. Despite the disadvantage of diodes lacking extended contacts, significant advances in Schottky-diode processing have been made which yield diodes with storage times well in excess of 10 msec, the minimum design goal, even for the 3.8-μm-period plated array.

The present diode-array-fabrication procedure utilizes n-type, phosphorous-doped, ⟨100⟩-oriented Si of 20-Ω-cm resistivity. An initial 100-nm oxide is grown at 1100°C in dry O_2 with 3-percent HCl, and a 1000-nm chemically vapor-deposited (CVD) SiO_2 or 150-nm Si_3N_4/300-nm SiO_2 composite layer is deposited to mask the front surface from the subsequent diffusion. A heavy phosphorous predeposition and diffusion (each for 30 min. at 1100°C) create an ohmic back contact and serve to getter crystallographic defects. Next, the front CVD and thermal layers are stripped and a new 100-nm oxide is grown (3-percent HCl, 1100°C), followed by a 30-min. N_2 anneal in 3-percent HCl at 1100°C. The combination of phosphorous gettering and HCl oxidation serves to maintain long minority-carrier lifetime (≳75 μsec), a requirement for low-leakage currents.

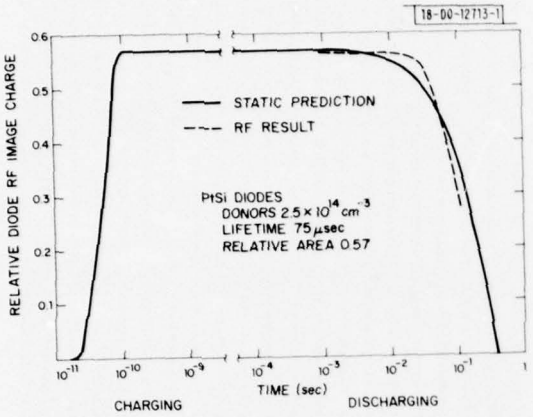

Fig. V-9. Charging and discharging characteristics of wideband diode array. Static prediction is calculation based upon DC I-V characteristics observed for large-area test diodes. An actual RF memory-correlator result for high-density array is also shown.

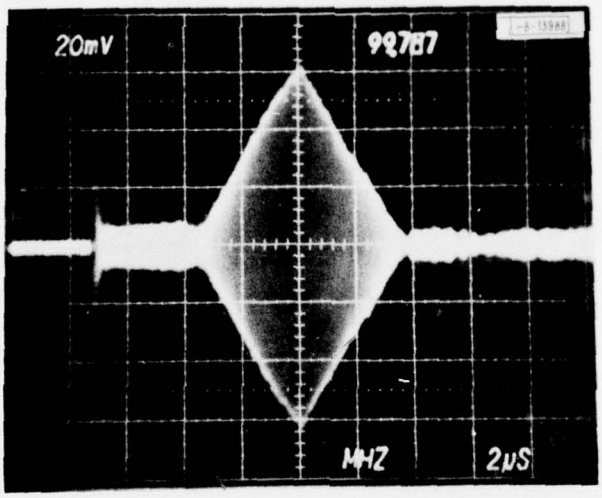

Fig. V-10. Correlation output obtained for two 100-MHz, 4-μsec bursts, with first waveform having been stored for 1 msec.

The lozenge-shaped pattern of holes is photolithographically produced and etched into the SiO_2. Then the front surface is RF sputter-etched to remove ~10 nm of SiO_2, and 60 nm of Pt is immediately sputtered onto the wafer. A 450°C sinter in pure H_2 for 10 min. completes the formation of a smooth, 120-nm-deep PtSi layer[8] in each window without creating SiO_2 that can interfere with the PtSi formation. A subsequent 600°C anneal in pure O_2 for 8 min. creates a thin layer of SiO_2 above the PtSi. This thin oxide prevents destruction of the PtSi when the unwanted Pt atop the 100-nm thermal SiO_2 is removed in modified aqua regia[9] ($4H_2O$:3HCl:1HNO_3 at 85°C). A subsequent pure H_2 anneal at 600°C for 15 min. reduces the density of surface states at the SiO_2-Si interface (~2×10^{10} $cm^{-2}eV^{-1}$ at midgap) and prevents excessive interface-leakage currents. The back-side oxide is removed and a 30-nm Cr/300-nm Au evaporated contact is applied.

After a dip etch in buffered HF, the front contacts are electroplated with fine-grained Au using a commercial solution at 50°C (Ref. 10). 1000 nm of In is then evaporated on the back, the 3.5-cm-long × 0.075-cm-wide correlator strips are saw cut from the wafer, and the damaged edges are chemically etched.

Large-area MOS dots and PtSi diodes were fabricated along with the correlator arrays in order to better characterize the device. Standard MOS tests indicate the high quality of the oxide which separates the diodes. Typical parameters are 0.3-V flatband shift, 75-μsec hole lifetime, and 2×10^{10} $cm^{-2}eV^{-1}$ surface states at midgap. Near-ideal diode behavior is also obtained.[11] The Schottky characteristic is well represented by

$$J = 21.3 \left(\exp\left|\frac{eV}{1.029\ kT} - 1\right|\right)\ nA/cm^2$$

for 2.5×10^{14} donors/cm^3 at 22°C. In addition to the ~20-nA/cm^2 leakage over the reverse-biased barrier, there is the expected leakage due to the thermal generation of electron-hole pairs within the depletion layer, which goes as en_iW/τ where n_i is the intrinsic carrier density, W is the depletion width, and τ is the effective lifetime. For 20-Ω-cm Si, this current is found to be double that of the Schottky component, a result which is consistent with the 75-μsec lifetime deduced from MOS tests. Thus, the total reverse leakage for a large-area diode was about 50 nA/cm^2 at −10 V.

These observed static I-V characteristics were used to predict the charging and discharging characteristics for a wideband array. As seen in Fig. V-9, the diodes should charge rapidly reaching in 100 psec a charge level determined by their filling factor within the array. In an actual device, the charging time is presently limited by external circuitry to ~1 nsec. Appreciable charge is expected to remain in the array for 100 msec. The actual RF response of a high-density array is seen to be in reasonable agreement with the static prediction. Differences in the discharging characteristics are attributed to the omission within the static model of two device features. The additional edge leakage to be expected within the high-density array was not estimated. However, the increased rate of charge loss is partially balanced by the second feature, an increased efficiency for the readout process as the depletion layer collapses.

3. RF Results

Initial RF characterization of the modified correlators showed substantial improvement in device performance. A typical correlation output is displayed in Fig. V-10. This triangular output represents the correlation between two 100-MHz, 4-μsec bursts, with the first waveform

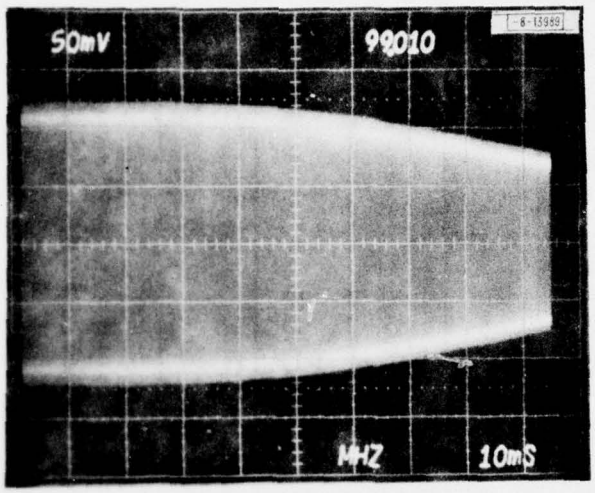

Fig. V-11. Storage capability of high-density array.

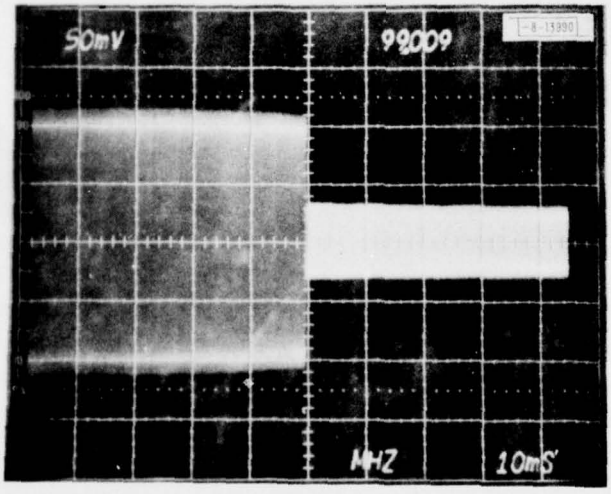

Fig. V-12. Storage followed by LED erasure.

having been stored for 1 msec. For convenience in the preliminary RF experiments, the high-density arrays were mounted with 100-MHz delay lines, hence the bandwidth is transducer-limited to 25 MHz. Also, for diagnostic purposes these devices were packaged in a manner which allowed convenient optical inspection of the air gap, but which obviated techniques for maximum suppression of spurious levels. Consequently, there is a relatively high level of direct EM feedthrough from the input which leads and overlaps with the desired output. In addition, spurious shear bulk waves introduce unwanted fine structure on the correlator output and yield signals which trail the desired response. Methods which are available for suppressing all these spurious signals will be implemented in future devices.

One of the major improvements in correlator performance results from the low-leakage currents achieved for the diodes. A display of the concomitant storage time is shown in Fig. V-11. A 100-MHz, 4-μsec burst was stored in the device at time zero, and subsequently a train of repeated identical bursts was entered and multiple correlations with the stored pattern were obtained. The envelope indicates the successive peaks of the correlation output. Note that the readout process is nondestructive. There is essentially no memory loss for the first 30 msec, and 3-dB storage loss does not occur for 70 msec. This represents an improvement in memory time of nearly two orders of magnitude over earlier devices.[6]

Because of signal-processing requirements, a need exists to rapidly clear the memory and have it recover quickly so that at any desired point in time, the signal-processing cycle could be initiated with a new reference waveform. A convenient mechanism exists for the erasure: photon-enhanced leakage current. As was described earlier, the predominant leakage current arises from the thermal generation of electron-hole pairs within the depletion layer, and this current can be enhanced in a controllable fashion by illuminating the Schottky array with green-light-emitting diodes (LEDs). Green light was selected to provide essentially complete absorption within the depletion layer so that all the holes generated are swept by the depletion field into the PtSi regions and rapidly discharge the array. A typical result is shown in Fig. V-12 where the normal storage of a reference waveform and subsequent multiple cross correlations were produced as in Fig. V-11 for the first 50 msec after entering the reference. Then a 160-μsec pulse of green light from five LEDs mounted under the delay line was used to completely discharge the array. The total time for the erase-and-recover process is 200 μsec, and is sufficiently short for most radar-signal-processing applications.

4. Recent Achievements Compared With Design Goals

The memory-correlator performance as it exists today is compared with the program design goals in Table V-1. Device characteristics have met most of the goals. A bandwidth of 100 MHz will be realized as soon as the existing 3.8-μm-period Schottky arrays are mounted against appropriate delay lines. Storage time is more than adequate, with 70 msec observed at a device temperature of 20°C. Of course, the leakage current is exponentially dependent on temperature, and a storage time for 3-dB memory loss of 25 msec is observed at 30°C. Therefore, the design goal of 10-msec minimum storage time is met at temperatures up to 40°C. This does not represent an application restriction since a compact thermoelectric unit can easily cool the correlator. Some improvement is still required in the interaction uniformity. The existing ±1-dB uniformity was limited not by the diodes but rather by particulate contamination of the air gap in these devices, and cleaner assembly techniques should provide improved

TABLE V-1
MEMORY CORRELATOR PERFORMANCE

	Achievement	Goal
Center Frequency (MHz)	100	300
Bandwidth (MHz)	25	>50
Waveform Duration (μsec)	10	>10
Storage Time (−3 dB) (msec)	70	>10
Maximum Temperature (T_S = 10 msec)	>40°C	>30°C
Dynamic Range (above kTB) (dB)	70	>60
Amplitude Uniformity (dB)	±1	±1/2
Spurious Level (dB)	−23	−35
At 1-dB Compression Point:		
P_{REF} (dBm)	18	–
P_{SIG} (dBm)	20	–
P_{OUT} (dBm)	−30	–

uniformity. Spurious levels are unacceptably high in the existing correlators, and for this reason the $LiNbO_3$ substrate geometry is undergoing extensive modifications. These modifications, as well as wideband correlator performance, will be reported at a later date.

R. W. Ralston
J. Cafarella
S. A. Reible
R. A. Cohen
R. W. Mountain

REFERENCES

1. H. A. Haus, "Bulk Scattering Loss of SAW Grating Cascades," to be published in IEEE Trans. Sonics and Ultrasonics.
2. V. S. Dolat and R. C. Williamson, "A Continuously Variable Delay-Line System," in 1976 Ultrasonics Symposium Proceedings (IEEE, New York, 1976), pp. 419-423.
3. K. A. Ingebrigtsen, R. A. Cohen, and R. W. Mountain, Appl. Phys. Lett. 26, 596 (1975), DDC AD-A016703/1.
4. Solid State Research Report, Lincoln Laboratory, M.I.T. (1975:1), p. 57, DDC AD-A009848/3.
5. K. A. Ingebrigtsen, Proc. IEEE 64, 764 (1976), DDC AD-A028456/2.
6. Solid State Research Report, Lincoln Laboratory, M.I.T. (1976:1), p. 69, DDC AD-A027261/7.
7. Ibid. (1976:3), p. 54, DDC AD-A034647.
8. D. Shinoda, Rev. Phys. Chem. Japan 42, 94 (1972); A. K. Sinha et al., J. Appl. Phys. 43, 3637 (1972).
9. M. J. Rand and J. F. Roberts, Appl. Phys. Lett. 24, 49 (1974).
10. "BDT 200," The Sel-Rex Co., 75 River Rd., Nutley, New Jersey 07110.
11. J. M. Andrews and M. P. Lepselter, Solid-State Electron. 13, 1011 (1969).

UNCLASSIFIED

SECURITY CLASSIFICATION OF THIS PAGE *(When Data Entered)*

REPORT DOCUMENTATION PAGE

READ INSTRUCTIONS BEFORE COMPLETING FORM

1. REPORT NUMBER: ESD-TR-76-327
2. GOVT ACCESSION NO.
3. RECIPIENT'S CATALOG NUMBER
4. TITLE *(and Subtitle)*: Solid State Research, 1976:4
5. TYPE OF REPORT & PERIOD COVERED: Quarterly Technical Summary rept. 1 August – 31 October 1976
6. PERFORMING ORG. REPORT NUMBER: 1976:4
7. AUTHOR(s): Alan L. McWhorter
8. CONTRACT OR GRANT NUMBER(s): F19628-76-C-0002
9. PERFORMING ORGANIZATION NAME AND ADDRESS: Lincoln Laboratory, M. I. T., P. O. Box 73, Lexington, MA 02173
10. PROGRAM ELEMENT, PROJECT, TASK AREA & WORK UNIT NUMBERS: Program Element No. 65705F, Project No. 649L
11. CONTROLLING OFFICE NAME AND ADDRESS: Air Force Systems Command, USAF, Andrews AFB, Washington, DC 20331
12. REPORT DATE: 15 November 1976
13. NUMBER OF PAGES: 98
14. MONITORING AGENCY NAME & ADDRESS *(if different from Controlling Office)*: Electronic Systems Division, Hanscom AFB, Bedford, MA 01731
15. SECURITY CLASS. *(of this report)*: Unclassified
15a. DECLASSIFICATION DOWNGRADING SCHEDULE

16. DISTRIBUTION STATEMENT *(of this Report)*

Approved for public release; distribution unlimited.

17. DISTRIBUTION STATEMENT *(of the abstract entered in Block 20, if different from Report)*

18. SUPPLEMENTARY NOTES

None

19. KEY WORDS *(Continue on reverse side if necessary and identify by block number)*

solid state devices
quantum electronics
materials research
microelectronics
surface-wave technology
photodiode devices
lasers
laser spectroscopy
imaging arrays
infrared imaging
surface-wave transducers

20. ABSTRACT *(Continue on reverse side if necessary and identify by block number)*

This report covers in detail the solid state research work of the Solid State Division at Lincoln Laboratory for the period 1 August through 31 October 1976. The topics covered are Solid State Device Research, Quantum Electronics, Materials Research, Microelectronics, and Surface-Wave Technology. Funding is primarily provided by the Air Force, with additional support provided by the Army (BMDATC), ARPA (MSO, IPTO), NSF, and ERDA.

DD FORM 1 JAN 73 1473 EDITION OF 1 NOV 65 IS OBSOLETE

UNCLASSIFIED

SECURITY CLASSIFICATION OF THIS PAGE *(When Data Entered)*

207650